R. & M. No. 3526

MINISTRY OF TECHNOLOGY

AERONAUTICAL RESEARCH COUNCIL
REPORTS AND MEMORANDA

An Experimental Investigation of the Compressible Turbulent Boundary Layer with Air Injection

By L. O. F. JEROMIN, Dipl-Ing., Ph.D.

LONDON: HER MAJESTY'S STATIONERY OFFICE
1968
PRICE £1 8*s.* 0*d.* NET

An Experimental Investigation of the Compressible Turbulent Boundary Layer with Air Injection

By L. O. F. JEROMIN, Dipl-Ing., Ph.D.

Reports and Memoranda No. 3526*
November, 1966

Summary.

The compressible turbulent boundary layer on a flat plate with air injection has been investigated experimentally. Boundary-layer developments were measured at Mach numbers of 2·5 and 3·5 for the case of zero injection and each of three different injection rates, with and without heat transfer. The free stream Reynolds numbers were 5×10^7 per meter for a Mach number of 2·5 and $4{\cdot}7 \times 10^7$ per meter for a Mach number of 3·5. All the more interesting boundary-layer parameters like momentum thickness, displacement thickness, boundary-layer thickness, boundary-layer shape parameter and the skin-friction coefficient were determined from the measured profiles and are given in this Report.

1. *Introduction.*

The use of fluid injection into the compressible turbulent boundary layer has wide engineering applications and a considerable number of papers on this topic have appeared in recent years. A critical survey of this previous work is given by Jeromin[3]. However, most of the experimental investigations at supersonic speeds have concentrated on overall drag and heat-transfer measurements and there is a marked lack of detailed measurements of velocity and temperature profile developments. Only one experimental investigation by Danberg has concentrated on detailed local quantities. The present Report describes an experimental investigation of the boundary layer development on a flat plate at Mach numbers of 2·5 and 3·5, with and without injection of air through the porous surface. The influence of heat transfer on the development was studied by pre-cooling the injected air so that the wall temperature could be varied from below recovery temperature to just above it.

This work was undertaken in conjunction with a theoretical investigation[2,4] in which the boundary-layer transformation proposed by Coles[1] has been extended to boundary layers with injection. The limited knowledge of turbulence means that a general theory of the turbulent boundary layer contains at least one element of arbitrariness. This means in practice that every theory is subject to certain integration constants which have to be evaluated empirically from available experimental data. Even boundary-layer transformations like those mentioned above can only be applied when the whole flow field, in at least the transformed flow, is known. These arguments make it clear that experimental studies of the transpired boundary layer are very valuable, especially when they cover a wide Mach number and Reynolds number range.

2.1. *Experimental Equipment.*

The investigation was carried out in the supersonic wind tunnel of the Cambridge University Engineering Department which operates as an intermittent blowdown tunnel. A brief description of the tunnel is given by Jeromin[4]. No steady state condition for the wall temperature can be obtained due to the short

*Replaces A.R.C. 28 549.

running time and to the slight changes of the total temperature; thus the influence of fluid injection on the Stanton number could not be investigated as intended at the beginning of the research.

The Mach number in the wind tunnel can be varied by changing the two solid nozzle liner blocks: two sets of nozzle liners are available, one each for a Mach number of 2·5 and 3·5. The working section is rectangular with the dimensions 0·165 m × 0·114 m. It was decided to halve the working section for the flat plate investigations by using only one nozzle liner. This has the advantage that the running time will be doubled. The lower half of the test section was then used for the injection apparatus.

2.1.1. *The injection apparatus.* The main parts of the apparatus are:

(i) a subsonic nozzle to blend the step from the wall of the settling chamber to the height of the centre-line of the test section which is now identical to the height of the flat plate;

(ii) a solid flat plate for the subsonic region and the region where the flow accelerates to supersonic flow;

(iii) a porous flat plate with a plenum chamber underneath it;

(iv) a traverse gear;

(v) equipment for bringing the injection air into the wind tunnel and for dividing it uniformly throughout the injection area;

(vi) equipment for bringing measuring devices out of the wind tunnel, such as flexible tubes connected to static pressure holes, thermocouple wires, electrical contacts, and the driving device for the traverse gear.

Nearly all the parts were made from mild steel and plated afterwards. The whole injection apparatus is screwed to a mounting plate which sits on the front and back beam of the test section so that it can be removed as a whole from the wind tunnel. The mounting plate rests on small distance pieces so that the slope of the flat plate can be adjusted as necessary to correct the Mach number distribution and to take into account the influence of the boundary-layer development on the expansion of the flow.

The porous section consists of the porous flat plate and the plenum chamber underneath it. The porous plate itself is fixed with small countersunk machine screws to a frame which rests on top of the plenum chamber. O-ring seals between the plenum chamber and the frame and between the frame and the porous flat plate have been used to guarantee an air-tight construction. The dimensions of the frame were made as small as possible, so that the injection area extends as near as possible to the side wall of the wind tunnel in order to minimise three-dimensional effects. The junctions between the front solid plate and the porous plate, and those between the frame and the porous plate, were filled with Cataloy paste and ground afterwards so that a very smooth surface without any steps was obtained. A solid flat plate has been built having exactly the same external dimensions as the frame, so that solid flat plate boundary-layer measurements can be carried out replacing the porous plate by the solid one.

A few more words must be said about the porous plate itself and porous materials in general. Photographs of various porous materials are shown in Figure 2 together with diagrams of their surface roughness. As is well known, the surface roughness has a considerable influence on the skin friction, so this effect must be taken into consideration when a porous material is selected. Another important factor is the uniformity of the porosity along the surface. Consequently a sintered bronze, 'Porosint' (manufactured by Sintered Products Ltd.), was chosen which can be obtained in sheets up to a thickness of 6·35 mm in five different grades depending on the particle diameter allowed to pass, which ranges from $2\frac{1}{2}$ microns for Grade A to $37\frac{1}{2}$ microns for Grade E.

Sintered Products Ltd. provide Porosint Bronze sheets with unfinished or rolled surfaces. The unfinished one is probably a little too rough for an investigation of turbulent boundary layers along permeable surfaces, so that porous plates with rolled surfaces were mainly used in the experiments (*see* diagrams of surface roughness in Figure 2). The porosity of Porosint Bronze and rigid mesh materials is badly impaired if any milling, grinding, or polishing operations are carried out on them. The rolling process must be considered as the best way of ensuring a minimum change of prosity together with a smooth surface. Before the design of the injection apparatus was started an investigation was made of the variation of the porosity within the sheets. Samples were taken from several sheets at various arbitrary positions and turned to a diameter of 63·5 mm. They were then investigated by measuring the pressure

drop Δp across the porous plate in a filtered dry air flow. The mass flow could be varied within a certain range and was measured by the pressure drop at an orifice. The measurements were carried out for samples of Grade A and Grade B both with unfinished or rolled surfaces. The results are shown in Figure 3. There is scatter of the porosity of the order of ± 5 per cent around a mean value so that one must expect a variation of the injection mass flow in the same order of magnitude. It is also apparent from Figure 3 that the rolling process leads to an increase of the pressure drop across the porous surface.

Four porous plates were constructed, together with a solid one, namely:

Plate A made from Porosint of Grade A (maximum particle diameter to pass: $2\frac{1}{2}$ microns) with a rolled surface; injection area: 85·9 mm × 396 mm, 32 thermocouples were fitted into the surface;

Plate B made from Porosint of Grade A with a rough, unfinished surface; injection area: 86·4 mm × 396 mm, 32 static pressure holes were inserted into the surface (only used for static pressure measurements);

Plate C made from Porosint of Grade B (maximum particle diameter to pass: 5 microns) with a rolled surface; injection area: 86·2 mm × 396 mm, 11 thermocouples were fitted into the surface in the region investigated;

Plate D made from Porosint of Grade B with a rough unfinished surface; injection area: 86·6 mm × 395 mm, 11 thermocouples were fitted into the surface in the region investigated.

The wall temperature must be known in order to evaluate the velocity profile from the Mach number profile, as will be shown later. For this purpose thermocouples were installed every half inch along the centreline of the porous plates (for Plate C and Plate D only in the region where boundary-layer traverses have been carried out). The problem was to ensure that only the wall temperature, and not a mean temperature between that in the plenum chamber and the actual wall temperature will be measured. This condition was fulfilled by using the arrangement shown in the sketch on the next page.

Copper-constantan thermocouple wire was chosen for its small dimensions and low price. Each wire was 0·173 mm thick and the overall diameter of both wires with insulation was approximately 0·508 mm. The thermocouple junction was obtained by hard-soldering the thermocouple wire to a small piece of copper wire in order to get an efficient heat conducting contact. The copper contact together with the thermocouple wire was fitted with 'Araldite' into a small ceramic tube of 0·992 mm outside diameter and with a length of approximately 5·08 mm. The ceramic tube was then fitted into the porous plate so that the end with the copper contact protruded slightly above the surface. To avoid any local disturbance of the flow the ceramic tube was finally ground down with a tiny dental grinding machine until it was level with the surface. It was assumed that the thermocouple inserts were small enough not to have any significant influence on the injection mass flow distribution and hence on the boundary-layer development.

The plenum chamber is practically a box with removable ends so that changes inside the chamber can be made easily. Four beams are fixed to the side-wall of the plenum chamber; the upper beams (plate holder) support the frame with the porous plate, and the lower beams (plenum chamber holder) are screwed to the mounting plate. Moreover the four beams are screwed to the front and back supports to give the whole construction more strength and to make it less sensitive to vibration. Inside the plenum chamber rests a second porous plate (filter plate) which is supported by slots in the side walls, and in the removable front and back walls (*see* Figure 4). The purpose of this plate is to divide the injection air uniformly over the surface and to absorb small particles which might have passed the main filter outside the wind tunnel.† Two air inlets in the bottom of the plenum chamber were installed for better diffusion of the injected air. Another reason for this choice was the prospect of further research in the interaction region of turbulent boundary layers with fluid injection and shock waves; here it might be interesting to influence the mass flow behind the shock wave independently of that in front of it. This can be achieved without excessive changes by putting a wall inside the plenum chamber at the position where the shock wave hits the wall. Opposite every air inlet a reflection plate was placed to improve the air distribution. With all these precautions an excellent constant mass flow along the surface was established as shown in Figure 5. The pressure measured by a pitot probe at a height of 0·10 mm above the

†Compressed air was used as injection air so that the dimensions of the air supply lines into the tunnel could be held small.

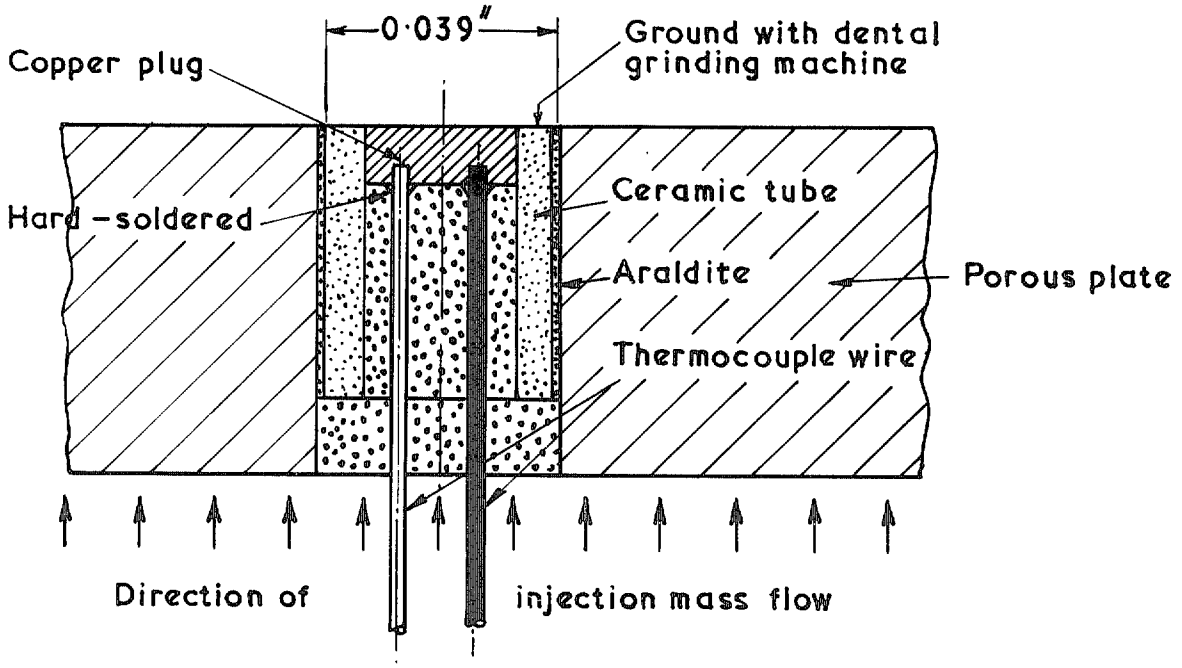

Thermocouple installation

porous surface is plotted in Figure 5 against the actual distance along the porous plate; the zero point coincides with the beginning of the injection at the front part of the apparatus. The overall variation of the mass flow along the surface is of the same order of magnitude as the one found for the test samples. Every point drawn in Figure 5 must be regarded as a mean value evaluated from several readings taken at the same position. This procedure was necessary because the pitot pressure was found to be very sensitive to small deviations in height and to the angle between the pitot probe and the surface.

The back plate with the traverse gear rests on top of the back support (*see* Figure 4). This arrangement was preferred to a traverse gear fixed to the side-wall of the wind tunnel since the latter would probably have become too large and might have caused difficulties in starting the wind tunnel. A special probe and probe holder were designed to cover a large distance along the plate in order to get a reasonable boundary-layer development. Each probe was provided with three fins to strengthen it and to avoid vibrations during the run. It was possible to conduct measurements in its extreme position as shown in Figure 4. The probe with its fins slides in the probe holder and can be fixed with nine screws every quarter of an inch so that boundary-layer traverses in these intervals are possible. The probe holder, as well as the probe itself, was designed so as to give the equipment the necessary strength as well as to keep its drag as low as possible, to avoid difficulties in starting the wind tunnel. This condition was established by turning and milling the probe holder to its final form as shown on Figure 4 (for more details *see* Section 2.13). The probe holder is supported by two shafts in order to reduce any movement of the probe in the flow direction to a minimum. The shafts slide in bronze guide bushes which are fitted in the top and bottom of the box surrounding the traverse gear mechanism. The two shafts are connected by a bridge with a driving shaft at its centre which is joined to the traverse gear drive. The traverse gear drive consists of two universal joints and two small shafts which are connected by a joining part which is used to adjust the length of the traverse gear drive and to correct for small angles between the different parts. The traverse gear drive is connected to a micrometer which can be operated from outside the wind tunnel (*see* Figure 4). The whole traverse gear can be set back and mounted below the second set of two holes in the back plate (*see* Figure 4), should boundary-layer measurements be needed in regions which cannot be covered by the traverse gear in the forward position.

It was decided not to measure the movement of the probe by means of the micrometer, because of possible errors due to any play within the drive. Instead a wiper sliding along a resistor was attached to the bridge and the resistor was connected as a potentiometer. It was found that there is a linear relation between the position of the probe and the voltage picked up by the wiper so that the movement of the probe can be calibrated quite easily by knowing two points of a calibration curve.

The pitot pressure was measured by a pressure transducer with a measuring range from 0 to 5·27 atm absolute. The pressure transducer was screwed to the back of the traverse gear box. It was insulated with a thick layer of paraffin wax in order to prevent spurious pressure fluctuations caused by temperature changes in the surroundings (*see* Green[10]).

Before the experiments were started the whole injection apparatus was checked for leakages by placing the porous plate with the frame against a solid one of identical shape and pumping the apparatus up with air. The pressure inside the chamber stayed constant for at least an hour.

2.1.2. *The air supply.* In addition to the injection apparatus a complete air supply for the injection mass flow was designed. The air for the injection was taken from the tunnel high pressure supply. The system contained the following equipment:

(i) an air filter;

(ii) a heat exchanger to pre-cool the air if wanted and to vary the air temperature within a certain range;

(iii) equipment to measure and control the mass flow.

Photographs of the air supply together with the wind tunnel and the injection apparatus are presented on Figure 1. A schematic diagram of the air supply is shown on Figure 6.

The injection air enters the filter at a temperature of about 295°K and a constant pressure of 13·70 atm. The filter was essential to protect the porous plates inside the injection apparatus against blockages which might be caused by small dust and oil particles produced by the compressors which feed the wind tunnel 68·5 atm supply pipe and which have passed through the main tunnel filters. The pressure is then reduced downstream of the filter by a reducing valve to the pressure necessary to inject a given mass flow through the porous surface. This pressure, indicated by a manometer gauge for easy adjustment, is a function of the pressure lost in the whole air supply system and the injection apparatus, hence of the mass flow itself, as well as the static pressure inside the wind tunnel.

In order to investigate the influence of heat transfer on the boundary-layer development it was necessary to vary the temperature of the injection mass flow within a certain range. Only the possibilities of pre-cooling the air have been investigated since it is more useful to investigate the influence of heat transfer from the flow to the wall. This case corresponds to the practical application of transpiration cooling. Considering the short running time of the wind tunnel a charge system was chosen instead of a continuous cooling process. It was decided to use a shell and tube heat exchanger, with the air to be cooled inside the pipes and the cooling medium around it. A suitable cooling medium was found in a dry ice-acetone mixture. The dry ice (solid CO_2) sublimates at a constant temperature of $T_s = -78{\cdot}5$°C and $p_s = 1$ atm. The acetone is used as a medium to increase the heat transfer to the pipe since the free convection of gaseous CO_2 developed by the sublimation process would result in a very small heat-transfer coefficient and hence a very large heat exchanger.

It is useful to be able to vary the temperature between T_1 and T_5 (*see* Figure 6). This was achieved by attaching a mixing chamber to the heat exchanger in which uncooled and cooled air can be mixed. The mass flow was divided behind the reducing valve, one part (m_1) passes through the heat exchanger and the rest (m_2) by-passes it. The mass flow can be varied in each direction by means of two needle valves. To give an example, the mass flow through the by-pass can be increased by opening needle valve II and closing simultaneously needle valve I by about the same amount so that the total mass flow $m = m_1 + m_2$ remains constant. The pressure loss of the air supply will be slightly changed by this procedure so that the total mass flow must be adjusted with the reducing valve. Thermocouples were installed to measure the inlet temperature T_1, the temperature inside the heat exchanger T_2, the temperature inside the mixing chamber T_4 and the outlet temperature. The whole apparatus was insulated with glass wool.

The injection mass flow was measured by means of an orifice through which the flow passes after leaving the mixing chamber. At the orifice the differential pressure Δp_c and the pressure p_c and the temperature T_c can be recorded. The differential pressure was measured by means of a manometer calibrated in mm of alcohol and designed to stand high pressures, whereas the pressure p_c was read from an accurate manometer gauge. The temperature T_c was assumed to be the same as T_5 which is a reasonable approximation because of the short distance between T_5 and T_c and the insulation. The mass flow was now divided between the two air inlets on the bottom of the injection apparatus inside the wind tunnel. The mass flow in each line can be determined by means of an orifice in the line; and varied, with the help of two needle valves connected to either line. The two lines end in a flexible Nylon tube with a joining part fitted to their end which can be connected to the wind tunnel.

In view of the short running time of the wind tunnel it was necessary to make reading of the various experimental data as quickly as possible by using automatic devices like thermocouple switches and X-Y plotters to record the temperatures and pressures. Parts of the instrumentation can be seen in Figure 1. The details of the test programme will be described later.

2.1.3. *The boundary-layer probes.*Three boundary-layer probes were designed: one pitot probe for the determination of the pitot pressure profiles along the centreline of the wind tunnel, a second for the region one inch to one side of the centreline, and a temperature probe for the evaluation of the boundary-layer temperature profiles along the centreline. A picture of the probes is shown on Figure 7.

The pitot probes were fabricated from hypodermic tubing of 1·068 mm outside diameter which was flattened at the tip to a height of 0·204 mm. Structural stiffness was obtained by soldering the tube into a slightly bigger one of 1·65 mm outside diameter which was fixed to a brass tube of 6·25 mm outside diameter. This brass tube was fitted with three fins, and is the main support of the probe as already described in Section 2.1.1. In view of the overall length of the probe of 292 mm, it was necessary to make the effective volume inside the probe as small as possible in order to keep the time lag in the system within reasonable limits. This condition was fulfilled by using only the hypodermic tubing with the smallest diameter of 1·067 mm as working space all along the probe. The end of the probe was connected with plastic tubing (its length depends on the position of the probe) to the transducer. The response time of the whole system in its extreme position as shown on Figure 4 was found satisfactory when the pressure was changed rapidly and the response time checked on the X-Y plotter.

The most promising methods for determining the temperature variation through the boundary layer are the total temperature probes proposed by Goldstein and Scherrer[5] and Langworthy[6] and those used for example by Danberg[7], Winkler[8] and Bradfield *et al.*[9]. The principle of a total temperature probe is the practical application of the adiabatic compression of a flow when passing through a normal shock wave. The flow then moves at a low velocity past a thermocouple fitted to the inside of the probe. But as the size of the probe becomes smaller the thermocouple tends to indicate the external surface temperature, and the measurements become rather doubtful. Static temperature measurements within boundary layers require a small design of probe for predicting local temperatures. For these purposes, a different kind of probe seems to be more reliable. Their application is based on the known flow pattern around small obstacles of well-defined geometrical shape, (such as wedges (Bradfield[9]) or cones (Danberg[7])), in supersonic flow by measuring the temperature of the obstacle. The static temperature in front of the obstacle with its oblique shock wave can be evaluated in a simple way from the temperature indicated by a thermocouple soldered to the wedge or cone, with the aid of oblique shock tables when the Mach number is known.

A temperature probe very similar to that proposed by Danberg was used for the temperature measurements. A stainless steel cone with an angle of 10°, a maximum diameter of 1·527 mm and approximately 8·90 mm long was fitted with Araldite to a ceramic tube with an outside diameter of 1·577 mm and a length of about 25·4 mm. A copper-constantan thermocouple was hard-soldered to the cone to indicate its temperature. The ceramic tube was fitted to a wedge which was soldered to a brass tube with three fins to give the necessary strength to the probe. The dimensions of the brass tube and the fins are identical with those of the pitot probe. A ceramic tube was selected to support the cone in order to reduce the heat conduction from the wedge to the cone. Moreover, a second thermocouple was installed into the

wedge to correct the temperature indicated by the cone for possible heat conduction effects. These effects were found to be negligible, at least in the temperature range investigated.

2.2. *Test Procedure.*

From earlier investigations (*see* Green [10]) it was known that the boundary layer is turbulent for zero injection in the region investigated. The experiments were carried out at two Mach numbers, namely at $M_\infty = 2{\cdot}5$ and $M_\infty = 3{\cdot}5$. A stagnation pressure of $P_0 = 5{\cdot}225$ atm was chosen for the tests at $M_\infty = 2{\cdot}5$. The tests at a nominal Mach number of 3·5 were carried out at a stagnation pressure of 8·30 atm, because it was impossible to start the wind tunnel below this pressure. The nominal working section Reynolds number per unit length was approximately 5×10^7 (1/m) for $M_\infty = 2{\cdot}5$ and $4{\cdot}75 \times 10^7$ (1/m) for $M_\infty = 3{\cdot}5$. It was the aim of the experiments to obtain Mach number and temperature profiles at various positions along the plate. A distance of 0·110 (m) along the plate can be covered with the pitot and temperature probe. Ten boundary-layer traverses were made within this distance so that a momentum thickness development could be evaluated from the measured profiles, which was essential to find the skin-friction coefficient with reasonable accuracy. The Mach number profiles were obtained by connecting the pitot probe to the pressure transducer and by putting the output of the transducer on the first Y-channel of the two-channel X-Y recorder. The wall temperature was recorded on the second Y-channel. The output of the potentiometer, which indicates the position of the probe within the boundary layer, was used as the X-input for the X-Y recorder. With this arrangement it was possible to measure a whole pitot pressure profile within 30 to 45 seconds depending on its thickness. The stagnation temperature was read every ten seconds on a 'Scalamp' galvanometer during every boundary-layer traverse so that any irregularity could be taken into account when the profiles were analysed. All the experiments can be divided into four categories:

(i) Mach number profile along solid flat plates $T_w > T_r$
(ii) Mach number profiles along porous plates with $T_w > T_r$
(iii) Mach number profiles along porous plates with $T_w \approx T_r$
(iv) Mach number profiles along porous plates with $T_w < T_r$.

Various porous plates have been used for the transpired boundary layers.

The solid flat-plate boundary-layer measurements were conducted by replacing the porous plate by a solid plate as described in Section 2.1.1. Its wall temperature was indicated by a thermocouple which was fitted into the plate. Static pressure holes of 0·25 (mm) outside diameter were drilled into the surface to measure the static pressure variation along the plate; but it was found to be more reliable to evaluate the static pressure from the stagnation and pitot pressure outside the boundary layer which could be measured with more accuracy, especially for flow with fluid injection. The pressure transducer, as well as the potentiometer of the traverse gear, were calibrated before every run.

Three sets of tests were carried out with fluid injection using three different porous plates: two plates with different grades and a smooth surface, and one plate with a rough surface (*see* Section 2.1.1). The wall temperature was changed from $T_w = 250°\text{K}$ to $T_w = 286°\text{K}$ for every set of Mach number profiles along the plate, so that profiles with and without heat transfer were obtained. Calibrated thermocouples were installed along the centreline of the porous plate half an inch apart in the region investigated. Mach number profiles were measured at a position half way between two thermocouples. The temperature indicated by these thermocouples was recorded during the run on X-Y recorders. Both thermocouples indicated virtually the same temperature. Two typical examples of pitot pressure profiles are shown on Figure 8 (zero injection, $M_\infty = 3{\cdot}5$) and Figure 9 ($F \approx 2 \times 10^{-3}$, $M_\infty = 3{\cdot}5$).

The injection mass flow was measured by means of an orifice which was calibrated by means of a gas meter under exactly the same conditions as they occur during the experiments in order to suppress possible Reynolds number effects on the calibration. It must be stressed here that all the quantities necessary to determine a boundary-layer profile were recorded every ten seconds, and were virtually constant. They were mainly recorded at these intervals to consider unforeseen irregularities during a run. The run was always repeated when big deviations were observed during a run.

When pre-cooled air was injected through the porous plate to obtain a wall temperature at recovery conditions, or below, the measurements were started only when a steady wall temperature was reached

along the plate. The wall temperature could be measured for Plate A also one inch on either side of the centreline. These temperatures were virtually the same as those indicated for the centreline. For low wall temperatures in the order of 250°K the steady state condition was reached after about half an hour. Some pitot pressure profiles were measured one inch off the centreline to investigate three-dimensional effects on the boundary-layer growth. The experimental procedure was the same as that used to measure along the centreline.

The temperature profiles were measured with the temperature probe described in Section 2.1.3. All the thermocouples mentioned above were calibrated inside the wind tunnel after the wind tunnel had not been used for at least two days and one could be assured that the temperature inside was constant and identical to the room temperature.

2.3. *Data Reduction.*

The experimental data were analysed by the Titan computer in the Mathematical Laboratory of the University of Cambridge. For this purpose a programme was written in Autocode language which evaluated the velocity profile†, $Y_T = \int_0^y \frac{\rho}{\rho_w}\, dy$, and the boundary-layer parameters θ, δ^* and H from the co-ordinates of the pitot pressure profile (as they were read from the X-Y recorder and punched on tapes). One boundary-layer profile could be analysed with this programme in two seconds. Moreover the skin-friction coefficient c_f and co-ordinates in the transformed planes using Coles'[1] and Jeromin's[2] boundary-layer transformations (*see* Appendix A) were evaluated simultaneously by feeding transformation parameters into the computer. The calculations were carried out as follows. The static pressure was evaluated from the pitot pressure outside the boundary layer and the stagnation pressure because of the uncertainty of static pressure measurements with fluid injection§. The free stream velocity u_∞ follows from p_∞ and T_∞. The Mach number profile was then calculated from the co-ordinates on the X-Y recorder graph using Raleigh's formula for supersonic flow and the corresponding formula for subsonic flow.

The static temperature has to be known in order to evaluate the velocity from the Mach number. Some static temperature profiles were calculated from measured stagnation temperature profiles for various injection rates and are compared in Figures 10 to 13 with the temperature formula

$$T = T_w - (T_w - T_r)\left(\frac{u}{u_\infty}\right) - (T_r - T_\infty)\left(\frac{u}{u_\infty}\right)^2, \tag{2.1}$$

---

†No correction for possible displacement effects was considered, since it is rather doubtful whether the displacement effects in their usual form for measurements with pitot probes in incompressible flow, still holds for compressible supersonic flow with a shock wave in front of the pitot probe. Green[38] investigated the effect of different opening diameters for the pitot probes in the same wind tunnel at similar stagnation conditions. He found no effect of the size of the pitot probe on the Mach number profile for the range of probe sizes investigated. But it cannot be concluded if there is a displacement effect or not. This must be the subject of a separate investigation.

§ Static-pressure measurements with fluid injection were carried out measuring the static pressure along the plate by means of static pressure holes in the surface. The static pressure holes were obtained by drilling small holes into the porous plate and fitting hypodermic tubing with Araldite into them. Unfortunately it was found that the measurements were not accurate enough because of the difficulties of making the edge of the tubing level with the surface of the plate which could not be realised with the necessary accuracy for all the 32 pressure holes.

which was proposed by Spence[12], Crocco[13] and Van Driest[14]†. The agreement in Figures 10 to 13 for various injection rates between experiment and Eq. (2.1) can be regarded as satisfactory, so that the Spence formula was used for the further analysis of all the boundary-layer profiles, instead of measuring the temperature profile for each profile. Similar satisfactory agreement was found by Danberg[15] for transpired compressible boundary layers at a Mach number of 6·2. The only difficulty in the application of the temperature formula is how the recovery factor is affected by fluid injection. There is scarcely any reasonable theoretical information available, so Bartle and Leadon's experimental data[16] for Mach numbers of 2·0 and 3·2 were used instead. Their data were analysed by plotting r/r_o (r_o is the recovery factor without injection) against F in Figure 14 and so extrapolating and interpolating their experimental results linearly to the two Mach numbers investigated.

The local velocity within the boundary layer was then calculated from the Mach number. When the temperature and velocity variations were known, the co-ordinate

$$Y_T = \int_o^y \frac{\rho}{\rho_w} dy = \int_o^y \frac{T_w}{T} dy, \tag{2.2}$$

(which will be used in a similar form by all boundary-layer transformations), the momentum thickness

$$\theta = \int_o^\delta \frac{\rho u}{\rho_\infty u_\infty} \left(1 - \frac{u}{u_\infty}\right) dy, \tag{2.3}$$

the displacement thickness

$$\delta^* = \int_o^\delta \left(1 - \frac{\rho u}{\rho_\infty u_\infty}\right) dy, \tag{2.4}$$

the boundary-layer shape parameter

$$H = \delta^*/\theta, \tag{2.5}$$

and the boundary-layer thickness δ for $u/u_\infty = 0{\cdot}995$ were evaluated simultaneously by the same programme. The integrations were performed numerically using small step lengths. The Reynolds number R was calculated using Sutherland's formula for the viscosity, namely

$$\mu = \frac{T_s + 117}{T + 117} \left(\frac{T}{T_s}\right)^{3/2} \mu_s, \tag{2.6}$$

with reference value at standard conditions of $\mu_s = 6{\cdot}178 \times 10^{-2}$ (kg/m.h) at $T_s = 273{\cdot}15°K$. There were slight changes of the Reynolds number along the plate due to very small pressure gradients and unavoidable changes of the stagnation conditions, so that a mean value R was evaluated for each boundary-layer development. The further calculations to determine R_x and R_θ are based on R. Another problem was the determination of the virtual origin of the turbulent flow. For boundary layers with

†Spence's formula was derived for compressible boundary layers without injection, and it was necessary to check whether Eq. (2.1) holds for flow with fluid injection as well. The static temperature profiles were evaluated from the measured local total temperature which was indicated by the cone. The Mach number distribution through the boundary layer was known from pitot pressure measurements. Hence the local Mach number behind the oblique shock wave of the cone can easily be determined with the help of graphs for conical flow (*see* for example Rosenhead *et al*[23]). The static temperature can then be calculated from the local Mach number and local temperature using isentropic flow tables.

zero mass transfer the mean slope method proposed by Rubesin, Maydew and Varga[17] was applied for both Mach numbers (*see* Figure 15). With fluid injection a plot θ against x (*see* Figures 16 and 17) was used to estimate the virtual origin by extrapolating the curves to $\theta = 0$.† This method is certainly not highly accurate and must rather be considered as an approximate approach in the absence of a more reliable method. Calculations were made to determine the skin friction coefficients at $M_\infty = 2{\cdot}5$ and $M_\infty = 3{\cdot}5$ using several theories for boundary layers without injection. Mager's and Spence's boundary-layer transformations were applied to Ludwieg/Tillmann's skin-friction law[19] (*see* Appendix A) for incompressible flow. Finally Sommer and Short's T'-method[21] has been used to predict the variation of c_f with R_x or x for the two Mach numbers investigated. These results are presented in Figures 20 and 21 where theoretical and experimental skin-friction coefficients are compared for the case of zero injection.

All the data are presented in the form of tables to facilitate further analysis since the existing experimental data were found to be much less easy to use when published only as graphs. The contents of the tables are explained in Appendix A. The summary tables containing the main boundary-layer parameters are included in this Report whereas the tables of the boundary-layer profiles themselves can be obtained from the Department of Engineering, University of Cambridge (Dr. L. C. Squire).

2.4. *Accuracy.*

A calculation to determine the errors for all the data given in the tables becomes rather difficult in view of the complexity of the measuring technique, and the amount of analysis performed on the data itself. The possible errors for the momentum and displacement thickness were evaluated by feeding into the computer the possible deviations from a measured mean value for every quantity necessary to calculate θ and δ^*. These deviations were changed systematically until the worst configuration was obtained, which predicted an error of about ± 1 per cent for θ and $\pm 1{\cdot}5$ per cent for δ^* so that the quoted values for the boundary-layer shape parameter H might be subject to an error of the order of ± 4 per cent. It is even more difficult to predict an error for the skin-friction coefficient when it is evaluated from the momentum equation because of the evaluated error for θ itself and slight changes of the injection mass flow as well as the Reynolds number per unit length which might influence the θ development in an unknown order of magnitude†. A reasonable estimate might be an error of ± 8 per cent for c_f up to a value of $F \simeq 1{\cdot}2 \times 10^{-3}$ for both Mach numbers. The error is certainly much bigger for the highest injection rate of $F \simeq 2 \times 10^{-3}$ for $M_\infty = 3{\cdot}5$. For the last case, an error of ± 50 per cent for the skin-friction coefficient is not impossible in view of the scatter for the momentum thickness. Even the pressure gradient term becomes dominant here for the evaluation of the skin-friction coefficient from the momentum equation. The error in the injection mass flow parameter F is about 1 per cent.

In estimating potential errors for the boundary-layer parameters, a most important factor is the possibility of three-dimensional effects such as cross-flows on the boundary-layer growth. Several boundary-layer profiles were measured, one inch on either side of the centreline of the wind tunnel along the porous plates, for a Mach number of 3·5. The momentum thickness and displacement thickness evaluated from these boundary-layer profiles deviate only minutely from those obtained along the centreline. The differences are only of the order of ± 2 per cent for θ and δ^*, so that the more or less expected three-dimensional effects seem to be in reasonable proportions to treat the boundary layer as two-dimensional (*see* also the next Section).

By considering the accuracy of the transducer and the X-Y recorder, and by allowing for reading errors, it is estimated that the non-dimensional velocities in the boundary layer (i.e. u/u_∞) are accurate

†Figures 16 and 17 suggest for the case of zero injection that the curves have to be bent in order to obtain the same virtual origin as predicted by Rubesin's *et al* method. This is the only justification why the curves are bent for the case of air injection as well.

†This second source of error has a considerable effect on the θ-development and hence on the skin-friction coefficient itself.

to $\mp 0{\cdot}001$. However, the tabulated values were taken directly from the computer output and are quoted to more decimal places than is strictly justified.

3. *Discussion of Results.*

3.1. *Experimental Results.*

Typical velocity profiles u/u_∞ against y/δ are plotted in Figures 22 and 23 for the two Mach numbers investigated and various injection rates. These diagrams were mainly drawn to give some idea of the influence of air injection on the velocity profiles. The velocity profiles drawn on each diagram were measured at the same station. Three different injection rates are always compared with a boundary layer measured on a solid flat plate. The injection process deforms the boundary layer similarly to the effect of adverse pressure gradients on boundary layers without transpiration. The deformation of the profile results in a reduction of the skin-friction coefficient and the reduction increases with increasing injection mass flow parameter F, as is apparent from the shape of the boundary-layer profile in Figures 22 and 23.

The influence of air injection on the boundary-layer profile seems to be less significant for a Mach number of 2·5 than for a Mach number of 3·5 when comparing Figure 22 with Figure 23. First of all a far bigger injection range is investigated at $M_\infty = 3{\cdot}5$ so that bigger deformations of the profile have to be expected. Other parameters influencing the shape of the profile apart from the mass transfer at the wall are the wall and free stream temperature and pressure gradients. Adverse pressure gradients, cooling of the wall and fluid injection shift the profiles to the left in Figures 22 and 23 whereas favourable pressure gradients, heating of the wall, and suction, create shifts of the profiles to the right hand side in the diagrams. The unavoidable slight pressure gradients are mainly responsible for the fact that the outer part of the profile at $M_\infty = 2{\cdot}5$, $F \simeq 0{\cdot}7 \times 10^3$ and $F \simeq 1{\cdot}2 \times 10^{-3}$ (*see* Figure 22) lie much closer together than one would expect. As one can see in Figure 24 the profiles with $F \simeq 0{\cdot}4 \times 10^{-3}$ and $F \simeq 0{\cdot}7 \times 10^3$ lie in an adverse pressure gradient (shift to the left in Figure 22) whereas the profile with $F \simeq 1{\cdot}2 \times 10^{-3}$ lies in a favourable pressure gradient (shift to the right). These different pressure gradients† cause deformations such that the outer part of the profiles with the two highest injection rates measured at station 60 to 90 (*see* Appendix A) even overlap each other. On the other hand all profiles at $M_\infty = 3{\cdot}5$ are measured in a region of adverse pressure gradient. The order of magnitude of this adverse pressure gradient is barely affected by the process of fluid injection.

For the highest injection rate of $F = 2{\cdot}111 \times 10^{-3}$ at a Mach number of 3·5 the deformation has reached a point where it is difficult at the measuring stations further downstream to determine, with sufficient accuracy, the point where the pitot probe touches the wall, because the Mach number variation close to the wall has become extremely small, causing fluctuation of the pitot pressure (*see* Figure 25). It could not be decided whether the boundary layer has separated at the station 100 for the Run $3{\cdot}5-2.1-1.100$ (*see* Appendix A) since the boundary-layer slope at the wall could not be measured. It seems as if the boundary layer is blown off at this point. Scott *et al*[22] found from their experiments that turbulent separation occurs at $FR_x^{\frac{1}{2}} = 0{\cdot}06$ for a Mach number of $M_\infty = 3{\cdot}0$, but unfortunately they did not specify how they defined their point of separation. Evaluating the product $FR_x^{\frac{1}{2}}$ for Run $3{\cdot}5-2{\cdot}1-1{\cdot}100$ (*see* Appendix A) would result in a value of 0·061; a value very close to the one predicted by Scott *et al*[22]. But it must be stressed here that it cannot be decided from the present measurements whether separation occurs or not. It is quite possible that the skin-friction coefficient has a finite value and that it is difficult to measure the Mach number profile close to the wall because of the fluctuating pitot pressure. An argument for this interpretation of the measured data is the momentum thickness development up to Station 70 (Run $3{\cdot}5-2{\cdot}1-1{\cdot}70$) which predicts a finite skin-friction coefficient, with reasonable credibility. It seems very unlikely that the skin friction coefficient would suddenly drop to zero without a blending region between. More experimental information must be obtained before a final conclusion can be drawn.

---

†The measurements with injection rates $F \simeq 1.2 \times 10^{-3}$ were carried out under slightly modified conditions by changing the slope of the porous flat plate and so influencing the expansion in the supersonic nozzle.

The most important boundary-layer parameters θ, δ^* and H are plotted in Figures 26 to 31 against the co-ordinate x for all measurements with and without heat transfer.

There is only a slight scatter for the values of the momentum and displacement thickness, whereas the values for the boundary-layer shape factor H sometimes indicate larger deviations from a mean value. As for the case of zero injection the momentum and displacement-thickness increase roughly linearly with x, but the slopes $d\theta/dx$, $d\delta^*/dx$ increase with increasing injection rate. The boundary-layer shape parameter H decreases with x.

Cooling of the wall (experiments with $T_w \simeq T_r$ and $T_w < T_r$) reduces the displacement thickness and the boundary-layer shape parameter (compared with the experiments at $T_w > T_r$) but increases the momentum thickness in a much smaller degree. But it must be stressed here that the heat-transfer effect is fairly small, since the wall temperature does not deviate very much from the recovery temperature T_r because the temperature of the injection mass flow could be only varied in the range $(T_r - 30) < T_r$ (°C) $< (T_r + 30)$. Danberg[15] had facilities for investigating the influence of heat transfer on the transpired boundary layer at a hypersonic Mach number of 6·7, by changing the ratio of the wall to free stream temperature T_w/T_∞ from 4·1 to 7·6 (for comparison the value $T_r/T_\infty = 8$ for his investigation). He found the same tendencies for δ^* and H when the wall was cooled, with the momentum thickness increased for decreasing T_w/T.

Plate A and Plate C are almost interchangeable, as shown in Figures 26 to 28. The slight differences between θ, δ^* and H measured along Plate A and Plate C are mainly due to slight changes in the stagnation temperature and the stagnation pressure, and are not caused by the differences of porosity, (expressed by the different grades) of the plates. The influence is also small for the rough plate (Plate D) as demonstrated on Figures 29 to 31, especially for high injection rates. The insignificant disagreements are also caused by slightly higher injection rates F for the experiments with Plate D.

Finally the skin-friction coefficient was evaluated from the momentum development using the momentum equation for compressible flow

$$\frac{c_{f1}}{2} = \frac{d\theta}{dx} - F - P \tag{3.1}$$

with

$$P = \frac{\theta}{\rho_\infty u_\infty{}^2} \frac{dp}{dx} (2 + H - M_\infty^2) . \tag{3.1.1}$$

The calculations were carried out by plotting θ against the actual distance along the plate measured from the critical dimension of the nozzle and evaluating the slope $\frac{d\theta}{dx}$. Only typical examples will be presented here (*see* Figures 18 and 19). The static pressure and Mach number variation along the region of the plate investigated were plotted on the same figures so that their influence on the θ-development can be studied. The slight scatter for θ is caused mainly by the variations of the static pressure, as one can see in these diagrams. No correction for the effect of static pressure gradients was made for the skin-friction calculation for the experiments at a Mach number of 2·5, as only those points of the θ-development were considered where the static pressure was virtually constant. A slightly adverse pressure gradient (*see* Figure 19) could not be avoided for the experiments at the Mach number of 3·5 so that all the skin-friction values derived from the momentum equation are corrected for the effect of the pressure gradient term (3.1.1). This correction term P is quite small compared to the term $\left(\frac{d\theta}{dx} - F\right)$ and is approximately $-0{\cdot}05 \times 10^{-3}$† for all momentum-thickness developments.

†The pressure gradient term P of the momentum equation is negative for an adverse pressure gradient since $M_\infty^2 > 2 + H$.

Evaluating the skin-friction coefficient for $M_\infty = 3{\cdot}5$ from the momentum equation, including the adverse pressure gradient term, results in a value for the case of zero injection which is about $D = 0{\cdot}02 \times 10^{-3}$ too high compared with other experimental investigations (*see* Figure 21), whereas for a Mach number of 2·5 the skin-friction coefficient evaluated from the momentum equation agrees very well with other experimental investigations (*see* Figure 20). The most likely explanation for the discrepancy at $M_\infty = 3{\cdot}5$ is a slightly three-dimensional effect. The good agreement between the experimental data for the skin-friction coefficient at a Mach number of 2·5 suggests that the three-dimensional effect at $M_\infty = 3{\cdot}5$ is probably caused by the continuous adverse pressure gradient at that Mach number. Consequently the skin friction coefficient for all the boundary-layer developments at $M_\infty = 3{\cdot}5$ must be corrected for the three-dimensional influence. This correction term has been determined assuming that the contribution of the three-dimensional effect to the momentum balance is unaffected by fluid injection and hence is the same as for zero injection, namely the difference $D = 0{\cdot}02 \times 10^{-3}$ between the value of the skin-friction coefficient determined from the momentum equation and the value measured by Matting *et al*[26], which is very accurate since it was measured by the floating element technique. It follows, then, that the skin-friction coefficient at $M_\infty = 3{\cdot}5$, including the three-dimensional effect, is given by

$$\frac{c_{f1}}{2} = \frac{d\theta}{dx} - F - P - \frac{D}{2}.$$

The pressure gradient term P as well as the three-dimensional term is very small compared to $\frac{d\theta}{dx}$ and F. Unfortunately $\frac{d\theta}{dx}$ and F are of the same order of magnitude so that the relatively small terms P and D have a significant influence on the value of the skin-friction coefficient. All the skin-friction values c_{f1} derived from the momentum equation are summarised in column 26 of the Tables II to XVI. The value for the skin-friction coefficient at a Mach number of 3·5 uncorrected for three-dimensional effects has been tabulated in brackets underneath the corrected value (*see* column 26).

From the results for the skin-friction coefficient it can be deduced that the boundary layer is virtually the same whether Plate A (Porosint of Grade A) or Plate C (Porosint of Grade B) were used during the experiments, since the skin-friction coefficients are about the same within the accuracy of the measurements (*see* column 26 in Table V–0 and Tables XVI–0 and Figure 32). The use of a plate with a rough surface (Plate D) has some influence on the skin-friction coefficient for smaller injection rates. Comparing the values for c_{f1} in column 26 in the Tables VII–0, IX–0 and XIV–0, XV–0, respectively (*see* Figure 32) one realises that the skin-friction coefficient has increased in the order of 15 per cent for the boundary layer measured along Plate D (Grade B, rough surface) compared to that obtained for a smooth surface. This increase of c_{f1} is also partially caused by a slightly smaller injection rate F for the experiments with Plate D. At higher injection rates (*see* Figure 32) the choice of the plate becomes unimportant, since the skin-friction coefficients evaluated from a boundary layer measured along a smooth porous plate (Plate C, Table IX–0, Figure 32) and along a rough porous plate (Plate D, Table XV–0, Figure 32) are approximately the same. No well defined influence of heat transfer on the skin-friction coefficient can be deduced from the θ-developments for the boundary layers with a cooled wall. The influence of heat transfer on $d\theta/dx$ is negligible, at least for the temperature range investigated, as can be found comparing the skin-friction coefficients in column 26 of the Tables II–0 to XIII–0 (*see* Figure 32). This result is not very surprising in view of the small overall change of the wall temperature (in the order of 50°C). Skin-friction measurements along solid flat plates with heat transfer have shown that only severe heating or cooling have significant effects on the skin-friction coefficient; so that only further experiments, where the wall temperature can be changed through a much bigger range than was possible with the experimental facilities used in the present investigation would clarify the situation. Danberg[15] measured skin-friction coefficients under the influence of heat transfer. Unfortunately his data for c_f show such a scatter that no final conclusion can be drawn from them.

3.2. *The Application of Boundary-layer Transformations to the Measured Profiles.*

The main features of Coles' and Jeromin's transformations are described in Ref. 1 and Refs. 2 and 4 respectively. These two transformations have been used to analyse the measured compressible boundary layers by comparing them with well-established formulae for incompressible flow like the 'law of the wall'

$$\frac{u^*}{u_\tau^*} = \frac{1}{\kappa} ln \frac{y^* u^* \rho^*}{\mu^*} + C \tag{3.2}$$

for boundary layers along smooth solid walls and Stevenson's law[18] for transpired layers.

$$\frac{2\mu_\tau^*}{v_w} \left[\sqrt{1 + \frac{v_w^* u^*}{u_\tau^{*2}}} - 1 \right] = \frac{1}{\kappa} ln \frac{y^* u^* \rho^*}{\mu^*} + C \tag{3.3}$$

with κ and C constant. The 'law of the wall' and Stevenson's law can be considered as formulae defining u_τ^* and hence $c_f{}^*$ for a given boundary-layer profile. The concept was used to determine the skin-friction coefficient for the compressible boundary layers by transforming the measured quantities u and y into their corresponding incompressible form and evaluating u_τ^* from Eq. (3.2) or Eq. (3.3) respectively. The friction velocity u_τ^* is constant where the 'law of the wall' holds. Its value was used to determine the skin-friction coefficient from the definition equation writing

$$c_f{}^* = \frac{2(u_\tau^*)^2}{u_\infty{}^2}. \tag{3.4}$$

The compressible skin-friction coefficient follows from the incompressible one, again using the transformation.

A problem was the choice of the constants κ and C in (3.2) and (3.3) since there is a considerable amount of disagreement in the literature regarding their actual value. Coles' values $\kappa = 0{\cdot}410$ and $C = 5{\cdot}00$ were chosen mainly because they are good mean values (for the scatter in the literature *see*, for example, Black and Sarnecki[24]).

Measured boundary-layer profiles at Mach numbers of 2·5 and 3·5 and each of three different injection rates are plotted in the transformed stage in Figure 33 in Stevenson's co-ordinates. The skin-friction coefficient used in this diagram is c_{f2} and not c_{f1} (which was evaluated from the momentum equation). The skin-friction coefficient c_{f2} was determined as the best fit to Stevenson's law and is tabulated in column 27 of the Tables II to XVI. The fully turbulent part of the compressible boundary-layer profile with air injection has been reduced to Stevenson's 'law of the wall' for incompressible flow. This collapse is not as good for the highest injection rate at $M_\infty = 3{\cdot}5$. But this profile is nearly separating (blown-off) so that it is rather surprising that it could be reduced at all. A collapse for the outer part of of the compressible profile cannot be expected from a plot like the one presented in Figure 33 since the transformed flows correspond to different Reynolds numbers R_x^* and R_θ^*.

Finally the values for the skin-friction coefficients c_{f1} (determined from the momentum equation), c_{f2} (determined from the 'law of the wall' in connection with Coles' and Jeromin's transformation) and c_{f3} (determined from an empirical relation in connection with Jeromin's transformation, *see* Appendix A) will be compared with each other (*see* Table I, the values for c_{f2} and c_{f3} are mean values evaluated from those tabulated in the columns 27 and 28 of the Tables II–0 to XVI–0). The agreement between the skin-friction coefficient predicted by the transformation and those calculated directly from the momentum

equation is very good for all injection rates investigated.† There is also an excellent agreement for the skin-friction coefficients at $M_\infty = 3{\cdot}5$ when the comparison is based on those values which are calculated from the momentum equation taking into consideration the correction for the slight three-dimensional effect as already described. Moreover, one has to consider that the error for the skin-friction coefficient determined from the momentum equation increases with increasing injection rate because the difference between $d\theta/dx$ and F becomes very small. The estimated error Δc_{f1} for the skin-friction coefficient c_{f1} is included in Table I. The possible error is considerable, especially for the highest injection rate at a Mach number of 3·5 where the boundary layer is nearly blown off. As mentioned before there is a slight adverse pressure gradient along the test section for the experiments at a Mach number of 3·5 so that the 'law of the wall' would probably predict a slightly smaller value for the skin-friction coefficient than for zero pressure gradient. The pressure gradient is probably responsible for the fact that Stevenson's 'law of the wall' predicts a slightly lower skin-friction coefficient than Eq. (A.1). Finally c_f/c_{f_o} is plotted against $2F/c_{f_o}$ on Figure 34, showing that the data of the present experimental analysis are consistent with the results of other investigations. It can be deduced from this Figure that the author's boundary-layer transformation in connection with Stevenson's law is the only theoretical approach which predicts the correct order of magnitude of the Mach number influence on the skin-friction coefficient.

4. *Conclusions.*

4.1. Compressible boundary layers with air injection have been measured at Mach numbers of 2·5 and 3·5 with free stream Reynolds numbers of 5×10^7 and $4{\cdot}7 \times 10^7$ per meter respectively. The stagnation temperature was about 295°K whereas the wall temperature varied from 240°K to 285°K.

4.2. The boundary-layer parameters θ, δ^*, δ, H, R_θ, R_x have been evaluated for these profiles and are tabulated. Tables of the boundary-layer profiles can be obtained from the Engineering Department, University of Cambridge.

4.3. It was shown that the fully turbulent part of a compressible boundary-layer profile can be reduced to a corresponding incompressible flow in the region where the 'law of the wall' applies.

4.4. The skin-friction coefficient c_f evaluated from the momentum equation was compared with one determined from the 'law of the wall' for transpired boundary layers as well as the one for boundary layers along solid walls applying Jeromin's and Coles' transformations to the measured compressible boundary-layer profiles. The agreement is excellent. It can be said that the boundary-layer transformation in connection with the 'law of the wall' is the most reliable method for the time being to evaluate the skin-friction coefficient from a measured compressible boundary-layer profile.

Acknowledgements.

This paper was abstracted from a dissertation submitted to the University of Cambridge for the degree of Doctor of Philosophy.

The author wishes to express his gratitude to his supervisor, Dr. L. C. Squire, for his continued interest, assistance and encouragement during the whole course of the research. Many useful discussions with him have contributed to this work. Thanks are also due to Mr. N. B. Surrey and Mr. A. A. Barker and their staffs for their help and advice in the design and manufacture of the experimental equipment.

I should like to express my particular thanks to the Provost and Fellows of King's College, for their award of an external studentship and for their support throughout the three academic years of the research.

†There is a slight inconsistency for the case of zero injection for $M_\infty = 2{\cdot}5$ between the skin-friction coefficient evaluated from the 'law of the wall' and the one determined from Ludwieg/Tillmann's law, both laws used in conjunction with Coles' transformation. The 'law of the wall' predicts higher skin-friction coefficients (in the order of 10 per cent) than the momentum equation and Ludwieg/Tillmann's law. The reason for this discrepancy might be the sublayer hypothesis since slight changes of the transformation parameter σ have a significant influence on the skin-friction coefficient determined from 'law of the wall' whereas c_f determined from Ludwieg/Tillmann's law is affected only very little. The reason for this discrepancy for the zero injection case has not been investigated in more detail since the present analysis was mainly concentrating on transpired boundary layers where, fortunately, the concept of the sublayer hypothesis need not be used, Ref. 2.

LIST OF SYMBOLS

C	Constant in law of the wall
c_f	Local skin-friction coefficient
$F = \rho_w v_w / \rho_\infty u_\infty$	Injection parameter
H	Boundary-layer shape parameter
M	Mach number
P	Pressure term in momentum equation
p	Static pressure
$R = \frac{u_\infty \rho_\infty}{\mu_\infty}$	Reynolds number per unit length
$R_x = u_\infty \rho_\infty x/\mu_\infty$	Reynolds number based on x
$R_\theta = u_\infty \rho_\infty \theta/\mu_\infty$	Reynolds number based on θ
r	Recovery factor
T	Absolute temperature
u	Velocity in x-direction
u_τ	Skin-friction velocity
v	Velocity, normal to the wall (y-direction)
x	Co-ordinate along the plate
y	Co-ordinate normal to the wall
Y_T	Transformed co-ordinate
δ	Boundary-layer thickness
δ^*	Displacement thickness
θ	Momentum thickness
κ	Mixing-length constant
μ	Viscosity
ρ	Density

Subscripts.

o	Zero injection and stagnation conditions
r	Recovery condition
s	Sublimation condition and standard condition
w	Wall condition
∞	Free stream condition

Superscript.

$*$	Transformed flow (incompressible)

REFERENCES

No.	*Author(s)*	*Title, etc.*
1	D. Coles	The turbulent boundary layer in a compressible fluid. *Phys. Fluids* Vol. 7, pp. 1403–1423, 1964.
2	L. O. F. Jeromin	A boundary layer transformation for turbulent boundary layers with air injection. *J. Fluid Mech.* Vol. 31, pp. 65–94, 1968.
3	L. O. F. Jeromin	The status of research in transpired turbulent boundary layers. To be published in *Progress of Aeronautical Sciences*, Vol. 10, 1968. Pergamon Press.
4	L. O. F. Jeromin	Compressible turbulent boundary layer with fluid injection. Ph.D. Thesis, University of Cambridge, 1966.
5	D. L. Goldstein and R. Scherrer	Design and calibration of a total temperature probe for use at supersonic speeds. NACA TN 1885, May 1949.
6	R. A. Langworthy	The design and calibration of the total temperature probe for use in a Mach number 5 turbulent boundary with heat transfer. Defense Research Lab., University of Texas, Austin DRL–483, 1962.
7	J. E. Danberg	The equilibrium temperature probe, a device for measuring temperatures in hypersonic boundary layers. U.S. Naval Ordnance Lab., White Oak, Md., NOLTR 61–2 Aeroballistic Research Rep. No. 146, 1961.
8	E. M. Winkler	Stagnation temperature probes for use at high supersonic speeds and elevated temperatures. NAVORD Rept. 3834, October 1954.
9	W. S. Bradfield, A. R. Hanson and J. J. Sheppard, Jr.	Design, calibration, and application of a miniature total temperature probe. *J. Heat Transfer*, Vol. 86, p. 462–464, 1962.
10	J. E. Green	The turbulent boundary layer in two-dimensional flow with an oblique shock wave. Ph.D. Thesis, University of Cambridge, March 1966.
11	L. Rosehead, *et al*	*A Selection of Tables for use in Calculations of Compressible Air Flow.* Oxford, Clarendon Press, 1952.
12	D. A. Spence	Velocity and enthalpy distributions in the compressible turbulent boundary layer on a flat plate. *J. Fluid Mech.* Vol. 8, pp. 368–387, 1960.
13	L. Crocco	Su di unvalor massimo del coefficiente di transmissione del calore da una lamina piana a un fluido scorrente. *Rendiconti R. Accadmia dei Lincei*, Vol. 14, p. 790, 1931.
14	E. R. Van Driest	Turbulent boundary layer in compressible fluids. *J. Aero. Sci.* Vol. 18, pp. 145–160 and 216, 1951.

15 J. E. Danberg . . . . . Measurements of the characteristics of the compressible turbulent boundary layer with air injection.
NAVORD Rept. 6683, Aerodyn. Res. Rept. No. 67, 1960.
Characteristics of the turbulent boundary layer with heat and mass transfer at $M = 6{\cdot}7$.
NOL TR pp. 64–99, (Aerodyn. Res. Rept. No. 228), October 1964.

16 E. R. Bartle and B. M. Leadon . . . . Experimental evaluation of heat transfer with transpiration cooling in a turbulent boundary layer at $M = 3{\cdot}2$.
J. Aero/Space Sci. Vol. 27, pp. 78–80, 1960.

17 M. W. Rubesin, R. C. Maydew and S. A. Varga . . An analytical and experimental investigation of the skin friction of the turbulent boundary layer on a flat plate at supersonic speeds.
NACA TN 2305, 1951.

18 T. N. Stevenson . . . . A law of the wall for turbulent boundary layers with suction or injection.
The College of Aeronautics, Cranfield, Rept. Aero. No. 166, July 1963; Aero. Res. Coun. 26025 (unpublished).

19 H. Ludwieg and W. Tillmann . . Investigations of the wall shearing stress in turbulent boundary layers.
NACA TM 1285, May 1950.

20 F. Schultz-Grunow . . . . Neues Widerstrandsgesetz für glatte Platten.
Luftfahrtforschung Vol. 17, p. 239, 1940; translated as NACA TM 986, 1941.

21 S. C. Sommer and B. J. Short . . Free flight measurements of skin friction of turbulent boundary layers with high rates of heat transfer at high supersonic speeds.
J. Aeronautical Sci. Vol. 23, pp. 536–542, 1956.

22 C. J. Scott, G. E. Anderson and D. R. Elgin . . Laminar, transitional and turbulent mass transfer cooling experiments at Mach numbers 3 – 5.
University of Minnesota, Res. Rept. No. 162, AFOSR TN 59–1305, 1959.

23 L. Rosenhead, *et al* . . . . *A Selection of Graphs for use in Calculations of Compressible Air Flow.*
Oxford, Clarendon Press, 1954.

24 T. J. Black and A. J. Sarnecki . . The turbulent boundary layer with suction or injection.
A.R.C. R. & M. 3387, October 1958.

25 A. Mager . . . . . Transformation of the compressible turbulent boundary layer.
J. Aeronautical Sci. Vol. 25, pp. 305–311, 1958.

26 F. W. Matting, D. R. Chapman, J. R. Nyholm and A. G. Thomas . . Turbulent skin friction at high Mach numbers and Reynolds numbers in air and helium.
NASA TR R–82, 1961.

27 W. H. Shuttz, W. H. Hartwig and J. E. Weiler . . Turbulent boundary layer and skin friction measurements on a smooth, thermally insulated flat plate at supersonic speeds.
Univ. Texas Defense Research Lab., Austin, Texas, DRL–364, CM–823, 1955.

28 R. A. Dutton .. .. .. The velocity distribution of a turbulent boundary layer along a flat plate.
A.R.C. C.P. 453, 1957.

29 H. S. Mickley and R. S. Davies .. .. Momentum transfer for flow over a flat plate with blowing.
NACA TN 4017, March 1957.

30 P. N. Romanenko and V. N. Kharchenko .. The effect of transverse mass flow on heat transfer and friction drag in a turbulent flow of compressible gas along an arbitrarily shaped surface.
Int. J. Heat and Mass Transfer, Vol. 6, pp. 727–738, 1963.

31 J. McQuaid .. .. .. Incompressible turbulent boundary layers with distributed injection.
Ph.D. Thesis, University of Cambridge, 1966.

32 M. W. Rubesin .. .. The influence of surface injection on heat transfer and skin friction associated with the high speed turbulent boundary layer.
NACA RM A55L13, 1956.

33 C. C. Pappas and A. F. Okuno Measurements of skin friction of the compressible turbulent boundary layer on a cone with foreign gas injection.
J. Aeronautical Sci. Vol. 27, p. 321, 1960.

34 T. Tendeland and A. F. Okuno The effect of fluid injection on the compressible turbulent boundary layer–the effect on skin friction of air injected into the boundary layer of a cone at $M = 2{\cdot}7$.
NACA RM A65D05, 1956.

35 W. H. Dorrance and F. J. Dore The effect of mass transfer on the compressible turbulent boundary layer skin friction and heat transfer.
J. Aeronautical Sci. Vol. 21, pp. 404–410, 1954.

36 M. W. Rubesin .. .. An analytical estimation of the effect of transpiration cooling on the heat transfer and skin friction characteristics of a compressible, turbulent boundary layer.
NACA TN 3341, 1954.

37 D. B. Spalding, D. M. Auslander and T. R. Sundaram .. .. The calculation of heat and mass transfer through the turbulent boundary layer on a flat plate at high Mach numbers, with and without chemical reaction.
Supersonic Flow, Chemical Processes and Radiative Transfer, edited D. B. Olfe and V. Sakkay, Pergamon Press, pp. 211–276, 1964.

38 J. E. Green .. .. .. Private communication.
Engineering Laboratory, University of Cambridge, 1964.

APPENDIX A

The Contents of the Tables.

Every table is labelled with a Roman and an Arabic number. The Roman number is introduced to distinguish between boundary-layer developments measured at different Mach numbers, injection mass flows and wall temperatures.

There are fifteen different sets of boundary-layer developments:

Table II	: $F = 0, M_\infty = 2{\cdot}5, T_w > T_r$,	solid plate
Table III	: $F = 0{\cdot}57 \times 10^{-3}, M_\infty = 2{\cdot}5, T_w > T_r$,	plate C
Table IV	: $F = 0{\cdot}895 \times 10^{-3}, M_\infty = 2{\cdot}5, T_w > T_r$,	plate C
Table V	: $F = 1{\cdot}271 \times 10^{-3}, M_\infty = 2{\cdot}5, T_w > T_r$,	plate A
Table VI	: $F = 0, M_\infty = 3{\cdot}5, T_w > T_r$,	solid plate
Table VII	: $F = 0{\cdot}653 \times 10^{-3}, M_\infty = 3{\cdot}5, T_w > T_r$,	plate C
Table VIII	: $F = 1{\cdot}172 \times 10^{-3}, M_\infty = 3{\cdot}5, T_w > T_r$,	plate C
Table IX	: $F = 2{\cdot}111 \times 10^{-3}, M_\infty = 3{\cdot}5, T_w > T_r$,	plate C
Table X	: $0{\cdot}4 < F \times 10^3 < 1{\cdot}3, M_\infty = 2{\cdot}5, T_w \simeq T_r$,	plate A
Table XI	: $1{\cdot}2 < F \times 10^3 < 2{\cdot}2, M_\infty = 3{\cdot}5, T_w \simeq T_r$,	plate C
Table XII	: $0{\cdot}4 < F \times 10^3 < 1{\cdot}3, M_\infty = 2{\cdot}5, T_w < T_r$,	plate A and plate C
Table XIII	: $1{\cdot}2 < F \times 10^3 < 2{\cdot}3, M_\infty = 3{\cdot}5, T_w < T_r$,	plate C
Table XIV	: $F = 0{\cdot}636 \times 10^{-3}, M_\infty = 3{\cdot}5, T_w > T_r$,	plate D (rough surface)
Table XV	: $F = 2{\cdot}060 \times 10^{-3}, M_\infty = 3{\cdot}5, T_w > T_r$,	plate D (rough surface)
Table XVI	: $F = 1{\cdot}340 \times 10^{-3}, M_\infty = 2{\cdot}5, T_w > T_r$,	plate C

For each set of tables there is a summary of all the interesting boundary-layer parameters; this summary is labelled with a Roman numeral followed by a zero (for example Table II–0), and the boundary-layer profiles themselves are labelled by the same Roman numeral plus an Arabic one (for example II–8), to distinguish between the various boundary-layer profiles measured at different positions along the plate: thus, for example, the boundary-layer parameters of the profiles II–1 to II–10 are summarised in Table II–0.

The following quantities describing the boundary layer are summarised in the tables 'zero' at the end of this Report:

column 1 : the serial number of the run consisting of three numbers: the first gives the Mach number (for example 2·5) the second the approximate mass flow parameter $F \times 10^3$ (for example 0·8) the third the running number of the experiment (for example 1) (to distinguish between runs measured at the same station for the same Mach number and injection mass flow but at different wall temperatures) followed by a number defining the measuring station along the plate (for example 50); hence a run would be defined completely for example by 2·5 – 0·8 – 1·50. The boundary-layer profiles measured along plate D (rough surface) are marked '*R*';

column 2 : plate used for the experiment (*see* Section 2.1.1);

column 3 : distance X' (*m*) along the plate where the measurement was carried out (this distance was measured from the critical dimension of the nozzle);

column 4 : stangation pressure p_o (at);

column 5 : injection mass flow $\rho_w v_w$ [kg/m^2.s];

column 6 : free stream stagnation temperature $T_{o\infty}$ (°K);

column 7 : wall temperature T_w (°K);

column 8 : recovery temperature T_r (°K)
(the recovery temperature was evaluated using a recovery factor of $r = 0{\cdot}890$ for the zero injection case; with injection the information according to Ref. 16 has been accepted (*see* Figure 14));

column 9 : free stream temperature T_∞ (°K);

column 10 : ratio of wall temperature to free stream temperature;

column 11 : free stream static pressure p_∞ (at);

column 12 : free stream Mach number M_∞;

column 13 : free stream velocity u_∞ (*m/s*);

column 14 : Reynolds number R (1/*m*);

column 15 : Reynolds number R_x' based on distance from the critical dimension of the nozzle;

column 16 : virtual origin Δx_v (*m*) of the flow measured from the critical dimension of the nozzle (a negative value means that the virtual origin is situated upstream; a positive one means a shift downstream);

column 17 : Reynolds number R_x based on distance from the virtual origin of the turbulent flow (a mean value for R has been used)

column 18 : free stream mass flow $\rho_\infty u_\infty$ [kg/m^2.s];

column 19 : injection mass flow parameter $F = \rho_w v_w/\rho_\infty u_\infty$ (based on a mean value for $\rho_\infty u_\infty$);

column 20 : momentum thickness θ (mm);

column 21 : displacement thickness δ^* (mm);

column 22 : boundary-layer thickness δ (mm) for $u/u_\infty = 0{\cdot}995$;

column 23 : $Y_T = \int_o^\delta \rho/\rho_w \, dy$ (mm) which will be used for boundary-layer transformation, to transform, for example, the displacement thickness;

column 24 : boundary-layer shape parameter H;

column 25 : Reynolds number R_θ based on momentum thickness θ (a mean value for R has been used);

column 26 : skin-friction coefficient c_{f1} evaluated from the momentum thickness development $\theta = f(x)$ and the momentum equation (typical examples for both Mach numbers are presented on Figures 18 and 19).†

---

†At $M_\infty = 3{\cdot}5$ the value for c_{f1} is corrected for three-dimensional effects whereas the value in brackets is not corrected.

column 27 : (i) with injection
skin-friction coefficient c_{f2} evaluated from Stevenson's law[18] for incompressible flow

$$\frac{2u_\tau^*}{v_w^*}\left[\sqrt{1+\frac{v_w^* u^*}{u_\tau^{*2}}}-1\right] = \frac{1}{\kappa} ln \frac{\rho^* y^* u_\tau^*}{\mu^*} + C$$

(with Coles' constants $\kappa = 0{\cdot}410$ and $C = 5{\cdot}00$) and Jeromin's transformation[2,4];

(ii) without injection
skin-friction coefficient c_{f2} evaluated from the 'law of the wall' for incompressible flow

$$\frac{u^*}{u_\tau^*} = \frac{1}{\kappa} ln \frac{\rho^* y^* u_\tau^*}{\mu^*} + C$$

($\kappa = 0{\cdot}410$ and $C = 5{\cdot}00$) and Coles' transformation[1] (superscript* refers to incompressible flow)

column 28 : (i) with injection
skin-friction coefficient c_{f3} evaluated from an empirical relationship for the skin-friction coefficient for transpired incompressible boundary layers (*see* Jeromin[4]) with the help of Jeromin's transformation. The empirical relationship defining c_f^* is of the form

$$\frac{c_f^*}{c_{fo}} = 1+\alpha\left(\frac{2F^*}{c_{fo}^*}\right)+\beta\left(\frac{2F^*}{c_{fo}^*}\right)^2+\gamma\left(\frac{2F^*}{c_{fo}^*}\right)^3+\delta\left(\frac{2F^*}{c_{fo}^*}\right)^4 \qquad \text{(A.1)}$$

where c_{fo}^* is the skin-friction coefficient without injection and α, β, γ, δ are constants evaluated from experimental data. The skin-friction coefficients c_f^* and c_{fo}^* are compared with each other in the empirical relationship at $R_x^* = \text{const}$. The skin-friction coefficient without injection was determined from Ludwieg/Tillmann's[19] formula
$c_{f0}^* = 0{\cdot}246 \times 10^{-0{\cdot}678H^*} R_{\theta 0}^{*\,-0{\cdot}268}$

(ii) with injection
skin-friction coefficient c_{f3} evaluated from Ludwieg/Tillmann's law for incompressible flow and Coles' transformation[1].

The tables for the boundary-layer profiles (not included in this paper)

column 1 : distance y (mm) normal to the plate

column 2 : ratio of distance y (mm) over momentum thickness θ (mm)

column 3 : local Mach number M

column 4 : ratio of local velocity u (m/s) over free stream velocity u_∞ (m/s)

column 5 : ratio of local temperature T°K over free stream temperature T_∞°K

column 6 : $Y_T = \int_o^y \rho/\rho_w \, dy$ (mm) which in this, or a similar form, form part of all the transformations for the y-co-ordinate

column 7 : (i) with injection

y-co-ordinate $\left(\frac{2u_\tau^*}{v_w^*}\left(\sqrt{1+\frac{v_w^* u^*}{u_\tau^{*2}}}-1\right)\right)$ for Stevenson's law[18] applying Jeromin's transformation[2] to the compressible turbulent boundary-layer profile

(ii) without injection

y-co-ordinate u^*/u_τ^* for the 'law of the wall'[1] applying Coles' transformation[1] to the compressible boundary- layer profile

column 8 : (i) with injection

x-co-ordinate $ln\frac{y^* u_\tau^*}{v^*}$ for Stevenson's law[18] applying Jeromin's transformation[2] to the compressible boundary-layer profile

(ii) without injection

x-co-ordinate $ln\frac{y^* u_\tau^*}{v^*}$ for the 'law of the wall'[1] applying Coles' transformation[1] to the compressible boundary-layer profile

TABLE 1

$T_w > T_r$

M	$F \times 10^3$	$c_{f1}.10^3$	$\Delta c_{f1}.10^3$	$c_{f2}.10^3$	$c_{f3}.10^3$
2·55	0	1·60	±0·10	1·87	1·62
2·53	0·57	1·12	±0·12	1·08	1·18
2·53	0·895	0·95	±0·15	0·95	0·95
2·54	1·27	0·725	±0·20	0·72	0·73
3·58	0	1·18	±0·10	1·27	1·27
3·56	0·65	0·79	±0·12	0·71	0·77
3·55	1·17	0·56	±0·15	0·47	0·56
3·52	2·11	0·37	±0·20	0·23	0·35

TABLE II-0

RUN	PLATE	x' [m]	P_o [at]	$\rho_w v_w$ [kg/m²·s]	T_o [°K]	T_w [°K]	T_r [°K]	T_∞ [°K]	T_w/T_∞ [-]
2.5-0.0-1.10		0.334	5.208	0	295	285.5	276	127.9	2.334
2.5-0.0-1.20		0.3465	5.208	0	292	284.5	273	127.5	2.334
2.5-0.0-1.30	solid	0.3595	5.208	0	293	283.5	274	127.5	2.225
2.5-0.0-1.40		0.372	5.209	0	296.5	284.5	277.5	129	2.207
2.5-0.0-1.50		0.3845	5.209	0	294	286	275	127.5	2.244
2.5-0.0-1.60		0.3975	5.210	0	294.5	284	275.5	127.5	2.227
2.5-0.0-1.70		0.4103	5.210	0	295	284	276	127.5	2.226
2.5-0.0-1.80	solid	0.422	5.210	0	296	284.5	277	128	2.223
2.5-0.0-1.90		0.435	5.210	0	292.5	285	273.5	126	2.265
2.5-0.0-1.100		0.4485	5.210	0	294	285.5	275	127	2.244

RUN	P_∞ [at]	M_∞ [-]	U_∞ [m/s]	$R \cdot 10^{-7}$ [1/m]	$R'_x 10^{-7}$ [-]	Δx_v [m]	$R_x 10^{-7}$ [-]	$\rho_\infty U_\infty$ [kg/m²s]	$F \cdot 10^3$ [-]
2.5-0.0-1.10	0.2792	2.557	579.8	4.933	1.646		1.953	432.2	0
2.5-0.0-1.20	0.2861	2.541	575.1	5.053	1.751		2.015	441.1	0
2.5-0.0-1.30	0.2823	2.550	577.1	5.003	1.797	-0.06	2.078	436.7	0
2.5-0.0-1.40	0.2815	2.551	580.7	4.912	1.827		2.14	433.4	0
2.5-0.0-1.50	0.2808	2.553	578.1	4.978	1.914		2.203	434.9	0
2.5-0.0-1.60	0.2794	2.556	579.0	4.955	1.968		2.268	433.1	0
2.5-0.0-1.70	0.2779	2.560	579.9	4.931	2.024		2.333	431.2	0
2.5-0.0-1.80	0.2764	2.563	581.5	4.893	2.066	-0.06	2.387	428.9	0
2.5-0.0-1.90	0.2719	2.574	578.9	4.956	2.158		2.455	427.3	0
2.5-0.0-1.100	0.2749	2.567	579.4	4.944	2.218		2.519	429.3	0

RUN	Θ [mm]	δ^* [mm]	δ [mm]	$\int_0^\delta \rho/\rho_w dy$ [mm]	H [-]	R_Θ [-]	$c_{f_1} 10^3$ [-]	$c_{f_2} 10^3$ [-]	$c_{f_3} 10^3$ [-]
2.5-0.0-1.10	0.315	1.327	4.153	7.32	4.21	15630		1.80	1.63
2.5-0.0-1.20	0.326	1.363	4.275	7.495	4.18	16170		1.80	1.625
2.5-0.0-1.30	0.3355	1.401	4.380	7.685	4.175	16640		1.80	1.62
2.5-0.0-1.40	0.347	1.435	4.475	7.755	4.143	17200		1.85	1.62
2.5-0.0-1.50	0.3515	1.467	4.570	8.015	4.17	17430	1.60	1.87	1.615
2.5-0.0-1.60	0.366	1.520	4.697	8.150	4.155	18150		1.87	1.61
2.5-0.0-1.70	0.3765	1.558	4.963	8.70	4.14	18670		1.90	1.605
2.5-0.0-1.80	0.3745	1.543	4.970	8.71	4.12	18570		1.92	1.60
2.5-0.0-1.90	0.389	1.632	5.085	8.995	4.095	19280		1.91	1.60
2.5-0.0.1.100	0.397	1.652	5.205	9.22	4.08	19580		1.90	1.595

TABLE III-0

RUN	PLATE	x' [m]	P_o [at]	$\varrho_w v_w$ [kg/m²·s]	T_o [°K]	T_w [°K]	T_r [°K]	T_∞ [°K]	T_w/T_∞ [-]
2.5-0.5-1.10		0.341	5.217	0.2525	291	281	271	127	2.213
2.5-0.5 1.20		0.354	5.192	0.2516	291	280	271	128	2.195
2.5-0.5-1.30	C	0.3665	5.190	0.2535	293.5	285.5	273	128	2.22
2.5-0.5-1.40		0.3793	5.190	0.2529	293.5	281	273	129	2.185
2.5-0.5-1.50		0.3915	5.189	0.2534	293.5	279.5	273	129	2.17
2.5-0.5-1.60		0.404	5.179	0.2520	293	282	272.5	127.5	2.21
2.5-0.5-1.70		0.4165	5.178	0.2528	293.5	282	273	126.5	2.225
2.5-0.5-1.80	C	0.429	5.186	0.2515	294.5	278	274	127.5	2.185
2.5-0.5-1.90		0.442	5.199	0.2533	291.5	279	271	126	2.215
2.5-0.5-1.100		0.455	5.200	0.2525	292	280	272	127	2.205

RUN	P_∞ [at]	M_∞ [-]	U_∞ [m/s]	$R \cdot 10^{-7}$ [1/m]	$R'_x \cdot 10^{-7}$ [-]	Δx_v [m]	$R_x \cdot 10^{-7}$ [-]	$\varrho_\infty U_\infty$ [kg/m²·s]	$F \cdot 10^3$ [-]
2.5-0.5-1.10	0.2873	2.539	574.0	5.088	1.736		1.808	443.1	0.570
2.5-0.5-1.20	0.2923	2.525	572.3	5.108	1.810		1.873	447.2	0.563
2.5-0.5-1.30	0.2867	2.537	576.0	5.011	1.837	-0.02	1.937	440.0	0.575
2.5-0.5-1.40	0.2911	2.527	575.0	5.035	1.908		2.000	444.0	0.570
2.5-0.5-1.50	0.2915	2.527	574.9	5.036	1.970		2.063	444.4	0.571
2.5-0.5-1.60	0.2826	2.545	576.5	4.988	2.017		2.125	436.1	0.577
2.5-0.5-1.70	0.2738	2.565	578.8	4.928	2.055		2.187	427.5	0.592
2.5-0.5-1.80	0.2752	2.653	579.8	4.910	2.108	-0.02	2.248	428.2	0.587
2.5-0.5-1.90	0.2773	2.558	576.3	5.001	2.208		2.315	432.5	0.585
2.5-0.5-1.100	0.2820	2.548	575.9	5.014	2.282		2.380	436.5	0.579

RUN	Θ [mm]	δ^* [mm]	δ [mm]	$\int_0^\delta \varrho/\varrho_w \, dy$ [mm]	H [-]	R_Θ [-]	$c_{f_1} \cdot 10^3$ [-]	$c_{f_2} \cdot 10^3$ [-]	$c_{f_3} \cdot 10^3$ [-]
2.5-0.5-1.10	0.449	1.923	5.14	8.15	4.305	23830		1.00	1.21
2.5-0.5-1.20	0.477	2.028	5.46	9.04	4.25	23880		1.01	1.20
2.5-0.5-1.30	0.4765	2.047	5.447	9.065	4.293	23850		1.05	1.20
2.5-0.5-1.40	0.500	2.107	5.613	9.195	4.215	25050		1.07	1.18
2.5-0.5-1.50	0.516	2.165	5.89	9.67	4.195	25850	1.1	1.08	1.175
2.5-0.5-1.60	0.528	2.215	6.15	10.30	4.195	26450		1.15	1.17
2.5-0.5-1.70	0.537	2.264	6.37	10.72	4.21	26880		1.22	1.16
2.5-0.5-1.80	0.5715	2.405	6.64	11.00	4.20	28630		1.15	1.15
2.5-0.5-1.90	0.580	2.450	6.86	11.54	4.223	29070		1.13	1.14
2.5-0.5-1.100	0.600	2.535	7.03	11.73	4.223	30050		1.11	1.13

TABLE IV-0

RUN	PLATE	X' [m]	P_o [at]	$\rho_w V_w$ [kg/m²·s]	T_o [°K]	T_w [°K]	T_r [°K]	T_∞ [°K]	T_w/T_∞ [-]
2.5-0.9-1.10		0.341	5.218	0.4005	292	281.5	271.5	127.5	2.205
2.5-0.9-1.20		0.354	5.192	0.3945	292.5	281.5	272	128	2.195
2.5-0.9-1.30	C	0.3665	5.190	0.3930	294.5	282.5	274	128.5	2.195
2.5-0.9-1.40		0.3793	5.189	0.3945	292.5	281	272	128.5	2.195
2.5-0.9-1.50		0.3915	5.181	0.3940	292.5	281	272	128	2.195
2.5-0.9-1.60		0.404	5.179	0.3945	293.5	282.5	272.5	127.5	2.215
2.5-0.9-1.70		0.4165	5.179	0.3940	294.5	282	274	128.5	2.20
2.5-0.9-1.80	C	0.429	5.188	0.3945	291	281	270.5	126	2.23
2.5-0.9-1.90		0.442	5.189	0.3935	292.5	280.5	272	127	2.205
2.5-0.9-1.100		0.455	5.190	0.3945	294	281.5	273	128	2.20

RUN	P_∞ [at]	M_∞ [-]	U_∞ [m/s]	$R \cdot 10^{-7}$ [1/m]	$R'_x \cdot 10^{-7}$ [-]	ΔX_v [m]	$R_x \cdot 10^{-7}$ [-]	$\rho_\infty U_\infty$ [kg/m²·s]	$F \cdot 10^3$ [-]
2.5-0.9-1.10	0.2881	2.537	574.9	5.066	1.729		1.670	443.1	0.903
2.5-0.9-1.20	0.2892	2.532	574.6	5.049	1.789		1.773	443.1	0.890
2.5-0.9-1.30	0.2851	2.541	577.7	4.969	1.820	0	1.835	437.5	0.899
2.5-0.9-1.40	0.2894	2.531	574.8	5.040	1.862		1.898	442.9	0.892
2.5-0.9-1.50	0.2881	2.533	575.0	5.027	1.968		1.960	442.4	0.891
2.5-0.9-1.60	0.2809	2.549	577.2	4.970	2.007		2.023	434.2	0.910
2.5-0.9-1.70	0.2824	2.545	578.1	4.946	2.060		2.085	434.7	0.909
2.5-0.9-1.80	0.2764	2.560	576.1	5.005	2.145	0	2.147	431.9	0.915
2.5-0.9-1.90	0.2811	2.550	576.4	5.000	2.210		2.213	435.4	0.905
2.5-0.9-1.100	0.2844	2.542	577.0	4.985	2.270		2.278	437.5	0.903

RUN	Θ [mm]	δ^* [mm]	δ [mm]	$\int_0^\delta \rho/\rho_w \, dy$ [mm]	H [-]	R_Θ [-]	$c_{f_1} 10^3$ [-]	$c_{f_2} 10^3$ [-]	$c_{f_3} 10^3$ [-]
2.5-0.9-1.10	0.490	2.135	5.455	8.93	4.36	24530		0.85	0.99
2.5-0.9-1.20	0.513	2.217	5.765	9.45	4.32	25670		0.89	0.98
2.5-0.9-1.30	0.528	2.283	5.85	9.55	4.32	26400		0.905	0.965
2.5-0.9-1.40	0.543	2.323	5.98	9.71	4.28	27180		0.94	0.955
2.5-0.9-1.50	0.564	2.407	6.235	10.18	4.27	28200	0.9	0.93	0.945
2.5-0.9-1.60	0.581	2.483	6.628	11.03	4.275	29070		0.99	0.935
2.5-0.9-1.70	0.590	2.510	7.48	12.55	4.245	29550		0.97	0.925
2.5-0.9-1.80	0.622	2.653	7.21	12.08	4.27	31130		0.98	0.915
2.5-0.9-1.90	0.648	2.76	7.45	12.40	4.26	32430		0.98	0.905
2.5-0.9-1.100	0.670	2.858	7.548	12.40	4.265	33530		0.93	0.89

TABLE V-O

RUN	PLATE	X' [m]	P_o [at]	$\rho_w V_w$ [kg/m²·s]	T_o [°K]	T_w [°K]	T_r [°K]	T_∞ [°K]	T_w/T_∞ [-]
2.5-1.2-1.10		0.335	5.216	0.5510	299	288	270	131.7	2.19
2.5-1.2-1.20		0.3475	5.216	0.5500	298.5	287	271	130.5	2.205
2.5-1.2-1.30	A	0.360	5.216	0.5505	298.5	287.5	271	130.5	2.205
2.5-1.2-1.40		0.373	5.204	0.5545	295	292.5	270	128.5	2.275
2.5-1.2-1.50		0.3855	5.204	0.5545	295	291.5	272	128.5	2.265
2.5-1.2-1.60		0.398	5.203	0.5515	296.5	290.5	272	129	2.255
2.5-1.2-1.70		0.4105	5.204	0.552	297	290.5	273	128	2.265
2.5-1.2-1.80	A	0.4235	5.204	0.551	297.5	290.5	271	128	2.27
2.5-1.2-1.90		0.436	5.204	0.5505	297.5	290	270	129	2.25
2.5-1.2-1.100		0.4495	5.204	0.551	297.5	290.5	270	129.5	2.24

RUN	P_∞ [at]	M_∞ [-]	U_∞ [m/s]	$R \cdot 10^{-7}$ [1/m]	$R'_x \cdot 10^{-7}$ [-]	Δx_v [m]	$R_x \cdot 10^{-7}$ [-]	$\rho_\infty U_\infty$ [kg/m²·s]	$F \cdot 10^3$ [-]
2.5-1.2-1.10	0.2967	2.518	579.5	4.946	1.656		1.570	445.9	1.270
2.5-1.2-1.20	0.2857	2.543	581.8	4.888	1.700		1.630	435.9	1.268
2.5-1.2-1.30	0.2887	2.536	581.1	4.907	1.769	+0.015	1.693	438.4	1.269
2.5-1.2-1.40	0.2841	2.545	578.6	4.957	1.850		1.757	436.7	1.277
2.5-1.2-1.50	0.2839	2.545	578.7	4.955	1.912		1.817	436.4	1.277
2.5-1.2-1.60	0.2814	2.551	580.6	4.907	1.954		1.878	433.1	1.271
2.5-1.2-1.70	0.2744	2.567	582.7	4.855	1.995		1.940	426.2	1.272
2.5-1.2-1.80	0.2722	2.572	583.4	4.837	2.050	+0.015	2.005	424.0	1.270
2.5-1.2-1.90	0.2791	2.556	582.1	4.870	2.124		2.067	430.2	1.269
2.5-1.2-1.100	0.2851	2.542	580.6	4.908	2.203		2.133	435.9	1.270

RUN	Θ [mm]	δ^* [mm]	δ [mm]	$\int_0^\delta \rho/\rho_w dy$ [mm]	H [-]	R_Θ [-]	$c_{f_1} \cdot 10^3$ [-]	$c_{f_2} \cdot 10^3$ [-]	$c_{f_3} \cdot 10^3$ [-]
2.5-1.2-1.10	0.547	2.390	5.935	9.54	4.37	27300		0.70	0.78
2.5-1-2-1.20	0.573	2.515	6.35	10.33	4.39	28130		0.71	0.77
2.5-1.2-1.30	0.584	2.563	6.515	10.59	4.385	28650		0.72	0.755
2.5-1.2-1.40	0.605	2.695	6.703	11.175	4.455	29650		0.73	0.74
2.5-1.2-1.50	0.622	2.758	6.905	11.45	4.44	30500	0.725	0.72	0.73
2.5-1.2-1.60	0.645	2.817	7.275	12.17	4.37	31630		0.77	0.725
2.5-1.2-1.70	0.675	2.940	7.725	13.06	4.355	33100		0.79	0.72
2.5-1.2-1.80	0.702	3.060	8.200	13.94	4.355	34400		0.78	0.71
2.5-1.2-1.90	0.723	3.145	8.220	13.77	4.345	35450		0.72	0.70
2.5-1.2-1.100	0.744	3.220	8.470	14.15	4.33	36470		0.70	0.69

TABLE VI-0

RUN	PLATE	X' [m]	P_o [at]	$\rho_w v_w$ [kg/m²·s]	T_o [°K]	T_w [°K]	T_r [°K]	T_∞ [°K]	T_w/T_∞ [-]
3.5-0.0-1.10		0.334	8.284	0	297	288	273	82.4	3.495
3.5-0.0-1.20		0.3468	8.284	0	296	287.5	272	82.4	3.491
3.5-0.0-1.30	solid	0.359	8.283	0	297	286.5	272.5	83.0	3.471
3.5-0.0-1.40		0.372	8.282	0	294.5	289.5	270	82.2	3.525
3.5-0.0-1.50		0.3845	8.282	0	294.5	286.5	270.5	82.8	3.460
3.5-0.0-1.60		0.397	8.282	0	295.5	286	271.5	83.1	3.443
3.5-0.0-1.70		0.410	8.281	0	296	285.5	271.5	83.3	3.427
3.5-0.0-1.80	solid	0.423	8.281	0	297	286	272.5	84.2	3.397
3.5-0.0-1.90		0.435	8.281	0	297.5	285.5	273	84.5	3.377
3.5-0.0-1.100		0.448	8.281	0	297.5	286.5	273	84.4	3.393

RUN	P_∞ [at]	M_∞ [-]	U_∞ [m/s]	$R \cdot 10^7$ [1/m]	$R_x' \cdot 10^{-7}$ [-]	ΔX_v [m]	$R_x \cdot 10^{-7}$ [-]	$\rho_\infty U_\infty$ [kg/m²·s]	$F \cdot 10^3$ [-]
3.5-0.0-1.10	0.0935	3.606	656.4	4.571	1.526		1.832	254.4	0
3.5-0.0-1.20	0.0942	3.601	655.5	4.597	1.594		1.892	255.9	0
3.5-0.0-1.30	0.0959	3.588	655.5	4.610	1.656	-0.06	1.948	258.6	0
3.5-0.0-1.40	0.0954	3.592	653	4.661	1.732		2.010	258.8	0
3.5-0.0-1.50	0.0972	3.578	652.7	4.685	1.802		2.065	261.9	0
3.5-0.0-1.60	0.0974	3.577	653.5	4.665	1.853		2.125	261.8	0
3.5-0.0-1.70	0.0980	3.572	653.7	4.668	1.913		2.185	262.8	0
3.5-0.0-1.80	0.1008	3.553	653.7	4.690	1.982	-0.06	2.245	267.2	0
3.5-0.0-1.90	0.1011	3.550	654.2	4.681	2.038		2.303	267.5	0
3.5-0.0-1.100	0.1007	3.553	654.4	4.675	2.096		2.363	266.8	0

RUN	Θ [mm]	δ^* [mm]	δ [mm]	$\int_0^\delta \rho/\rho_w \, dy$ [mm]	H [-]	R_Θ [-]	$c_{f_1} \cdot 10^3$ [-]	$c_{f_2} \cdot 10^3$ [-]	$c_{f_3} \cdot 10^3$ [-]
3.5-0.0-1.10	0.305	2.135	4.935	11.22	7.00	14180		1.33	1.30
3.5-0.0-1.20	0.3155	2.197	5.07	11.53	6.96	14770		1.32	1.29
3.5-0.0-1.30	0.329	2.275	5.175	11.58	6.92	15300		1.28	1.28
3.5-0.0-1.40	0.336	2.350	5.355	12.20	6.995	15630		1.27	1.27
3.5-0.0-1.50	0.344	2.370	5.435	12.24	6.89	16000	1.18 (1.38)	1.27	1.27
3.5-0.0-1.60	0.3505	2.406	5.505	12.29	6.86	16300		1.26	1.265
3.5-0.0-1.70	0.3585	2.445	5.67	12.70	6.82	16680		1.26	1.26
3.5-0.0-1.80	0.3695	2.500	5.75	12.72	6.76	17180		1.23	1.25
3.5-0.0-1.90	0.3745	2.545	5.995	12.90	6.76	17430		1.21	1.24
3.5-0.0-1.100	0.385	2.602	5.97	13.19	6.75	17910		1.21	1.23

TABLE VII-0

RUN	PLATE	x' [m]	P_o [at]	$\rho_w V_w$ [kg/m²·s]	T_o [°K]	T_w [°K]	T_r [°K]	T_∞ [°K]	T_w/T_∞ [-]
3.5-0.6-1.10		0.3405	8.289	0.1734	298.5	292	270	83.5	3.495
3.5-0.6-1.20		0.3535	8.289	0.1739	296.5	288	268	83.5	3.45
3.5-0.6-1.30	C	0.3653	8.289	0.1770	297	289.5	269	83.8	3.455
3.5-0.6-1.40		0.3785	8.289	0.1757	297.5	288.5	269	84.0	3.433
3.5-0.6-1.50		0.391	8.305	0.1747	293.5	288	265.5	83.2	3.463
3.5-0.6-1.60		0.404	8.319	0.1747	293	288	265	83.0	3.47
3.5-0.6-1.70		0.4165	8.315	0.1752	295.5	285.5	267.5	84.3	3.39
3.5-0.6-1.80	C	0.429	8.301	0.1752	291.5	291	264	83.3	3.49
3.5-0.6-1.90		0.442	8.301	0.1779	295	290.5	266.5	84.2	3.45
3.5-0.6-1.100		0.450	8.297	0.1728	294.5	289.5	267	84.2	3.44

RUN	P_∞ [at]	M_∞ [-]	U_∞ [m/s]	$R \cdot 10^{-7}$ [1/m]	$R'_x \cdot 10^{-7}$ [-]	ΔX_v [m]	$R_x \cdot 10^{-7}$ [-]	$\rho_\infty U_\infty$ [kg/m²·s]	$F \cdot 10^3$ [-]
3.5-0.6-1.10	0.0964	3.585	657.1	4 582	1.560		1.611	258.9	0.6475
3.5-0.6-1.20	0.0983	3.571	654.3	4.660	1.646		1.673	263.0	0.6485
3.5-0.6-1.30	0.0988	3.568	654.8	4.653	1.701	0	1.728	263.6	0.661
3.5-0.6-1.40	0.0994	3.563	654.8	4.659	1.762		1.792	264.7	0.6555
3.5-0.6-1.50	0.1008	3.555	649.9	4.787	1.873		1.850	269.0	0.652
3.5-0.6-1.60	0.1002	3.559	649.9	4.783	1.932		1.912	268.1	0.652
3.5-0.6-1.70	0.1032	3.537	651.2	4.777	1.990		1.973	272.4	0.654
3.5-0.6-1.80	0.1031	3.538	647.3	4.868	2.090	0	2.030	273.9	0.654
3.5-0.6-1.90	0.1037	3.534	650.1	4.806	2.124		2.093	273.6	0.664
3.5-0.6-1.100	0.1028	3.539	651.0	4.772	2.146		2.130	272.7	0.645

RUN	Θ [mm]	δ^* [mm]	δ [mm]	$\int_0^\delta \rho/\rho_w \, dy$ [mm]	H [-]	R_Θ [-]	$c_{f_1} \cdot 10^3$ [-]	$c_{f_2} \cdot 10^3$ [-]	$c_{f_3} \cdot 10^3$ [-]
3.5-0.0-1.10	0.4035	2.925	5.965	12.70	7.25	19100		0.75	0.80
3.5-0.6-1.20	0.4285	3.060	6.286	13.26	7.14	20270		0.74	0.795
3.5-0.6-1.30	0.4455	3.200	6.475	13.57	7.18	21130		0.72	0.785
3.5-0.6-1.40	0.454	3.240	6.58	13.76	7.13	21500		0.72	0.78
3.5-0.6-1.50	0.466	3.354	6.70	13.94	7.19	22070	0.79 (0.99)	0.69	0.77
3.5-0.6-1.60	0.477	3.435	6.90	14.44	7.19	22600		0.71	0.765
3.5-0.6-1.70	0.5045	3.534	7.155	14.75	7.01	23870		0.70	0.76
3.5-0.6-1.80	0.5075	3.580	7.38	15.62	7.17	24030		0.70	0.75
3.5-0.6-1.90	0.5215	3.668	7.51	15.82	7.03	24730		0.72	0.75
3.5-0.6-1.100	0.538	3.813	7.85	16.55	7.08	25500		0.70	0.745

TABLE VIII-0

RUN	PLATE	X' [m]	P_o [at]	$\rho_w V_w$ [kg/m²·s]	T_o [°K]	T_w [°K]	T_r [°K]	T_∞ [°K]	T_w/T_∞ [-]
3.5-1.2-1.10		0.343	8.289	0.3160	296	290.5	266.5	83.3	3.49
3.5-1.2-1.20		0.358	8.289	0.3157	296.5	292	267	83.8	3.48
3.5-1.2-1.30	C	0.368	8.289	0.3174	297.5	290	268	84.4	3.42
3.5-1.2-1.40		0.3805	8.289	0.3157	297.5	291	267.5	84.6	3.44
3.5-1.2-1.50		0.394	8.305	0.3195	293.5	288.5	264.5	83.6	3.47
3.5-1.2-1.60		0.4065	8.316	0.3157	293.5	386	264.5	83.4	3.43
3.5-1.2-1.70		0.4195	8.318	0.3175	295.5	287	266	84.6	3.39
3.5-1.2-1.80	C	0.432	8.301	0.3187	292.5	291	263.5	84.0	3.46
3.5-1.2-1.90		0.445	8.301	0.3185	294.5	289.5	265.5	84.6	3.42
3.5-1.2-1.100		0.453	8.301	0.3187	292.5	292.5	263.5	83.7	3.49

RUN	P_∞ [at]	M_∞ [-]	U_∞ [m/s]	$R \cdot 10^{-7}$ [1/m]	$R'_x \cdot 10^{-7}$ [-]	ΔX_v [m]	$R_x 10^{-7}$ [-]	$\rho_\infty U_\infty$ [kg/m²·s]	$F \cdot 10^3$ [-]
3.5-1.2-1.10	0.0977	3.575	654.2	4.659	1.586		1.537	262.3	1.167
3.5-1.2-1.20	0.0996	3.561	653.8	4.682	1.654		1.608	265.4	1.165
3.5-1.2-1.30	0.1001	3.558	655.2	4.655	1.702	+0.02	1.657	265.7	1.172
3.5-1.2-1.40	0.1018	3.546	653.9	4.698	1.777		1.716	268.9	1.165
3.5-1.2-1.50	0.1021	3.545	649.7	4.802	1.878		1.780	271.3	1.179
3.5-1.2-1.60	0.1015	3.549	650.0	4.793	1.936		1.840	270.2	1.165
3.5-1.2-1.70	0.1043	3.530	651.1	4.788	1.995		1.903	274.1	1.172
3.5-1.2-1.80	0.1052	3.524	647.5	4.878	2.094	+0.02	1.962	277.1	1.177
3.5-1.2-1.90	0.1051	3.525	649.9	4.821	2.131		2.023	275.9	1.176
3.5-1.2-1.100	0.1039	3.532	647.9	4.852	2.181		2.062	274.6	1.177

RUN	Θ [mm]	δ^* [mm]	δ [mm]	$\int_0^\delta \rho/\rho_w \, dy$ [mm]	H [-]	R_Θ [-]	$c_{f_1} 10^3$ [-]	$c_{f_2} 10^3$ [-]	$c_{f_3} 10^3$ [-]
3.5-1.2-1.10	0.480	3.578	6.82	13.80	7.46	22830		0.53	0.61
3.5-1.2-1.20	0.503	3.734	7.141	14.50	7.42	23950		0.53	0.59
3.5-1.2-1.30	0.5285	3.928	7.435	14.81	7.43	25150		0.50	0.59
3.5-1.2-1.40	0.5415	4.023	7.585	15.13	7.43	25780		0.48	0.58
3.5-1.2-1.50	0.559	4.150	7.75	15.43	7.43	26600	0.56 (0.76)	0.47	0.565
3.5-1.2-1.60	0.578	4.253	8.05	16.00	7.36	27530		0.47	0.56
3.5-1.2-1.70	0.604	4.445	8.45	16.62	7.35	28750		0.45	0.55
3.5-1.2-1.80	0.625	4.605	8.705	17.42	7.35	29750		0.44	0.54
3.5-1.2-1.90	0.6425	4.705	8.99	17.97	7.34	30580		0.47	0.535
3.5-1.2-1.100	0.6478	4.770	9.15	18.74	7.35	30850		0.47	0.53

TABLE IX-0

RUN	PLATE	X' [m]	P_o [at]	$\rho_w V_w$ [kg/m²·s]	T_o [°K]	T_w [°K]	T_r [°K]	T_∞ [°K]	T_w/T_∞ [-]
3.5-2.1-1.10		0.341	8.299	0.588	293	289.5	261	83.7	3.46
3.5-2.1-1.20		0.3535	8.299	0.589	293.5	289.5	261.5	83.8	3.455
3.5-2.1-1.30	C	0.3655	8.299	0.584	294.5	289	262.5	84.4	3.425
3.5-2.1-1.40		0.3785	8.307	0.587	292	291	261	84.1	3.46
3.5-2.1-1.50		0.391	8.306	0.5847	292.5	291.5	261.5	83.9	3.475
3.5-2.1-1.60		0.404	8.317	0.585	295.5	288.5	263	85.1	3.39
3.5-2.1-1.70	C	0.4165	8.317	0.584	296	287.1	263.5	85.6	3.355
3.5-2.1-1.80		0.4295	8.301	0.588	293.5	292.5	261.5	84.6	3.455
3.5-2.1-1.90		0.4415	8.300	0.584	296	291.5	264	85.3	3.42

RUN	P_∞ [at]	M_∞ [-]	U_∞ [m/s]	$R \cdot 10^{-7}$ [1/m]	$R'_x \cdot 10^{-7}$ [-]	ΔX_v [m]	$R_x \cdot 10^{-7}$ [-]	$\rho_\infty U_\infty$ [kg/m²·s]	$F \cdot 10^3$ [-]
3.5-2.1-1.10	0.1031	3.538	648.8	4.829	1.646		1.410	273.1	2.115
3.5-2.1-1.20	0.1029	3.539	649.5	4.813	1.702		1.470	272.6	2.120
3.5-2.1-1.30	0.1042	3.530	650.2	4.807	1.758	+0.05	1.528	274.4	2.110
3.5-2.1-1.40	0.1064	3.516	646.6	4.911	1.859		1.592	279.4	2.113
3.5-2.1-1.50	0.1049	3.526	647.6	4.873	1.906		1.652	276.5	2.104
3.5-2.1-1.60	0.1067	3.514	650.0	4.832	1.952		1.716	278.4	2.105
3.5-2.1-1.70	0.1081	3.505	650.2	4.838	2.016	+0.05	1.776	280.5	2.110
3.5-2.1-1.80	0.1066	3.514	647.9	4.879	2.095		1.838	279.1	2.115
3.5-2.1-1.90	0.1065	3.515	651.0	4.804	2.123		1.897	277.5	2.110

RUN	Θ [mm]	δ^* [mm]	δ [mm]	$\int_0^\delta \rho/\rho_w \, dy$ [mm]	H [-]	R_Θ [-]	$c_{f_1} \cdot 10^3$ [-]	$c_{f_2} \cdot 10^3$ [-]	$c_{f_3} \cdot 10^3$ [-]
3.5-2.1-1.10	0.630	5.033	8.64	16.22	7.98	30500		0.25	0.39
3.5-2.1-1.20	0.6645	5.355	9.08	16.86	8.06	32170		0.25	0.38
3.5-2.1-1.30	0.6905	5.485	9.36	17.33	7.94	33450		0.23	0.37
3.5-2.1-1.40	0.722	5.720	9.89	18.33	7.92	34900		0.20	0.36
3.5-2.1-1.50	0.749	5.94	10.19	18.97	7.95	36270	0.37 (0.57)	0.21	0.35
3.5-2.1-1.60	0.794	6.271	10.76	19.80	7.89	38450		0.20	0.34
3.5-2.1-1.70	0.817	6.292	11.00	20.40	7.70	39550		0.23	0.335
3.5-2.1-1.80	0.805	6.263	11.08	21.19	7.78	39000		0.25	0.33
3.5-2.1-1.90	0.8175	6.271	11.13	21.40	7.68	39600		0.28	0.325

TABLE X-0

RUN	PLATE	X' [m]	P_o [at]	$\varrho_w V_w$ [kg/m²·s]	T_o [°K]	T_w [°K]	T_r [°K]	T_∞ [°K]	T_w/T_∞ [-]
2.5-0.4-2.70		0.4113	5.241	0.1837	294.5	273.5	274	127.5	2.145
2.5-0.4-2.100		0.4493	5.221	0.1856	297	274	276.5	129.5	2.115
2.5-0.8-2.70	A	0.411	5.239	0.3420	295	275.5	273.5	127.5	2.16
2.5-1,2-2.10		0.335	5.249	0.545	294	275	272.5	130	2.115
2.5-1.2-2.30		0.3605	5.249	0.563	292	271.5	270.5	128	2.12
2.5-1.2-2.50		0.3855	5.252	0.5675	293	271	271	128	2.115
2.5-1.2-2.70	A	0.411	5.251	0.5695	293.5	271.5	271.5	126.5	2.145
2.5-1.2-2.90		0.4365	5.253	0.5697	294.5	274.5	272.5	127.5	2.15
2.5-1.2-2.100		0.4495	5.250	0.5705	295	274.5	273	129	2.125

RUN	P_∞ [at]	M_∞ [-]	U_∞ [m/s]	$R \cdot 10^{-7}$ [1/m]	$R'_x 10^{-7}$ [-]	ΔX_v [m]	$R_x 10^{-7}$ [-]	$\varrho_\infty U_\infty$ [kg/m²·s]	$F \cdot 10^3$ [-]
2.5-0.4-2.70	0.2769	2.564	580	4.944	2.034	-0.02	2.130	431	0.416
2.5-0.4-2.100	0.2863	2.542	580	4.934	2.218	-0.02	2.317	438	0.415
2.5-0.8-2.100	0.2791	2.559	579.5	4.949	2.036	0	2.036	433	0.790
2.5-1.2-2.10	0.2927	2.518	575	5.079	1.701	+0.015	1.553	450.5	1.230
2.5-1.2-2.30	0.2911	2.532	574.5	5.089	1.835	+0.015	1.730	446	1.270
2.5-1.2-2.50	0.2878	2.539	576	5.045	1.948	+0.015	1.856	442.5	1.281
2.5-1.2-2.70	0.2737	2.572	579.5	4.953	2.038	+0.015	1.984	429	1.285
2.5-1.2-2.90	0.2804	2.556	579	4.965	2.165	+0.015	2.113	434.5	1.285
2.5-1.2-2.100	0.2893	2.536	577.5	5.003	2.249	+0.015	2.177	442	1.287

RUN	Θ [mm]	δ^* [mm]	δ [mm]	$\int_0^\delta \varrho/\varrho_w \, dy$ [mm]	H [-]	R_Θ [-]	$c_{f_1} 10^3$ [-]	$c_{f_2} 10^3$ [-]	
2.5-0.4-2.70	0.5298	2.175	6.325	10.50	4.10	26200	1.19	1.22	
2.5-0.4-2.100	0.5805	2.223	6.375	10.37	4.19	26250		1.20	
2.5-0.8-2.70	0.5798	2.448	6.96	11.51	4.15	29200	1.03	1.08	
2.5-1.2-2.10	0.562	2.435	5.85	9.04	4.33	28500	0.72	0.71	
2.5-1.2-2.30	0.5965	2.540	6.40	10.07	4.26	30400	0.72	0.74	
2.5-1.2-2.50	0.659	2.805	6.89	10.73	4.26	33250		0.71	
2.5-1.2-2.70	0.698	2.935	7.88	12.75	4.20	35000	0.72	0.79	
2.5-1.2-2.90	0.759	3.213	8.38	13.48	4.23	37680		0.74	
2.5-1.2-2.100	0.7695	3.237	8.55	13.72	4.20	28530		0.71	

TABLE XI-O

RUN	PLATE	X' [m]	P_o [at]	$\rho_w V_w$ [kg/m²·s]	T_o [°K]	T_w [°K]	T_r [°K]	T_∞ [°K]	T_w/T_∞ [-]
3.5-1.2-2.30	C	0.368	8.298	0.3325	297.5	276	268	84.8	3.255
3.5-1.2-2.40		0.3805	8.298	0.3287	293	267.5	264	83.5	3.205
3.5-1.2-2.90		0.445	8.305	0.3295	292.5	272	263.5	84.0	3.235
3.5-1.2.2.100		0.453	8.305	0.3333	295	273	265.5	84.8	3.22
3.5-2.2-2.30	C	0.3655	8.298	0.624	297.5	267.5	265	85.7	3.12
3.5-2.2-2.40		0.378	8.300	0.6195	292	269.5	263	84.0	3.21
3.5-2.2-2.60		0.4045	8.301	0.609	292	275.5	264	84.5	3.26
3.5-2.2-2.90		0.4415	8.305	0.644	291.5	274	262	84.0	3.27

RUN	P_∞ [at]	M_∞ [-]	U_∞ [m/s]	$R \cdot 10^{-7}$ [1/m]	$R'_x 10^{-7}$ [-]	ΔX_v [m]	$R_x 10^{-7}$ [-]	$\rho_\infty U_\infty$ [kg/m²s]	$F \cdot 10^3$ [-]
3.5-1.2-2.30	0.1021	3.544	654	4.695	1.716		1.658	269.5	1.223
3.5-1.2-2.40	0.1022	3.543	649	4.811	1.820	+0.02	1.717	271.5	1.204
3.5-1.2-2.90	0.1051	3.524	647.5	4.874	2.154		2.025	277	1.212
3.5-1.2-2.100	0.1055	3.521	650	4.817	2.166		2.065	276.5	1.225
3.5-2.2-2.30	0.1063	3.515	652.5	4.766	1.742		1.530	276.5	2.240
3.5-2.2-2.40	0.1057	3.520	647	4.894	1.851	+0.05	1.592	278	2.220
3.5-2.2-2.60	0.1079	3.505	646	4.929	1.992		1.720	282	2.185
3.5-2.2-2.90	0.1065	3.514	645.5	4.929	2.278		1.898	280	2.310

RUN	Θ [mm]	δ^* [mm]	δ [mm]	$\int_0^\delta \rho/\rho_w \, dy$ [mm]	H [-]	R_Θ [-]	$c_{f_1} 10^3$ [-]	$c_{f_2} 10^3$ [-]	
3.5-1.2-2.30	0.5385	3.91	7.44	14.30	7.26	25680		0.45	
3.5-1.2-2.40	0.565	4.00	7.575	14.30	7.08	26950	0.56	0.47	
3.5-1.2-2.90	0.679	4.81	9.20	17.60	7.09	27600	(0.76)	0.44	
3.5-1.2-2.100	0.680	4.79	9.235	17.62	7.06	27600		0.44	
3.5-2.2-2.30	0.716	5.575	9.43	16.16	7.78	34750		0.15	
3.5-2.2-2.40	0.761	5.905	10.07	17.68	7.76	36930		0.20	
3.5-2.2-2.60	0.8315	6.40	11.02	19.80	7.70	40350	0.29	0.20	
3.5-2.2-2.90	0.881	6.615	11.83	21.87	7.51	42750	(0.49)	0.22	

TABLE XII-0

RUN	PLATE	X' [m]	P_o [at]	$\rho_w V_w$ [kg/m²·s]	T_o [°K]	T_w [°K]	T_r [°K]	T_∞ [°K]	T_w/T_∞ [-]
2.5-0.4-3.10	A	0.3353	5.223	0.1878	293	269	273	129	2.085
2.5-0.8-3.10	A	0.335	5.241	0.362	294	256.5	273	130	1.975
2.5-0.9-3.11	C	0.335	5.218	0.4300	295.5	264	274.5	130.5	2.02
2.5-0.8-3.100	A	0.4495	5.221	0.346	295.5	263	274	129	2.04
2.5-1.2-3.10	A	0.335	5.240	0.5915	294.5	264	272	130.5	2.02
2.5-1.4-3.11	C	0.335	5.218	0.6635	293.5	258	271	130	1.985
2.5-1.2-3.100	A	0.4495	5.221	0.590	296	262.5	274.5	130	2.02

RUN	P_∞ [at]	M_∞ [-]	U_∞ [m/s]	$R \cdot 10^{-7}$ [1/m]	$R'_x 10^{-7}$ [-]	ΔX_v [m]	$R_x 10^{-7}$ [-]	$\rho_\infty U_\infty$ [kg/m²·s]	$F \cdot 10^3$ [-]
2.5-0.4-3.10	0.2964	2.520	574.2	5.090	1.707	-0.02	1.807	450.2	0.4195
2.5-0.8-3.10	0.2979	2.517	574.8	5.075	1.702		1.702	451	0.803
2.5-0.9-3.11	0.2967	2.518	576.5	5.027	1.683	0	1.683	448.5	0.960
2.5-0.8-3.100	0.2878	2.539	578.2	4.985	2.241		2.241	440.5	0.787
2.5-1.2-3.10	0.3018	2.508	574.5	5.086	1.705		1.756	454	1.310
2.5-1.4-3.11	0.3022	2.507	573	5.113	1.712	+0.015	1.583	455	1.460
2.5-1.2-3.100	0.2946	2.524	577.5	5.005	2.250		2.175	446	1.306

RUN	Θ [mm]	δ^* [mm]	δ [mm]	$\int_0^\delta \rho/\rho_w \, dy$ [mm]	H [-]	R_Θ [-]	$c_{f_1} 10^3$ [-]	$c_{f_2} 10^3$ [-]	
2.5-0.4-3.10	0.4195	1.710	4.84	7.77	4.08	21350	1.19	1.20	
2.5-0.8-3.10	0.4925	1.983	5.245	7.885	4.03	25000		0.99	
2.5-0.9-3.11	0.4927	2.033	5.055	7.64	4.12	24830	1.03	1.11	
2.5-0.8-3.100	0.6715	2.690	7.25	11.27	4.00	33500		1.06	
2.5-1.2-3.10	0.5625	2.355	6.045	8.70	4.19	28550		0.75	
2.5-1.4-3.11	0.589	2.445	5.75	8.35	4.15	30070	0.725	0.70	
2.5-1.2-3.100	0.788	3.163	8.44	12.91	4.01	39450		0.76	

TABLE XIII-0

RUN	PLATE	X' [m]	P_o [at]	$\rho_w V_w$ [kg/m²·s]	T_o [°K]	T_w [°K]	T_r [°K]	T_∞ [°K]	T_w/T_∞ [-]
3.5-1.2-3.10		0.343	8.298	0.328	296	265.5	266.5	83.6	3.175
3.5-1.2-3.20		0.359	8.298	0.3335	297	264.5	267	84.6	3.125
3.5-1.2-3.60	C	0.4065	8.300	0.3295	296.5	264	267	84.5	3.125
3.5-1.2-3.70		0.4195	8.300	0.3377	297.5	256	268	85.9	2.98
3.5-1.2-3.80		0.432	8.300	0.3345	297.5	261	268	86.0	3.035
3.5-2.2-3.10		0.3405	8.298	0.622	294.5	265.5	262	84.2	3.155
3.5-2.2-3.20	C	0.353	8.298	0.6435	296.5	255.5	263	85.3	2.99
3.5-2.2-3.50		0.3907	8.300	0.619	293.5	256	263	84.8	3.02
3.5-2.2-3.70		0.4165	8.301	0.646	297	247.5	265	86.5	2.86

RUN	P_∞ [at]	M_∞ [-]	U_∞ [m/s]	$R \cdot 10^{-7}$ [1/m]	$R'_x 10^{-7}$ [-]	Δx_v [m]	$R_x 10^{-7}$ [-]	$\rho_\infty U_\infty$ [kg/m²s]	$F \cdot 10^3$ [-]
3.5-1.2-3.10	0.09903	3.566	653.5	4.682	1.594		1.540	264.5	1.207
3.5-1.2-3.20	0.1025	3.541	653	4.721	1.667		1.617	270.5	1.227
3.5-1.2-3.60	0.1023	3.543	653	4.721	1.908	+0.020	1.843	270	1.212
3.5-1.2-3.70	0.1075	3.508	652	4.789	1.995		1.904	278.5	1.241
3.5-1.2-3.80	0.1075	3.508	652	4.784	2.054		1.964	278.5	1.230
3.5-2.2-3.10	0.1039	3.532	650	4.807	1.636		1.408	274	2.230
3.5-2.2-3.20	0.1060	3.518	651.5	4.784	1.689	+0.050	1.470	276.5	2.307
3.5-2.2-3.50	0.1071	3.510	648	4.877	1.907		1.653	279.5	2.220
3.5-2.2-3.70	0.1104	3.489	650.5	4.838	2.015		1.778	283.5	2.320

RUN	Θ [mm]	δ^* [mm]	δ [mm]	$\int_0^\delta \rho/\rho_w dy$ [mm]	H [-]	R_Θ [-]	$c_{f_1} 10^3$ [-]	$c_{f_2} 10^3$ [-]	
3.5-1.2-3.10	0.5105	3.655	6.94	12.98	7.15	24350		0.47	
3.5-1.2-3.20	0.543	3.847	7.275	13.44	7.08	25930		0.46	
3.5-1.2-3.60	0.612	4.315	8.20	15.18	7.05	29200	0.50	0.44	
3.5-1.2-3.70	0.669	4.595	8.66	15.32	6.87	31850	(0.70)	0.40	
3.5-1.2-3.80	0.673	4.645	8.865	15.80	6.89	32100		0.40	
3.5-2.2-3.10	0.676	5.18	8.925	15.62	7.67	32750		0.21	
3.5-2.2-3.20	0.731	5.505	9.415	15.67	7.53	35470		0.18	
3.5-2.2-3.50	0.834	6.21	10.62	17.83	7.45	40400	0.28	0.18	
3.5-2.2-3.70	0.923	6.615	11.58	18.82	7.18	44730	(0.48)	0.16	

TABLE XIV-0

RUN	PLATE	X' [m]	P_o [at]	$\rho_w V_w$ [kg/m²·s]	T_o [°K]	T_w [°K]	T_r [°K]	T_∞ [°K]	T_w/T_∞ [-]
3.5-0.6-R10		0.3405	8.311	0.1730	294	290.5	266	83.0	3.50
3,5-0.6-R20		0.3533	8.311	0.1708	295	291.5	267	83.1	3.55
3.5-0.6-R30	D	0.3663	8.311	0.1727	295.5	290.5	267.5	82.9	3.545
3.5-0.6-R40		0.3790	8.311	0.1708	296	290	268	83.9	3.455
3.5-0.6-R50		0.3917	8.311	0.1693	297.5	291	269	84.3	3.45
3.5-0.6-R60		0.4043	8.310	0.1688	299	292.5	270.5	84.8	3.45
3.5-0.6-R70		0.4170	8.311	0.1701	297	292.5	269	85.0	3.44
3.5-0.6-R80	B	0.4290	8.310	0.1701	297.5	292.5	269	85.3	3.43
3.5-0.6-R90		0.4420	8.310	0.1700	298	292	269.5	85.2	3.425
3.5-0.6-R100		0.4485	8.310	0.1700	298.5	293.5	270.5	85.8	3.42

RUN	P_∞ [at]	M_∞ [-]	U_∞ [m/s]	$R \cdot 10^{-7}$ [1/m]	$R'_x 10^{-7}$ [-]	ΔX_v [m]	$R_x 10^{-7}$ [-]	$\rho_\infty U_\infty$ [kg/m²·s]	$F \cdot 10^3$ [-]
3.5-0.6-R10	0.0993	3.565	651	4.749	1.616		1.604	266.0	0.645
3.5-0.6-R20	0.0981	3.573	653	4.694	1.659		1.663	263.5	0.636
3.5-0.6-R30	0.0971	3.581	653.5	4.700	1.710	0	1.725	261.5	0.644
3.5-0.6-R40	0.1004	3.557	653	4.708	1.784		1.786	267	0.636
3.5-0.6-R50	0.1008	3.554	654.5	4.683	1.834		1.846	267	0.631
3.5-0.6-R60	0.1006	3.555	656.5	4.638	1.876		1.904	266	0.629
3.5-0.6-R70	0.1042	3.531	652.5	4.753	1.982		1.964	273.5	0.634
3.5-0.6-R80	0.1048	3.526	652.5	4.750	2.039	0	2.020	274	0.634
3.5-0.6-R90	0.1038	3.533	654	4.721	2.086		2.083	272	0.634
3.5-0.6-R100	0.1056	3.521	654	4.730	2.120		2.113	275	0.634

RUN	Θ [mm]	δ^{**} [mm]	δ [mm]	$\int_0^\delta \rho/\rho_w \, dy$ [mm]	H [-]	R_Θ [-]	$c_{f1} 10^3$ [-]	$c_{f2} 10^3$ [-]	
3.5-0.6-R10	0.4415	3.205	6.475	13.72	7.25	20800		0.690	
3.5-0.6-R20	0.4495	3.295	6.500	13.57	7.33	21180		0.680	
3.5-0.6-R30	0.4600	3.325	6.650	13.94	7.24	21400		0.700	
3.5-0.6-R40	0.4760	3.430	6.880	14.28	7.20	22430		0.680	
3.5-0.6-R50	0.4875	3.517	6.935	14.30	7.21	22970	0.895	0.680	
3.5-0.6-R60	0.5050	3.610	7.100	14.78	7.15	23330	(1.095)	0.700	
3.5-0.6-R70	0.5285	3.783	7.550	15.70	7.16	24880		0.650	
3.5-0.6-R80	0.5400	3.847	7.745	16.09	7.13	25450		0.660	
3.5-0.6-R90	0.5400	3.815	7.790	16.30	7.06	25450		0.700	
3.5-0.6-R100	0.5685	4.035	8.195	17.02	7.09	26770		0.660	

TABLE XV-O

RUN	PLATE	X' [m]	P_o [at]	$\varrho_w V_w$ [kg/m²·s]	T_o [°K]	T_w [°K]	T_r [°K]	T_∞ [°K]	T_w/T_∞ [-]
3.5-2.1-R10		0.3405	8.311	0.570	293.5	293	261.5	83.6	3.505
3.5-2.1-R20		0.3535	8.311	0.570	293.5	292.5	261.5	83.9	3.485
3.5-2.1-R30	D	0.366	8.311	0.570	294.5	292.5	262	84.0	3.48
3.5-2.1-R40		0.3787	8.311	0.570	296	292	264	85.4	3.42
3.5-2.1-R50		0.3915	8.310	0.5675	297	293	264.5	85.1	3.44
3.5-2.1-R60		0.4045	8.310	0.570	295	293.5	263	85.1	3.45
3.5-2.1-R70	D	0.417	8.310	0.5675	296	294	263.5	85.6	3.435
3.5-2.1-R80		0.429	8.310	0.567	297	293.5	264.5	85.9	3.415
3.5-2.1-R90		0.4415	8.310	0.5665	297.5	294.5	265	85.9	3.425

RUN	P_∞ [at]	M_∞ [-]	U_∞ [m/s]	$R \cdot 10^{-7}$ [1/m]	$R'_x 10^{-7}$ [-]	ΔX_v [m]	$R_x 10^{-7}$ [-]	$\varrho_\infty U_\infty$ [kg/m²·s]	$F \cdot 10^3$ [-]
3.5-2.1-R10	0.1020	3.546	650	4.797	1.633		1.394	271	2.063
3.5-2.1-R20	0.1036	3.535	649	4.828	1.706		1.458	274	2.063
3.5-2.1-R30	0.1029	3.540	650.5	4.793	1.756	0.050	1.517	272	2.063
3.5-2.1-R40	0.1067	3.514	651	4.808	1.822		1.578	278	2.063
3.5-2.1-R50	0.1049	3.526	652	4.765	1.866		1.639	274.5	2.055
3.5-2.1-R60	0.1067	3.514	650	4.830	1.953		1.702	278.5	2.063
3.5-2.1-R70	0.1081	3.505	650	4.837	2.017	0.050	1.762	280.5	2.055
3.5-2.1-R80	0.1080	3.505	651.5	4.805	2.063		1.820	280	2.053
3.5-2.1-R90	0.1073	3.510	652	4.786	2.115		1.879	278.5	2.050

RUN	Θ [mm]	δ^* [mm]	δ [mm]	$\int_0^\delta \varrho/\varrho_w \, dy$ [mm]	H [-]	R_Θ [-]	$c_{f_1} 10^3$ [-]	$c_{f_2} 10^3$ [-]	
3.5-2.1-R10	0.640	5.11	8.83	16.86	7.99	30750		0.30	
3.5-2.1-R20	0.660	5.35	9.09	17.07	8.11	31700		0.27	
3.5-2.1-R30	0.6845	5.525	9.37	17.46	8.08	32850		0.27	
3.5-2.1-R40	0.721	5.785	9.905	18.35	8.02	34630		0.22	
3.5-2.1-R50	0.744	5.98	10.15	18.80	8.03	35750	0.40	0.22	
3.5-2.1-R60	0.784	6.195	10.75	20.22	7.90	37650	(0.60)	0.26	
3.5-2.1-R70	0.805	6.31	11.00	20.74	7.84	38650		0.26	
3.5-2.1-R80	0.821	6.375	11.18	21.20	7.77	39380		0.27	
3.5-2.1-R90	0.866	6.79	11.88	22.50	7.83	41600		0.26	

TABLE XVI-0

RUN	PLATE	x' [m]	P_o [at]	$\rho_w V_w$ [kg/m² s]	T_o [°K]	T_w [°K]	T_r [°K]	T_∞ [°K]	T_w/T_∞ [-]
2.5-1.4-1.11		0.335	5.218	0 6665	295	282.5	273	129	2.19
2.5-1.4-1.21		0.348	5.218	0 666	295.5	284	273.5	129.5	2.195
2.5-1.4 1.31	C	0.3605	5.218	0.655	296.5	285	274	129	2.21
2.5-1.4-1.41		0.373	5.218	0.654	297	284.5	275	130	2.19
2.5-1.4-1.51		0.3855	5.220	0.659	292	287.5	270	128	2.245
2.5-1.4-1.61		0.3985	5.221	0.6575	293.5	287	271.5	128	2.24
2.5-1.4-1.71		0.411	5.221	0.6575	293.5	287.5	271.5	126.5	2.275
2.5-1.4-1.81	C	0.424	5.221	0.658	293	287	271	127	2.26
2.5-1.4-1.91		0.4365	5.221	0.657	294	286.5	272	128	2.24
2.5-1.4-1.101		0.4496	5.221	0.656	294.5	286.5	272.5	129.5	2.21

RUN	P_∞ [at]	M_∞ [-]	U_∞ [m/s]	$R \cdot 10^{-7}$ [1/m]	$R'_x \cdot 10^{-7}$ [-]	ΔX_v [m]	$R_x \cdot 10^{-7}$ [-]	$\rho_\infty U_\infty$ [kg/m² s]	$F \cdot 10^3$ [-]
2.5-1.4-1.11	0.2899	2.536	577.5	5.001	1.674		1.548	442	1.495
2.5-1.4-1.21	0.2898	2.534	577.5	4.994	1.738		1.663	442	1.495
2.5-1.4-1.31	0.2853	2.544	579.5	4.946	1.784	0.015	1.725	437.5	1.499
2.5-1.4-1.41	0.2876	2.539	580	4.939	1.844		1.788	439	1.490
2.5-1.4-1.51	0.2903	2.533	574	5.087	1.964		1.850	445.5	1.480
2.5-1.4-1.61	0.2858	2.543	577	5.016	2.000		1.915	440	1.495
2.5-1.4-1.71	0.2746	2.569	579.5	4.951	2.037		1.978	429.5	1.495
2.5-1.4-1.81	0.2803	2.556	577.5	4.997	2.119	0.015	2.043	435	1,513
2.5-1.4-1.91	0.2833	2.549	578	4.991	2.181		2.105	437.5	1.502
2.5-1.4-1.101	0.2925	2.528	576.5	5.031	2.226		2.170	445.5	1.473

RUN	Θ [mm]	δ^* [mm]	δ [mm]	$\int_0^\delta \rho/\rho_w \, dy$ [mm]	H [-]	R_Θ [-]	$c_{f_1} \cdot 10^3$ [-]	$c_{f_2} \cdot 10^3$ [-]	
2.5-1.4-1.11	0.5405	2.370	5.43	8.495	4.38	27000		0.70	
2.5-1.4-1.21	0.564	2.458	5.91	9.42	4.36	28180		0.725	
2.5-1.4-1.31	0.5835	2.568	6.26	10.08	4.40	29130		0.68	
2.5-1.4-1.41	0.6195	2.700	6.54	10.43	4.36	30950		0.70	
2.5-1.4-1.51	0.646	2.820	6.97	11.38	4.37	32250	0.75	0.70	
2.5-1.4-1.61	0.670	2.925	7.21	11.82	4.36	33470		0.71	
2.5-1.4-1.71	0.6845	2.985	7.39	12.19	4.36	34200		0.75	
2.5-1.4-1.81	0.730	3.220	8.05	13.30	4.41	35170		0.70	
2.5-1.4-1.91	0.749	3.290	8.125	13.28	4.39	36150		0.67	
2.5-1.4-1.101	0.789	3.437	8.78	14.40	4.35	39400		0.64	

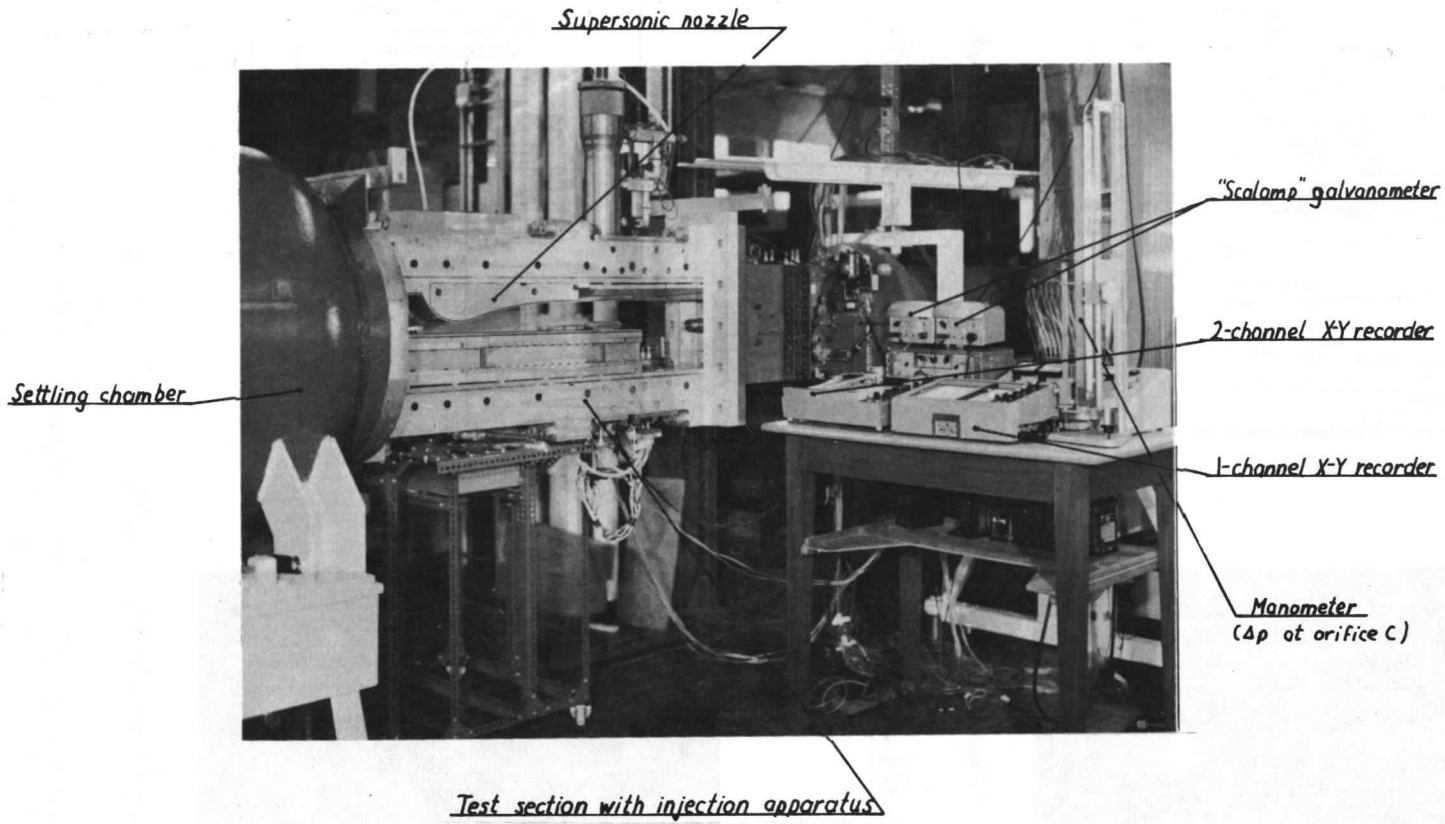

FIG. 1. View of the test section of the wind tunnel. (main view).

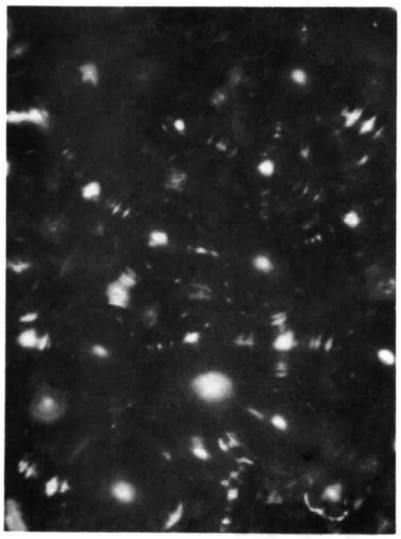

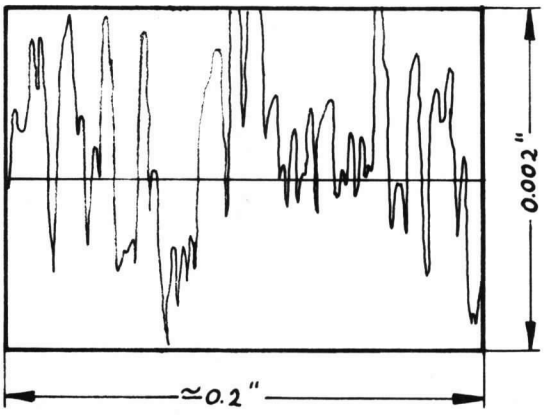

Microphotograph (Magnification: x 200)

Variation of surface roughness

Porosint Grade B (5 microns , rough surface , used for Plate D)

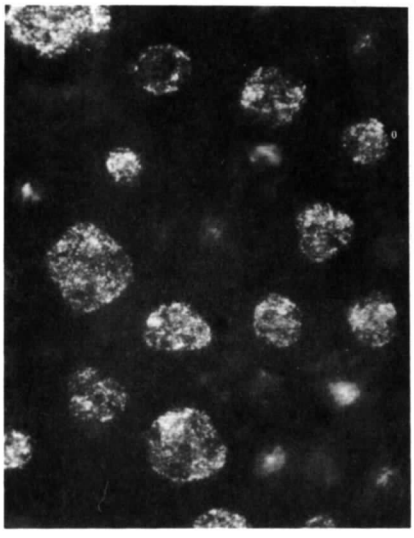

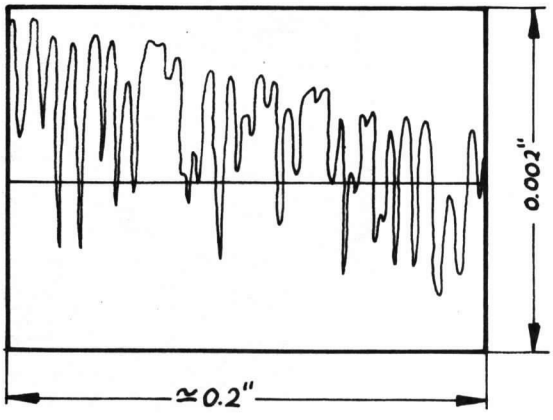

Microphotograph (Magnification: x 200)

Variation of surface roughness

Porosint Grade B (5 microns , rolled surface , used for plate C)

FIG. 2. Porosity and surface roughness of several porous materials.

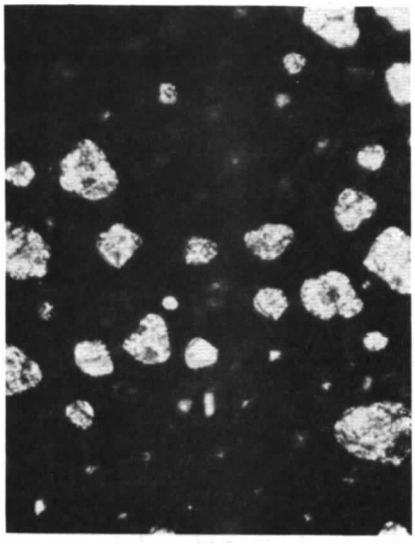

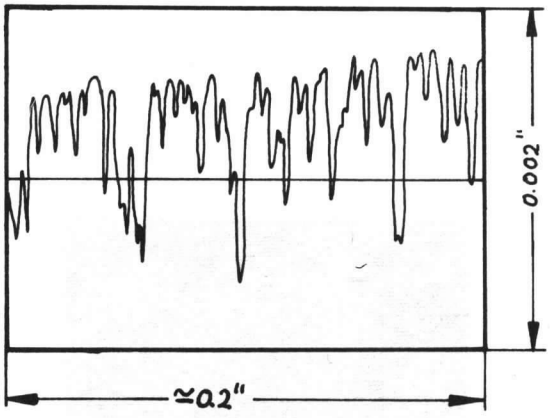

Microphotograph (Magnification: x 200)

Variation of surface roughness

Porosint Grade A (2½ microns, rolled surface, used for plate A)

FIG. 2 (contd.). Porosity and surface roughness of several porous materials.

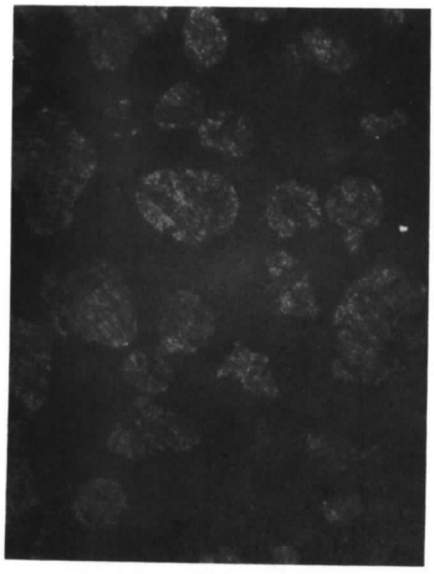

Microphotograph (Magnification : × 100)

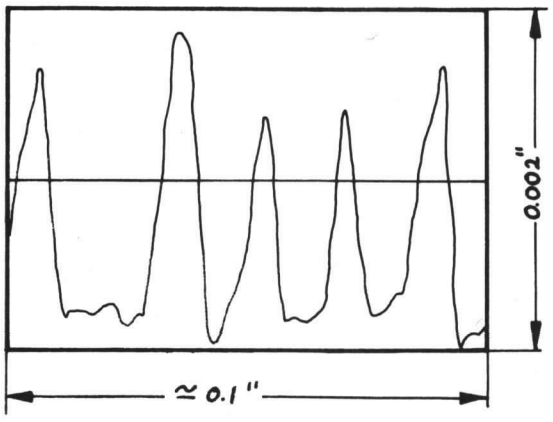

Variation of surface roughness

Vyon

Microphotograph (Magnification : × 100)

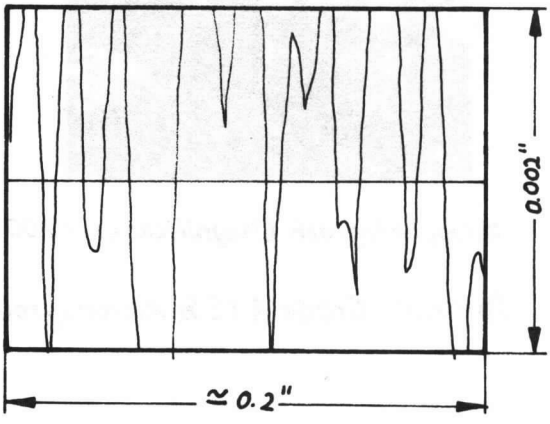

Variation of surface roughness

Porosint Grade E (37½ microns, rolled surface)

FIG. 2 (contd.). Porosity and surface roughness of several porous materials.

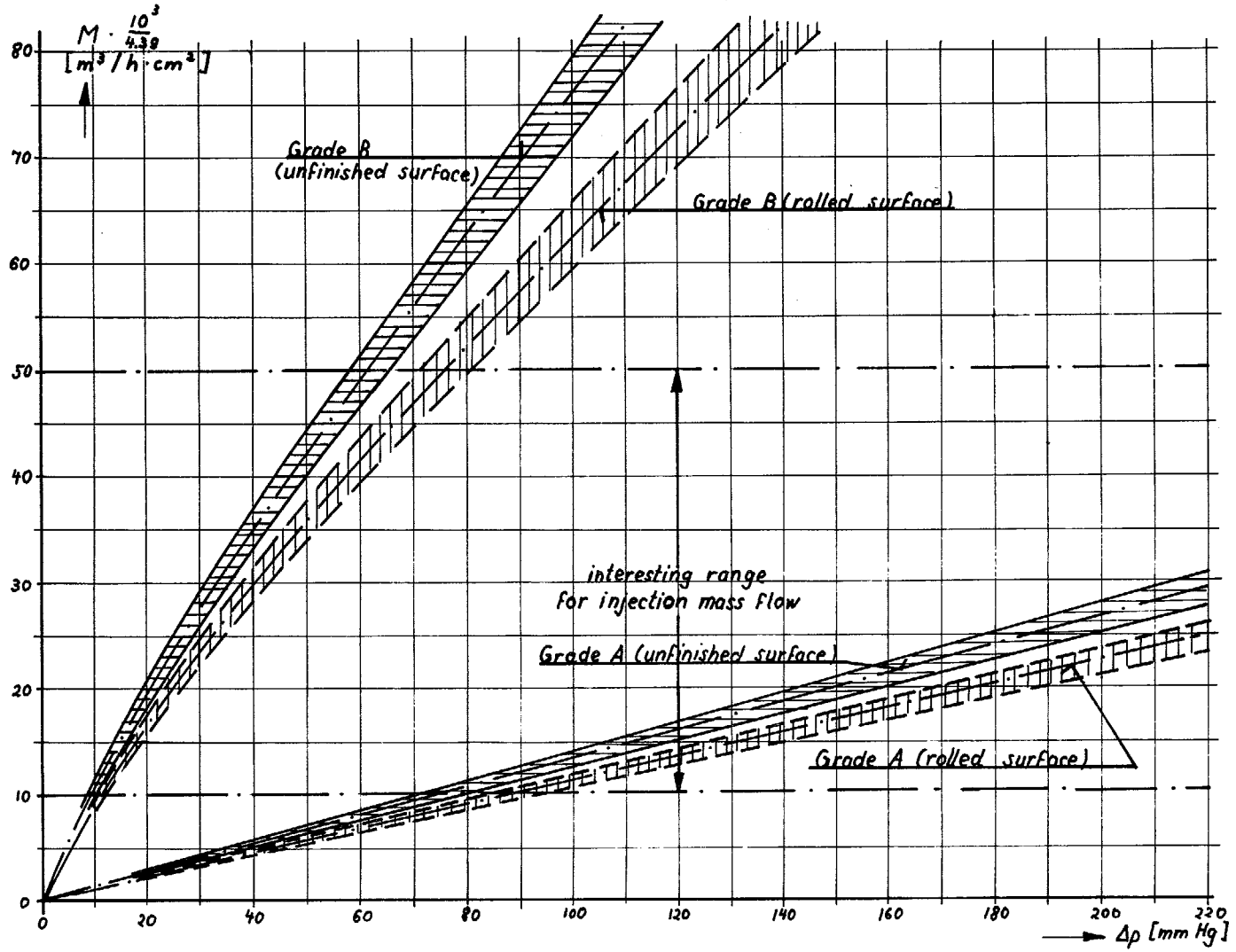

FIG. 3. Porosity variation of test samples (thickness: $\frac{1}{4}''$).

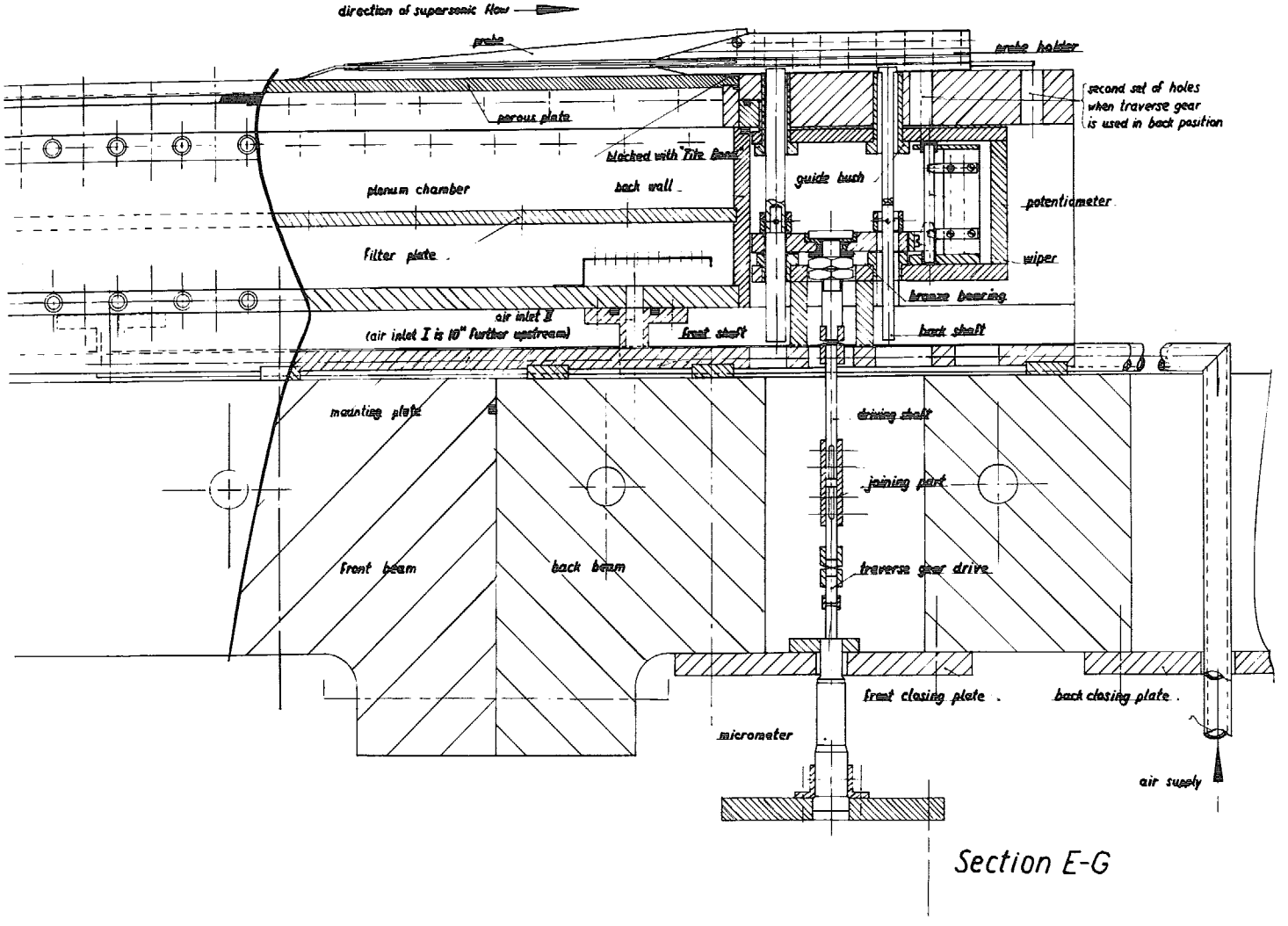

FIG. 4. Injection apparatus.

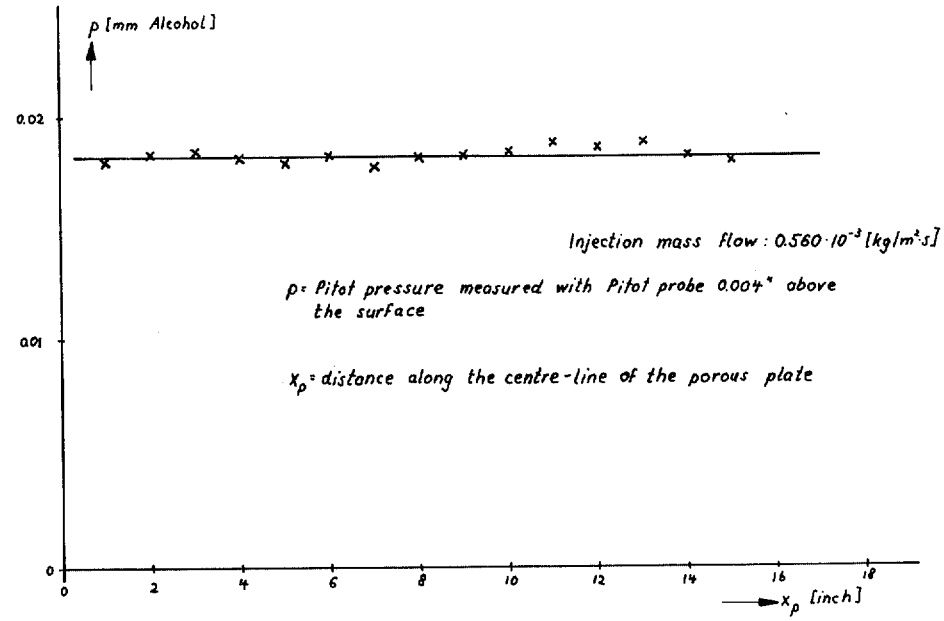

FIG. 5. Variation of injection mass flow along the centreline of the porous plate (Plate C).

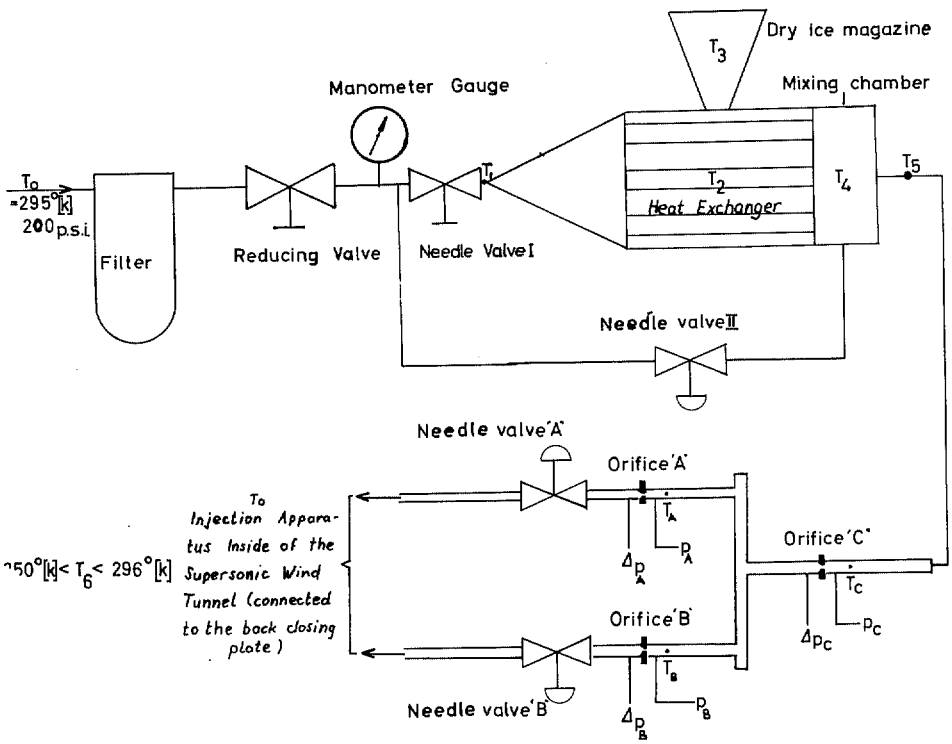

FIG. 6. Air supply for injection mass flow.

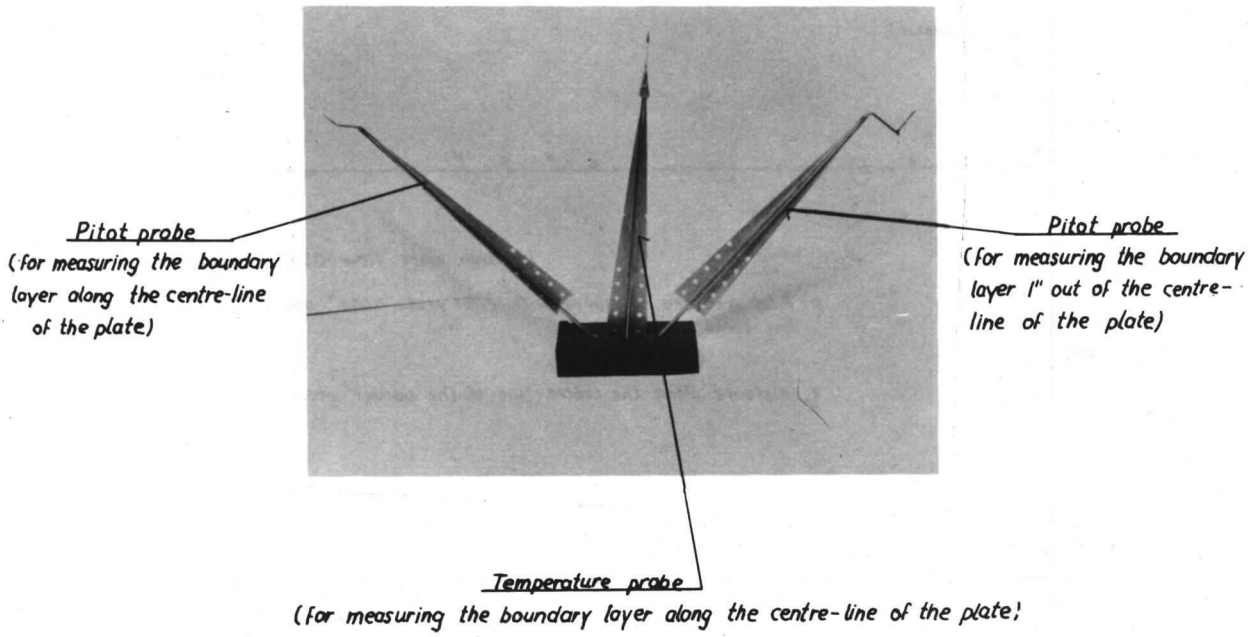

FIG. 7. The boundary layer probes.

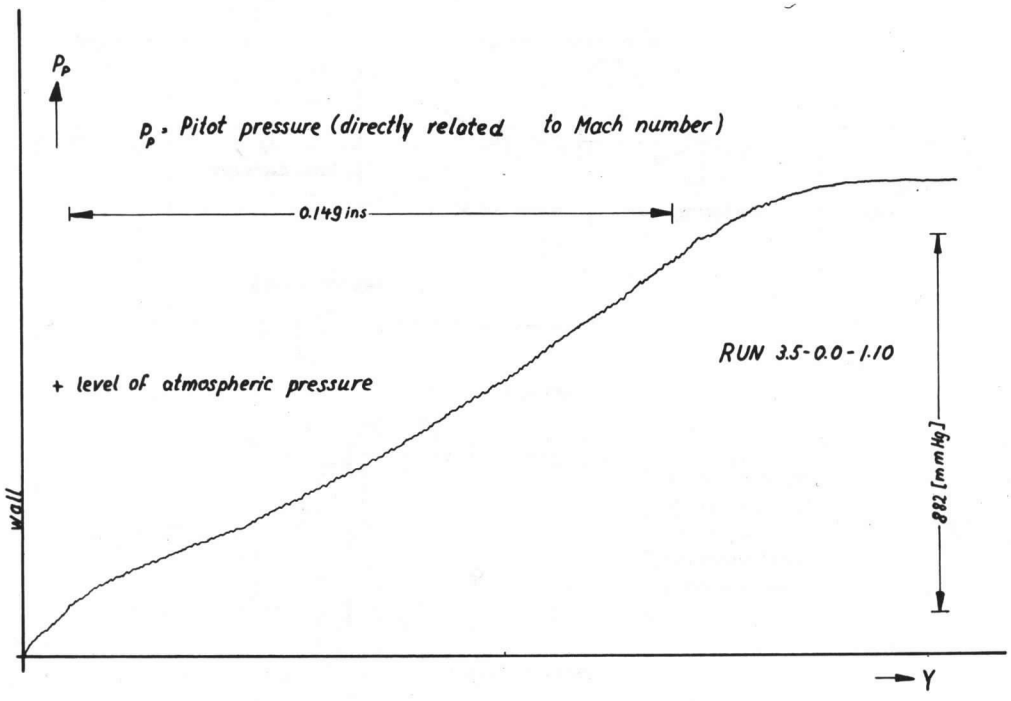

FIG. 8. Typical pitot pressure profile as drawn by X-Y plotter (zero injection, $M_\infty = 3{\cdot}5$).

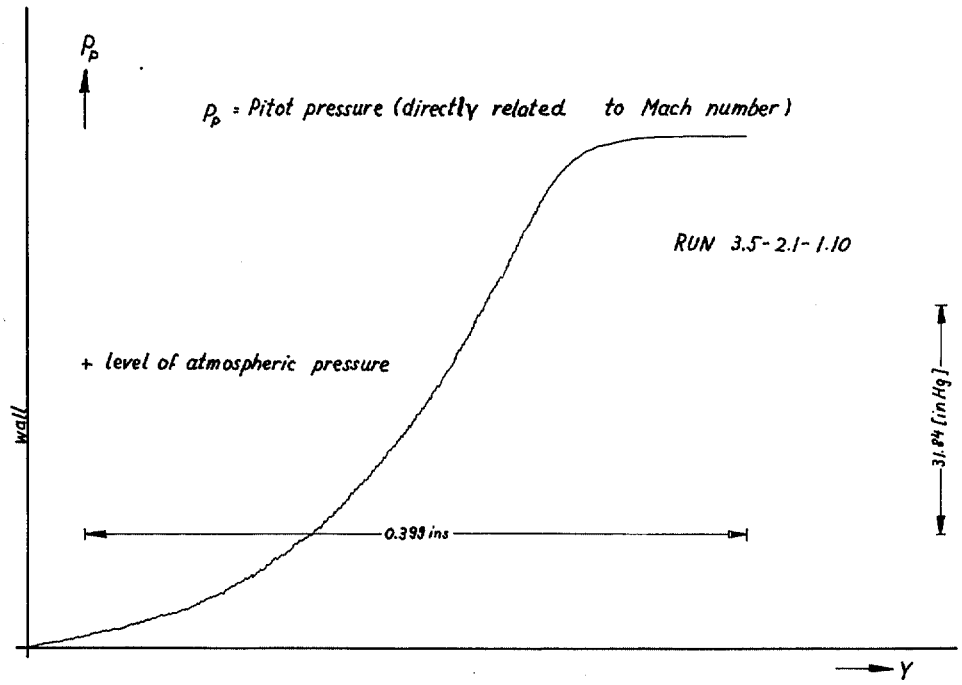

FIG. 9. Typical pitot pressure profile as drawn by X-Y plotter ($F = 2{\cdot}111 \times 10^{-3}$, $M_\infty = 3{\cdot}5$, Station 10).

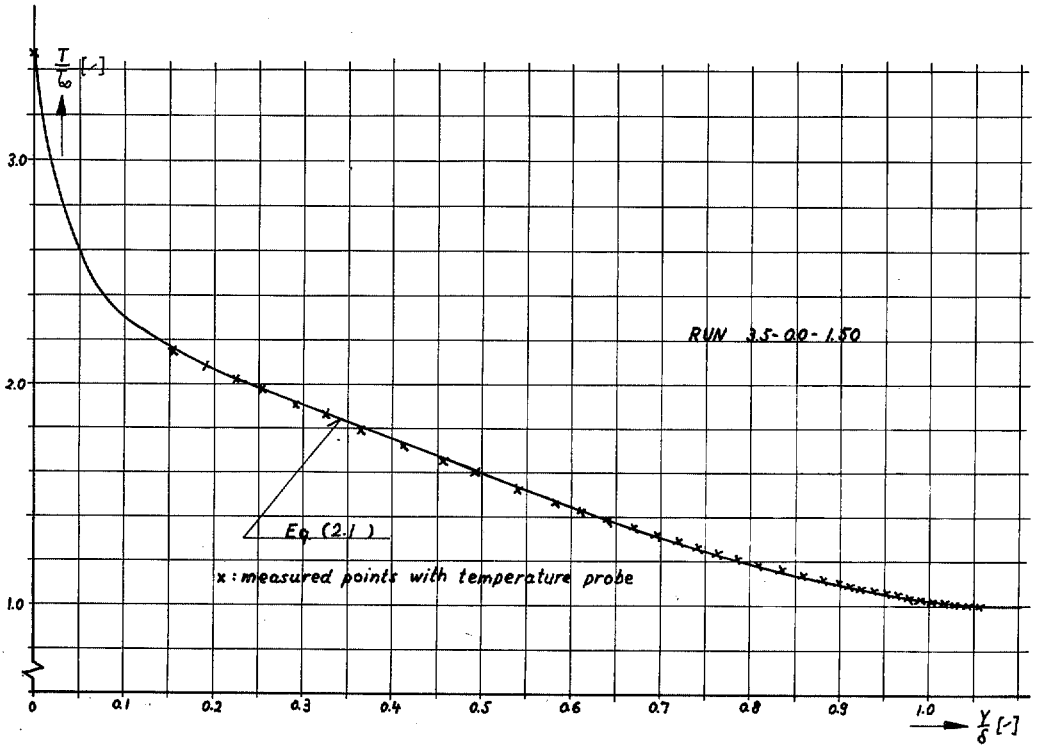

FIG. 10. Typical temperature profile (zero injection, $M_\infty = 3{\cdot}5$).

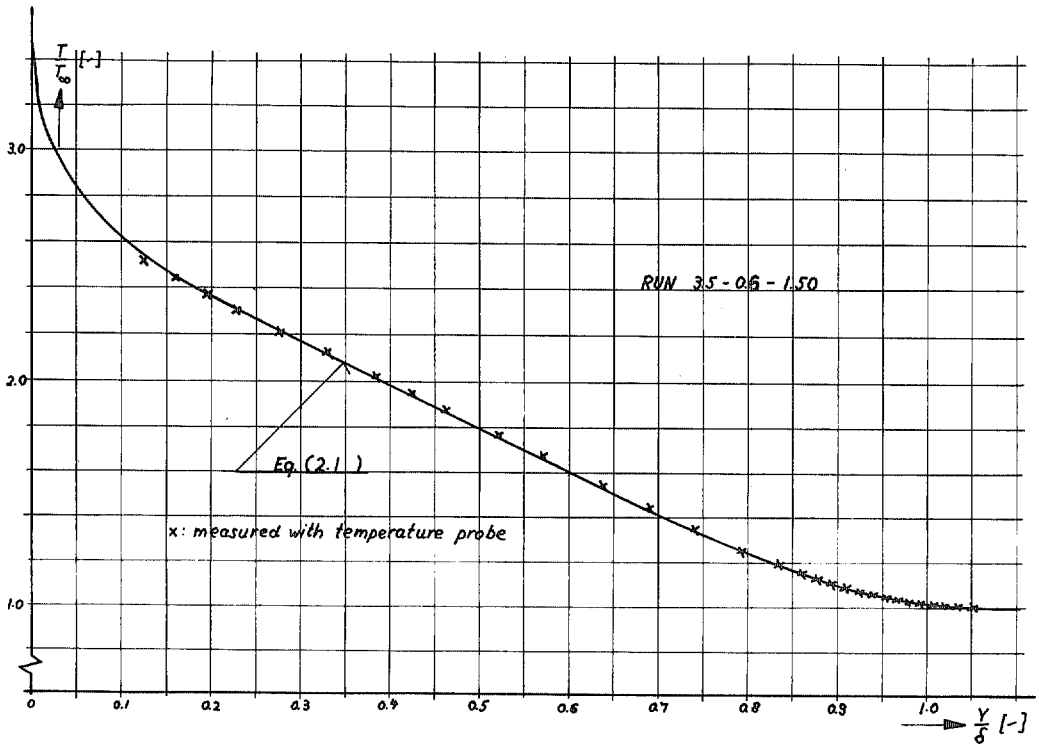

FIG. 11. Typical temperature profile ($F = 0{\cdot}653 \times 10^{-3}$, $M_\infty = 3{\cdot}5$).

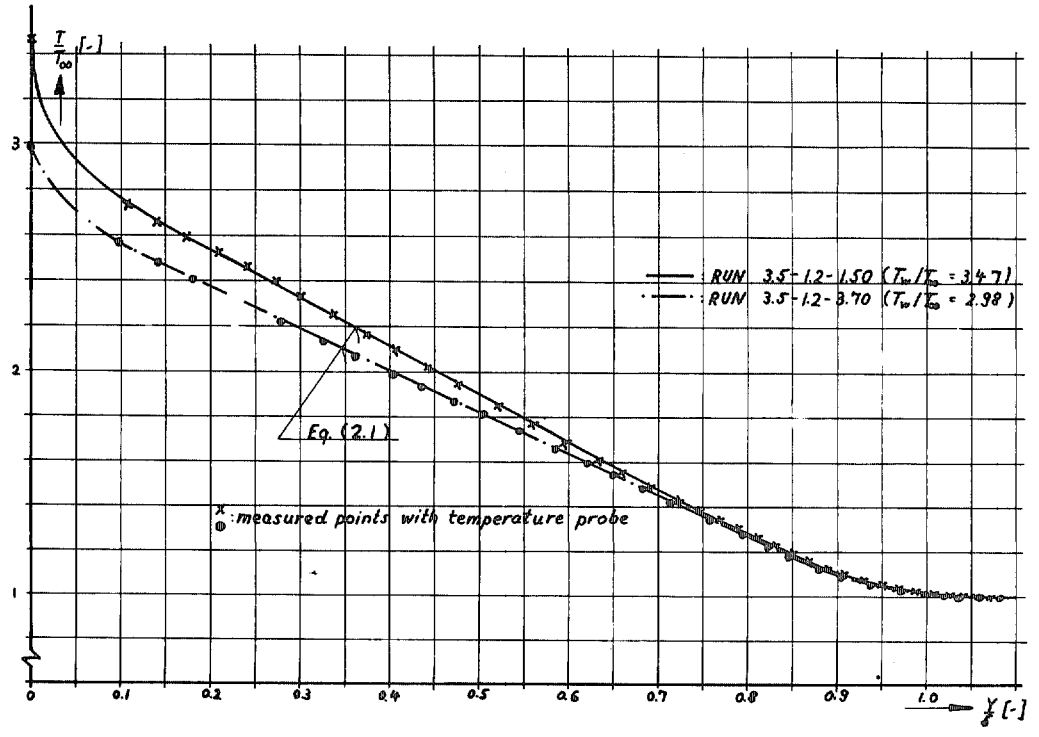

FIG. 12. Typical temperature profile ($F = 1{\cdot}172 \times 10^{-3}$, $M_\infty = 3{\cdot}5$).

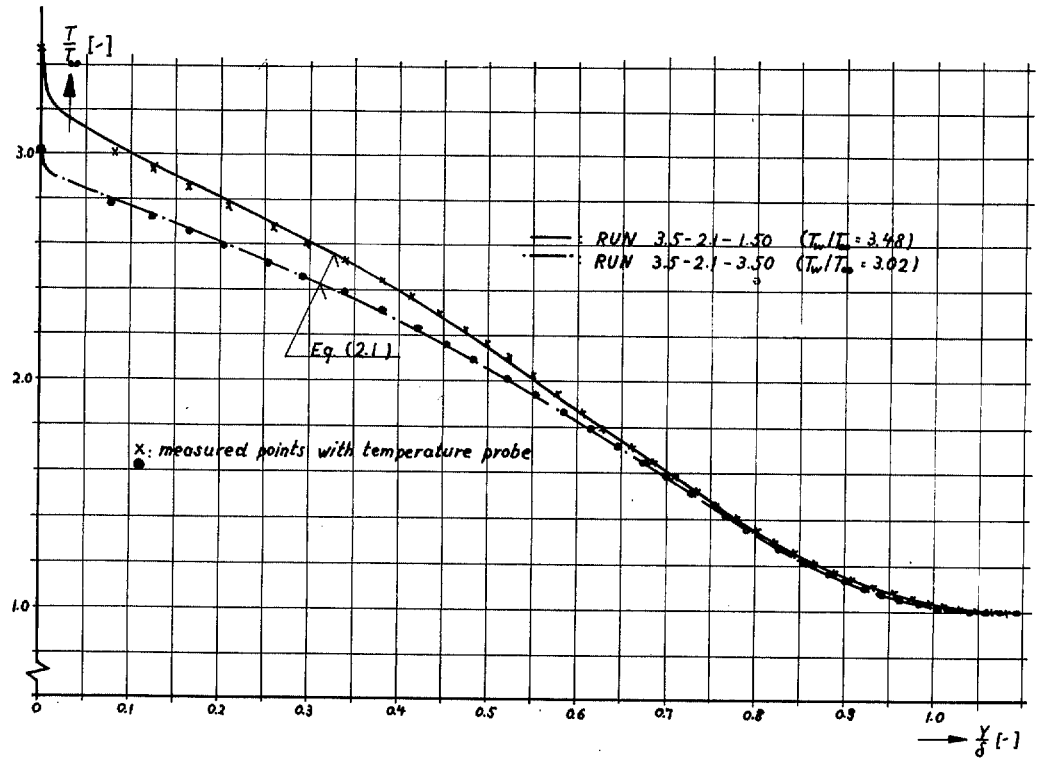

FIG. 13. Typical temperature profile ($F = 2{\cdot}111 \times 10^{-3}$, $M_\infty = 3{\cdot}5$).

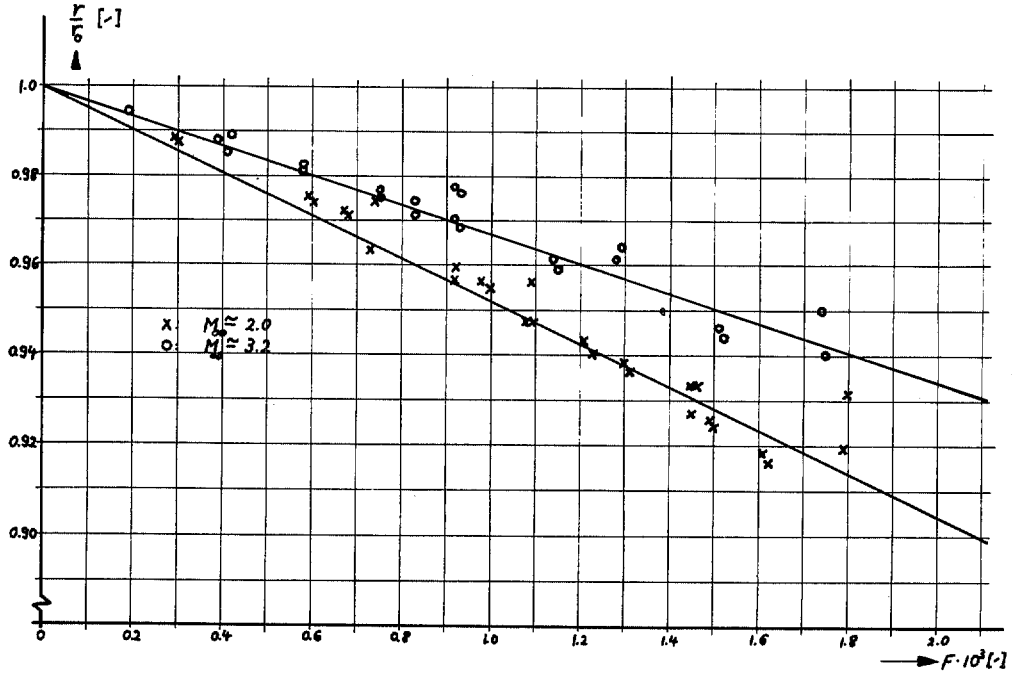

FIG. 14. Effect of air injection on recovery factor after Bartle and Leadon[16].

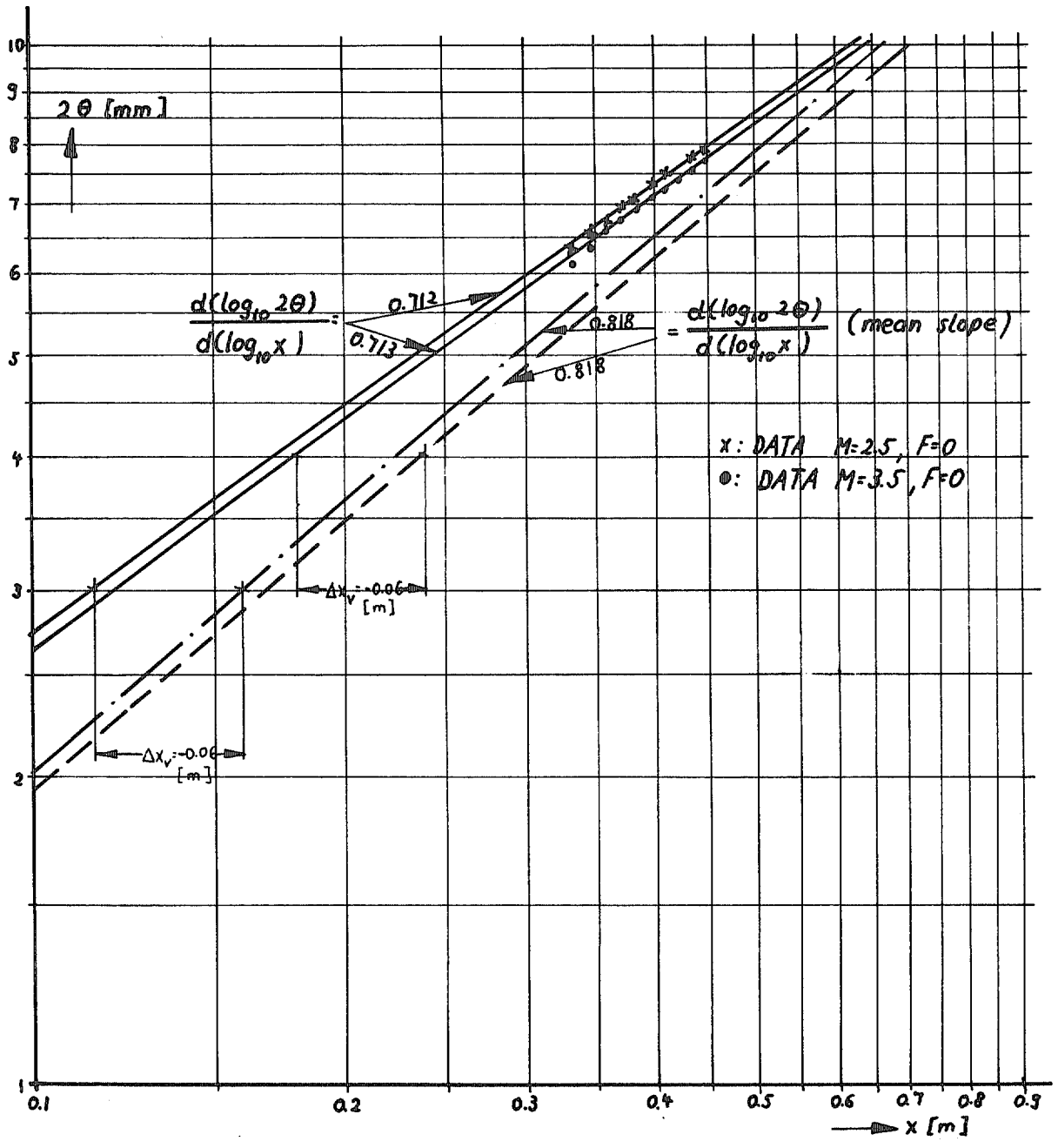

FIG. 15. Estimation of the virtual origin of turbulent flow after Ref. 17 for $M_\infty = 2{\cdot}5$ and $M_\infty = 3{\cdot}5$.

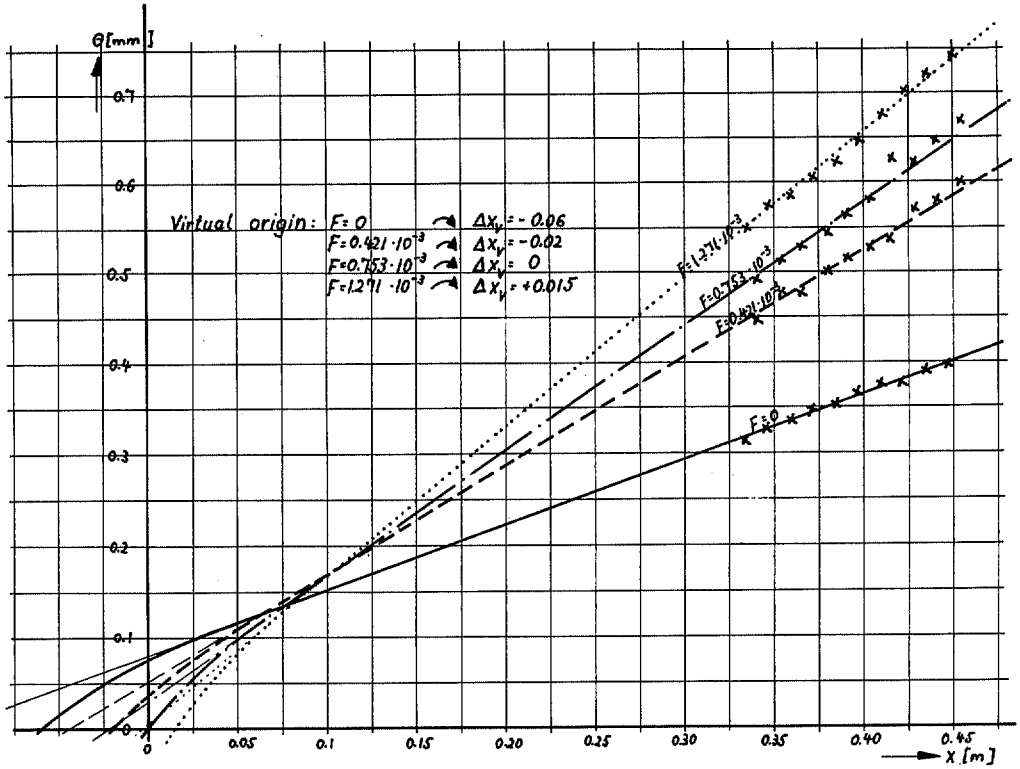

FIG. 16. Estimation of the virtual origin of turbulent flow from $\theta = f(x)$ ($M_\infty = 2{\cdot}5$, various F).

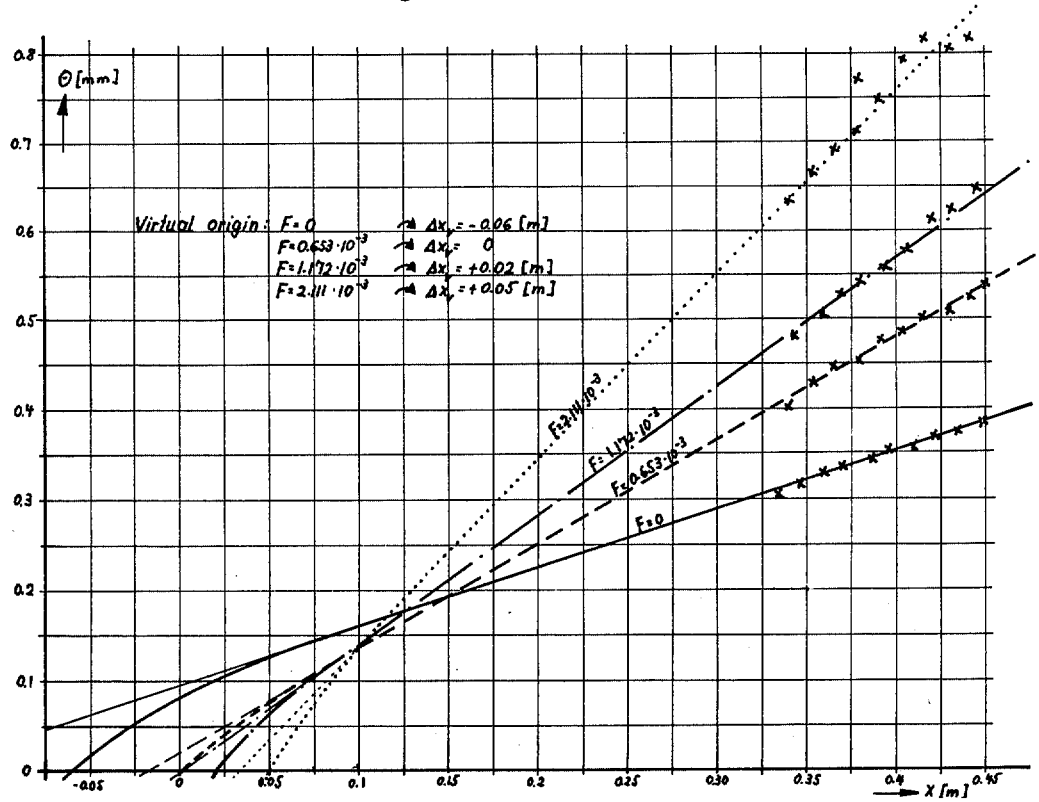

FIG. 17. Estimation of the virtual origin of turbulent flow from $\theta = f(x)$ ($M_\infty = 3{\cdot}5$, various F).

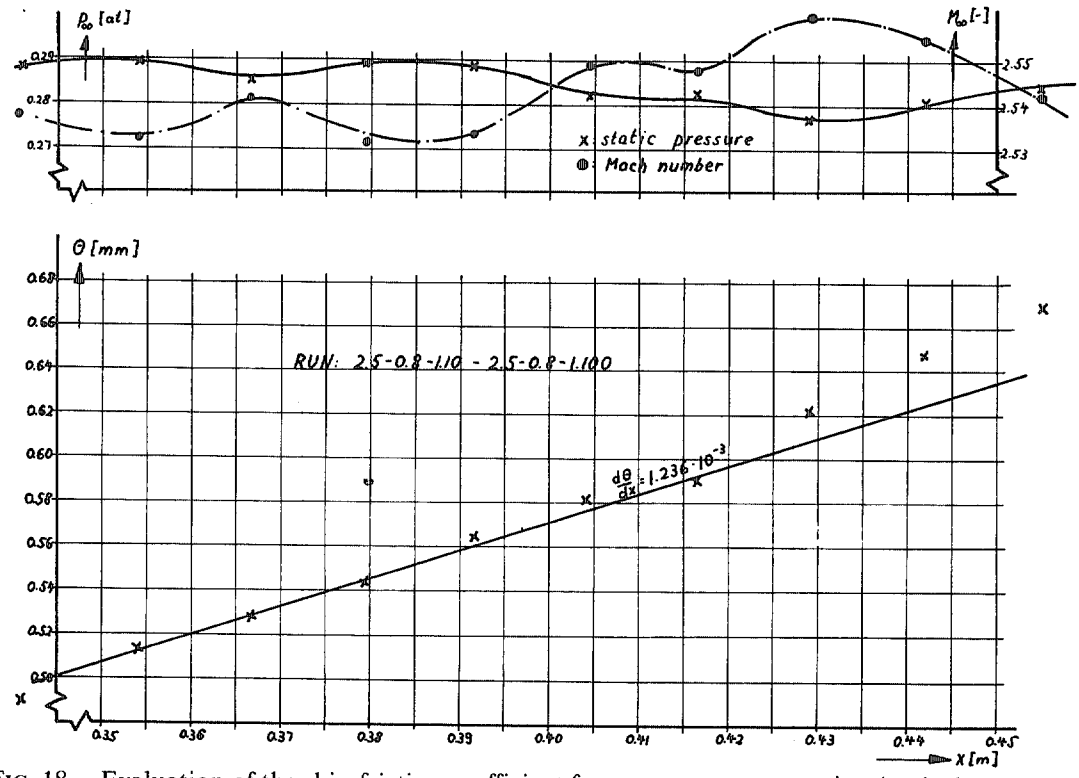

FIG. 18. Evaluation of the skin-friction coefficient from momentum equation (typical example, $M_\infty = 2{\cdot}54$, $F = 0{\cdot}753 \times 10^{-3}$).

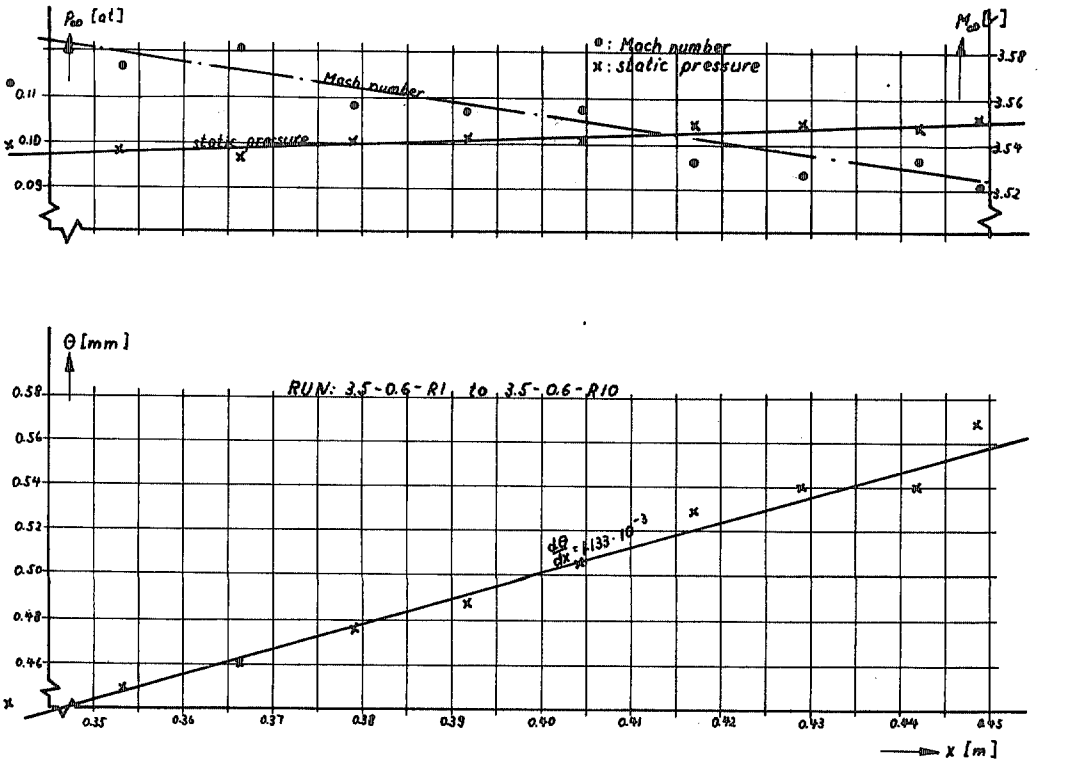

FIG. 19. Evaluation of the skin-friction coefficient from momentum equation (typical example, $M_\infty = 3{\cdot}55$, $F = 0{\cdot}636 \times 10^{-3}$).

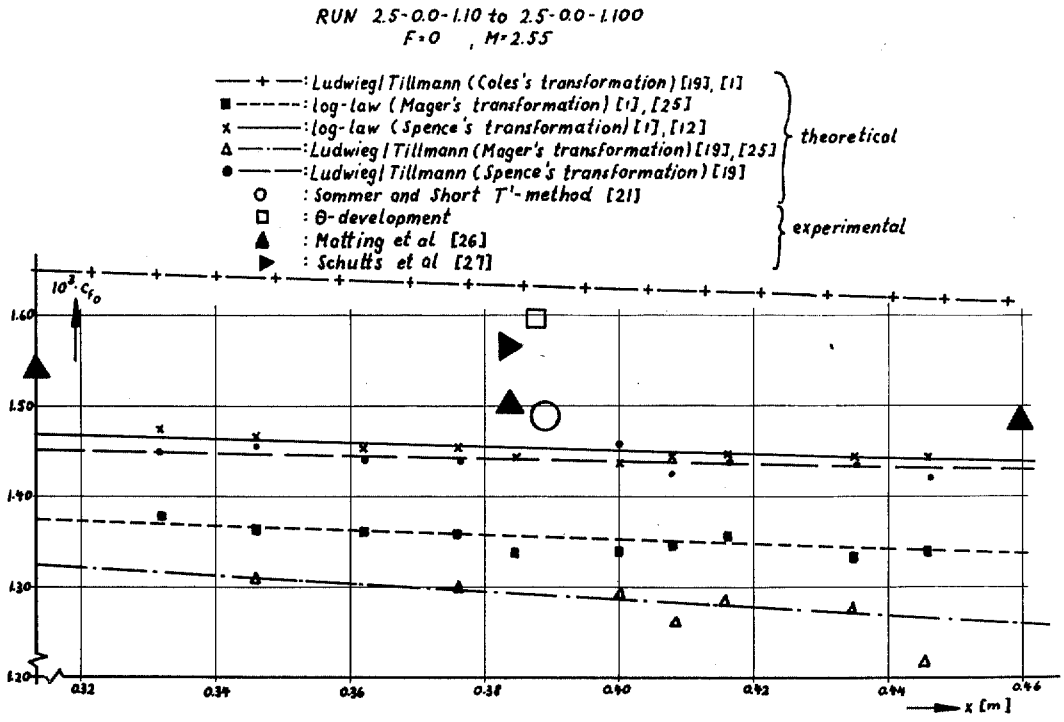

FIG. 20. Variation of skin-friction coefficient with distance along plate; ($M_\infty = 2{\cdot}5$, $F = 0$).

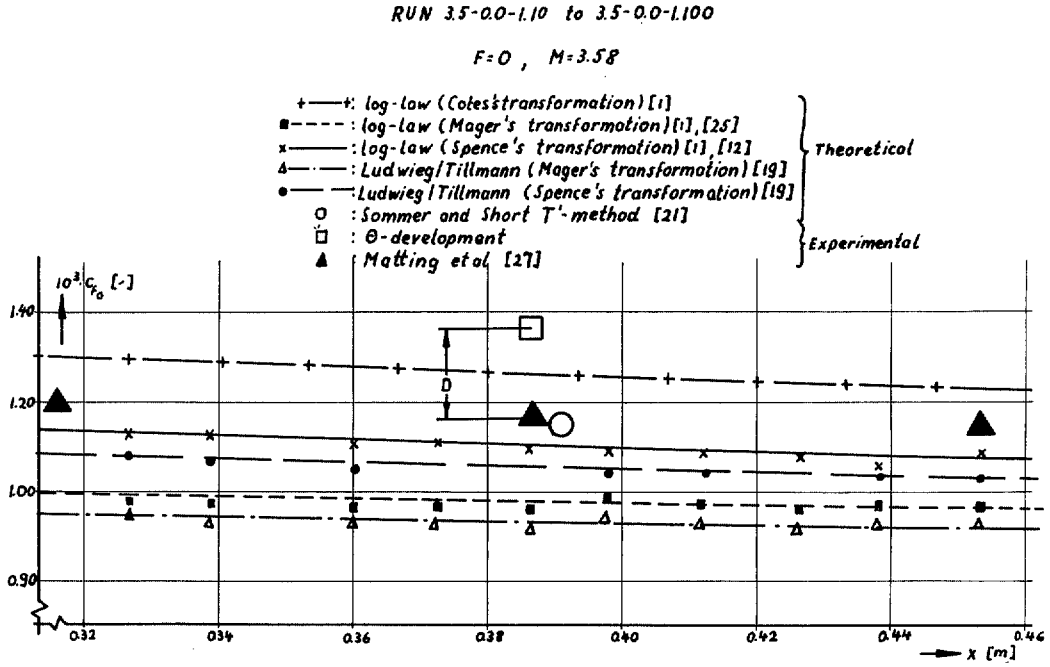

FIG. 21. Variation of skin-friction coefficient with distance along plate; ($M_\infty = 3{\cdot}5$, $F = 0$).

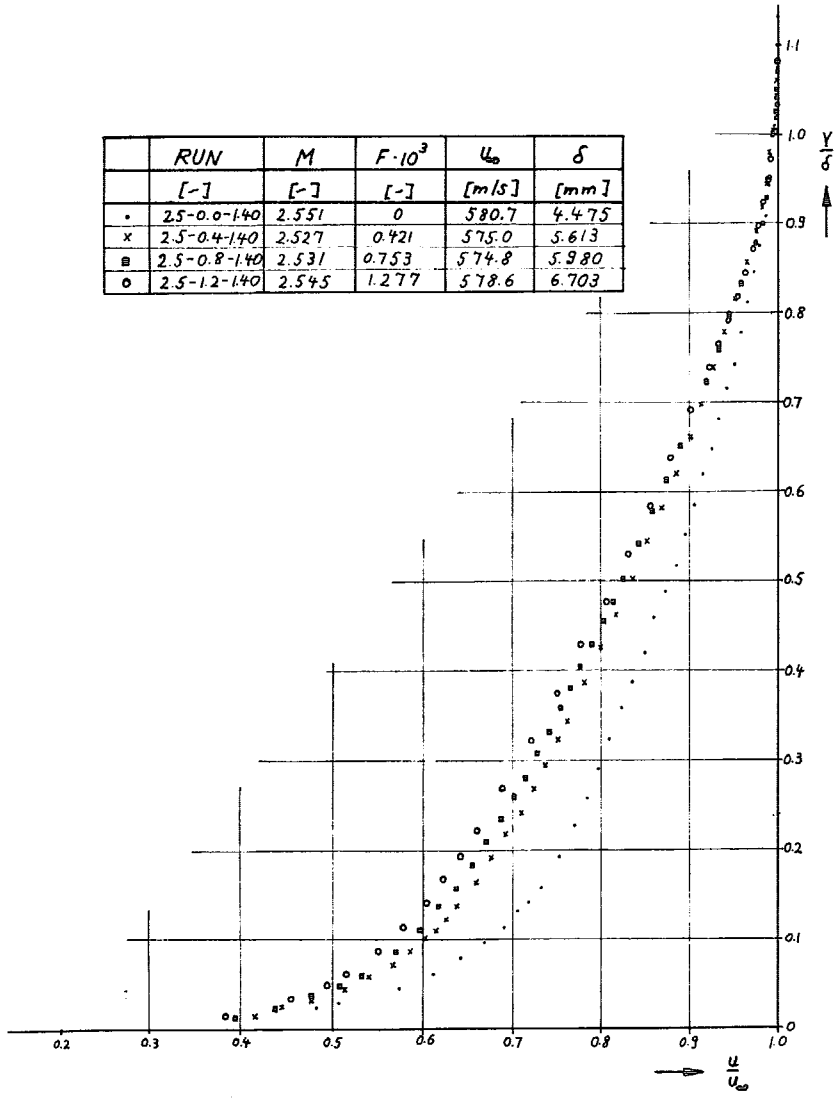

FIG. 22. Velocity profiles (with and without injection).

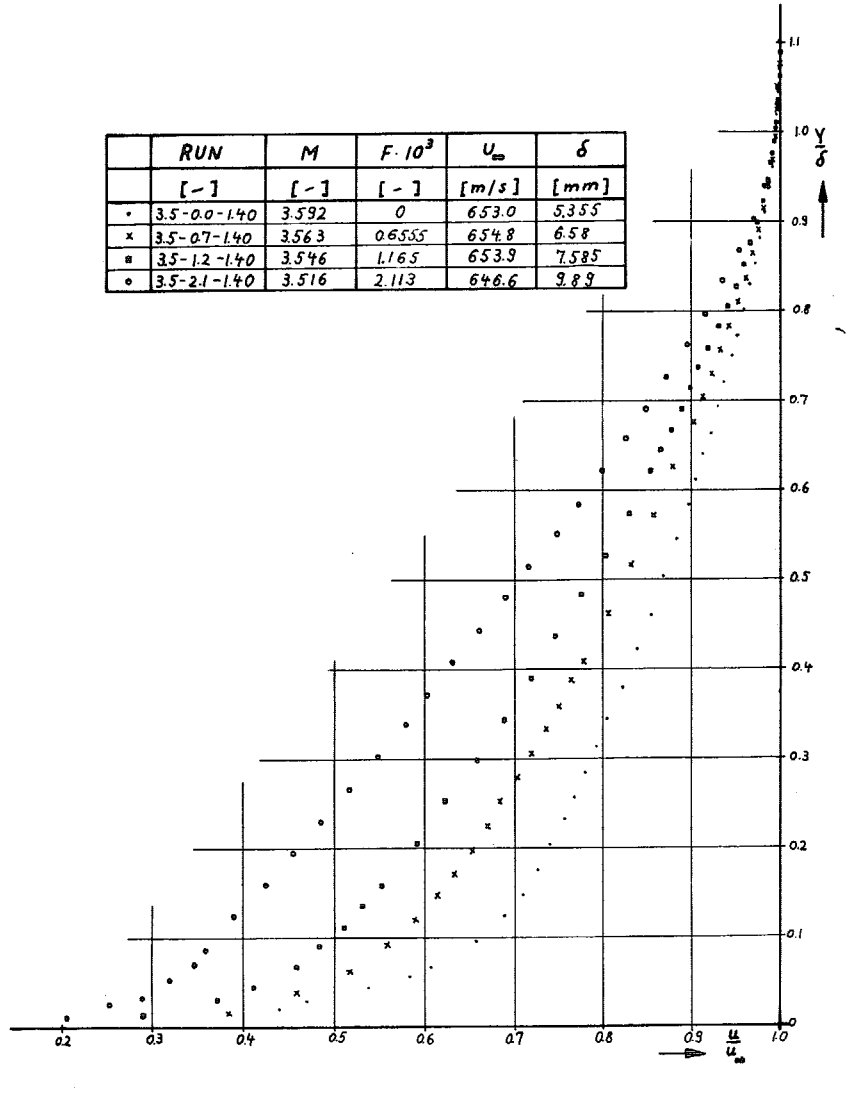

FIG. 23. Velocity profiles (with and without injection).

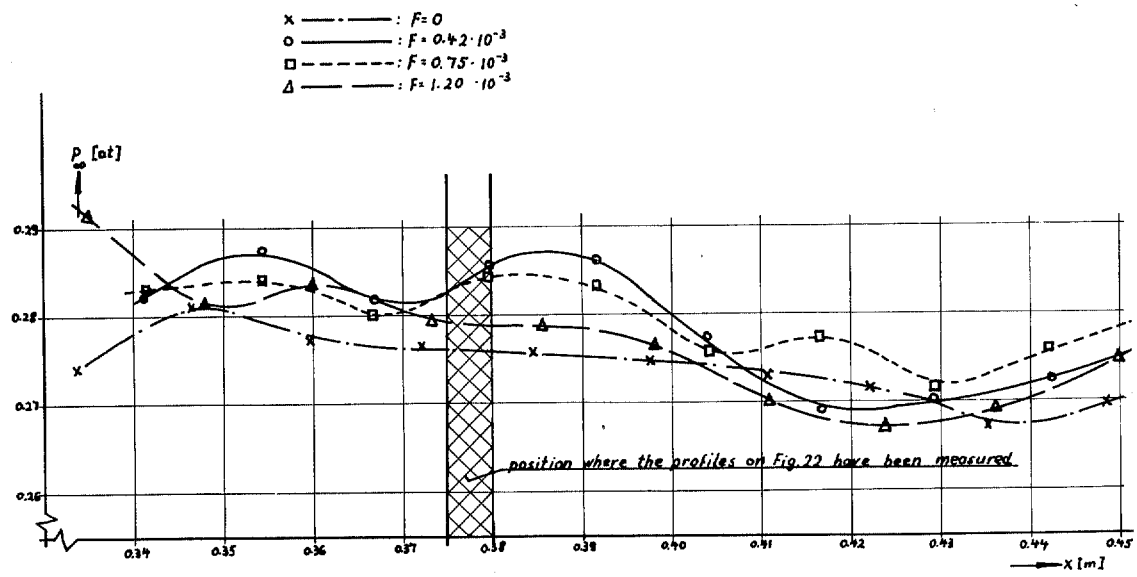

FIG. 24. Variation of static pressure along centreline, ($M_\infty = 2{\cdot}5$, various injection rates).

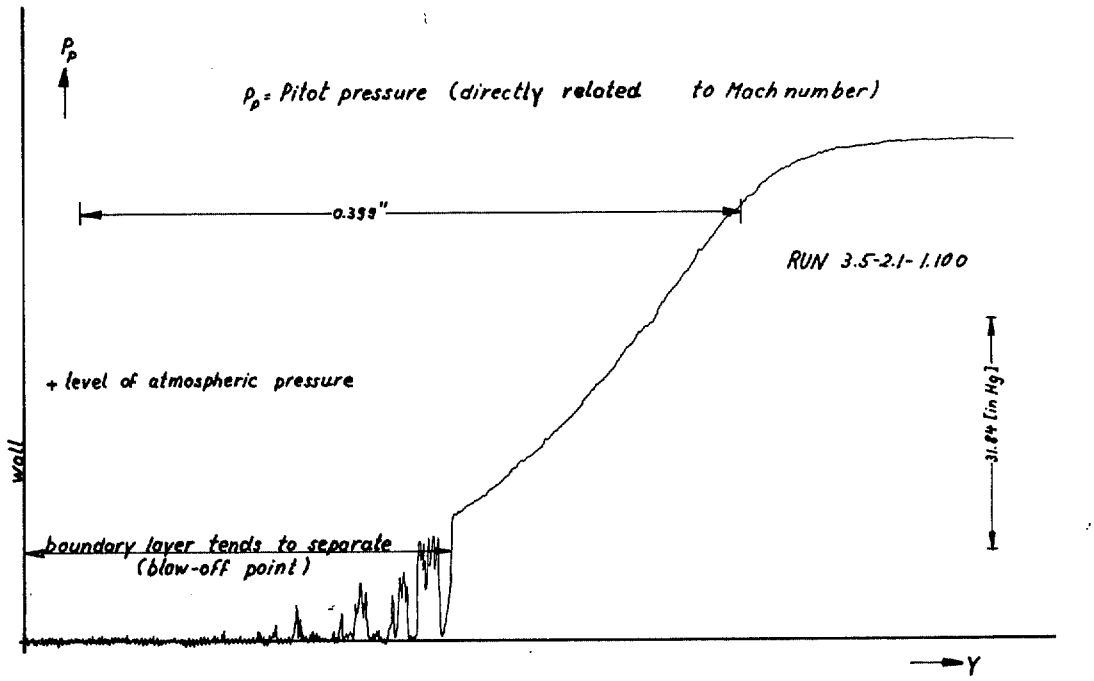

FIG. 25. Typical pitot pressure profile as drawn by X-Y plotter; ($F = 2{\cdot}111 \times 10^{-3}$, $M_\infty = 3{\cdot}5$, Station 100).

Explanation of the Symbols used on Figs. 26 to 31.

Mach number	$F \cdot 10^3$	$T_w > T_r$	$T_w \simeq T_r$	$T_w < T_r$	Plate
2.5	0	+			solid
	0.4	△	△	△	C
	0.7	○	○	○	C
	1.2	□	□	□	A
	1.3	▷			C
3.5	0	×			solid
	0.6	▲	▲	▲	C
	1.1	●	●	●	C
	2.1	■	■	■	C
	0.6	▽			D
	2.1	◆			D

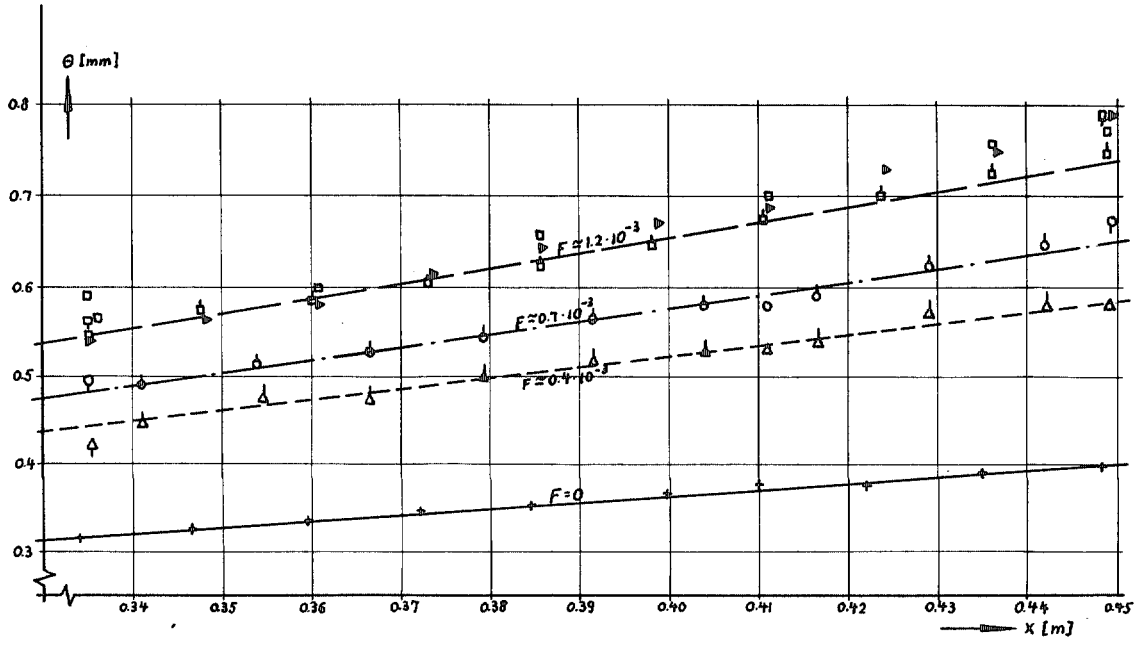

FIG. 26. Variation of the momentum thickness with distance along plate; ($M_\infty = 2{\cdot}5$, various injection rates F).

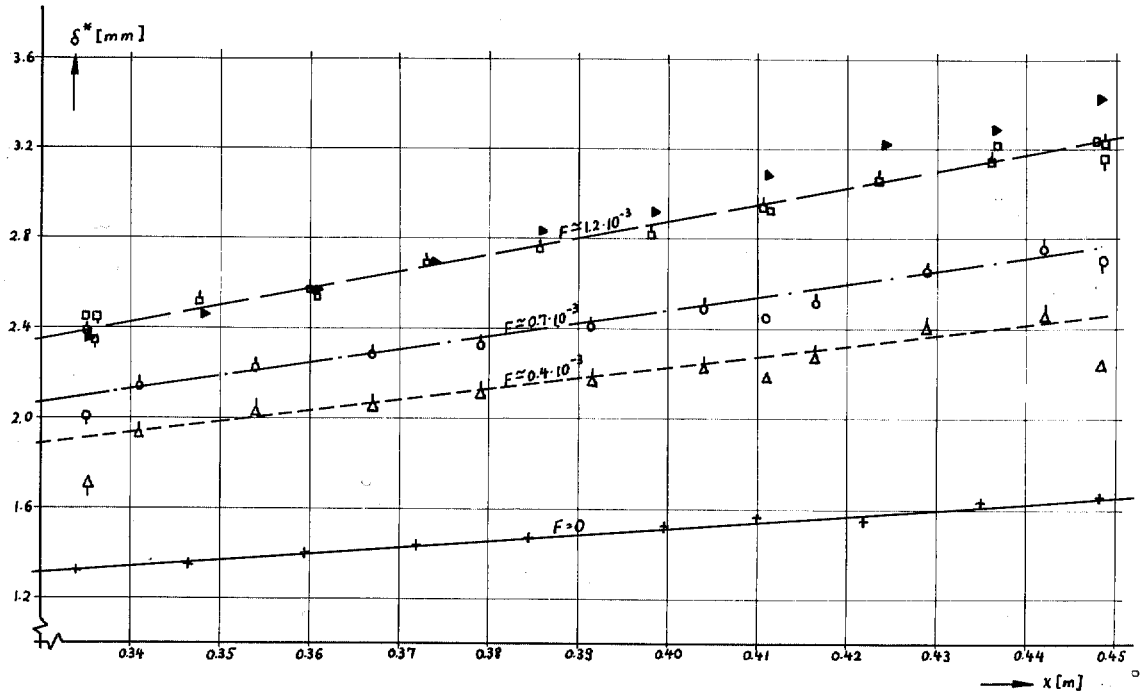

FIG. 27. Variation of displacement thickness with distance along plate; ($M_\infty = 2{\cdot}5$, various injection rates).

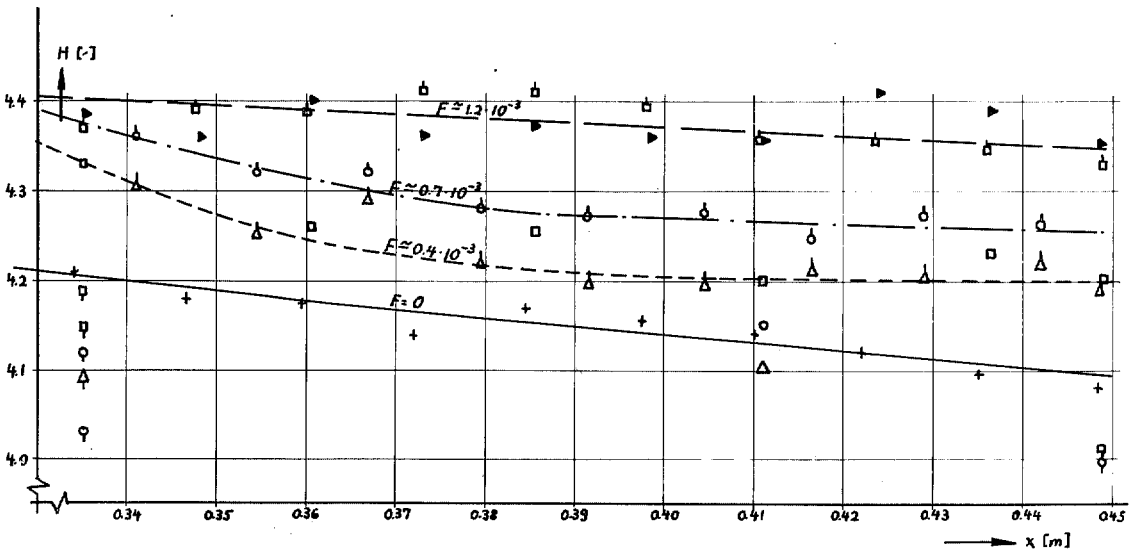

FIG. 28. Variation of the boundary-layer parameter H with distance along plate; ($M_\infty = 2{\cdot}5$, various injection rates).

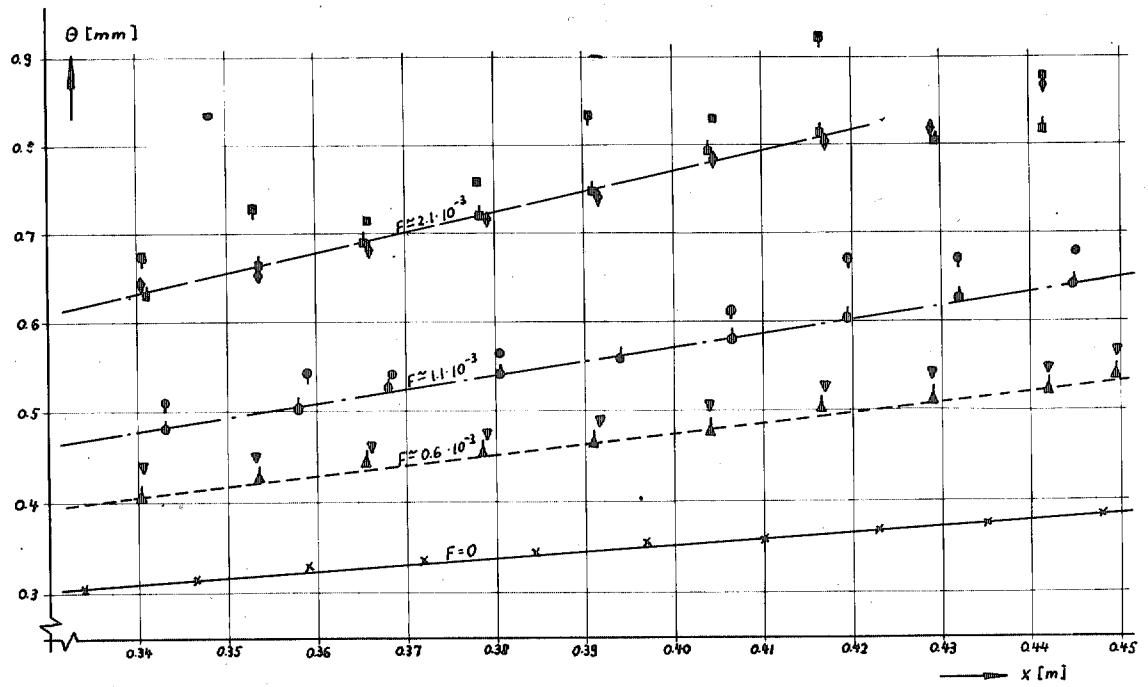

FIG. 29. Variation of the momentum thickness with distance along plate; ($M_\infty = 3{\cdot}5$, various injection rates F).

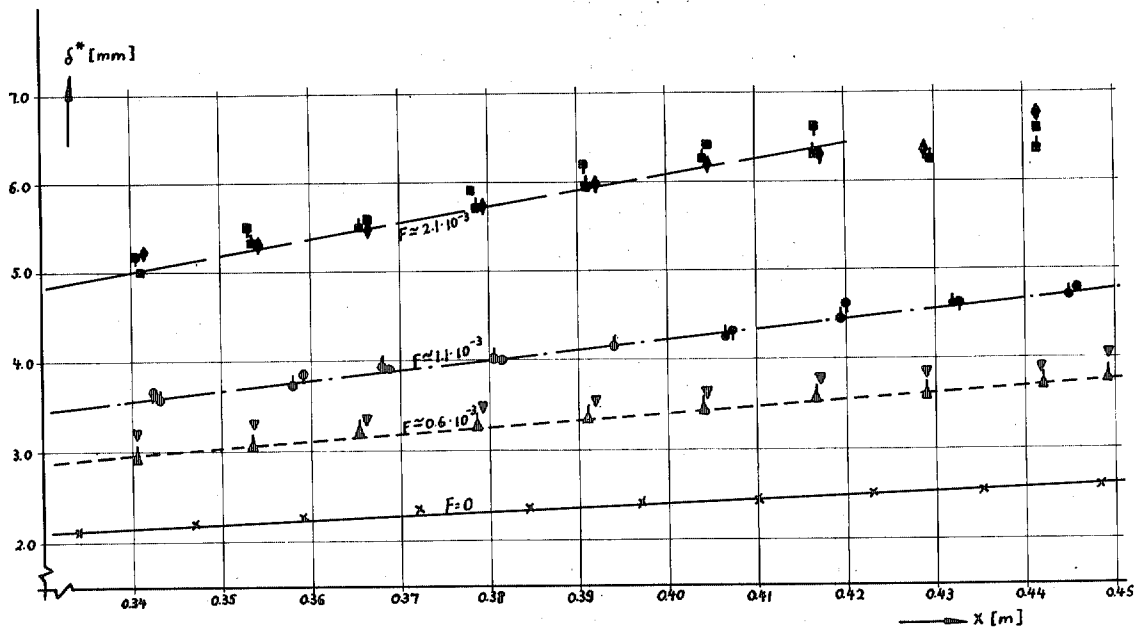

FIG. 30. Variation of displacement thickness with distance along plate; ($M_\infty = 3{\cdot}5$, various injection rates F).

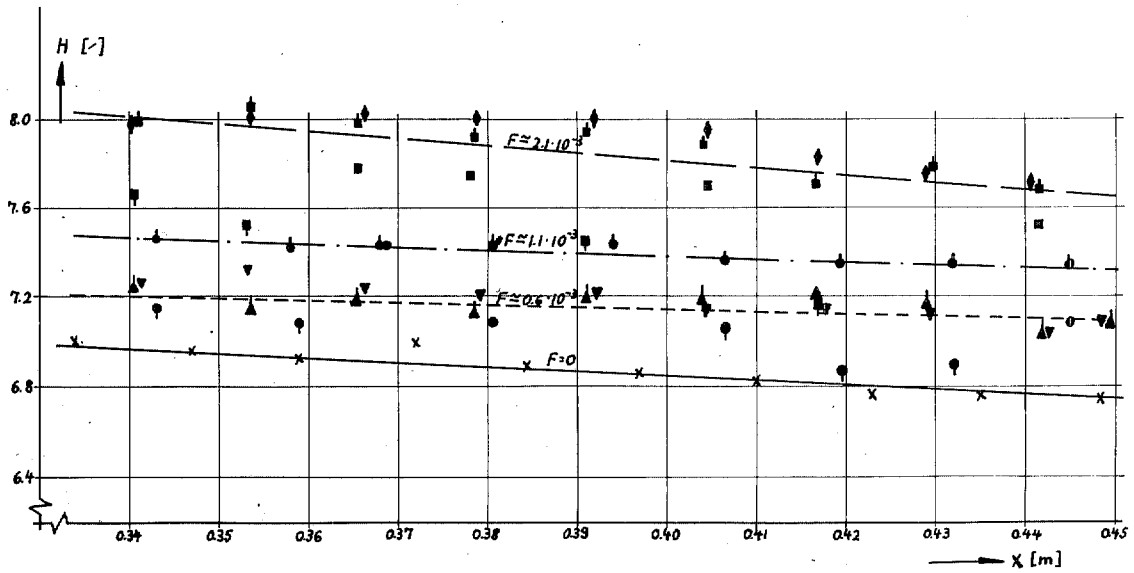

FIG. 31. Variation of the boundary-layer parameter H with distance along plate; ($M_\infty = 3{\cdot}5$, various injection rates F).

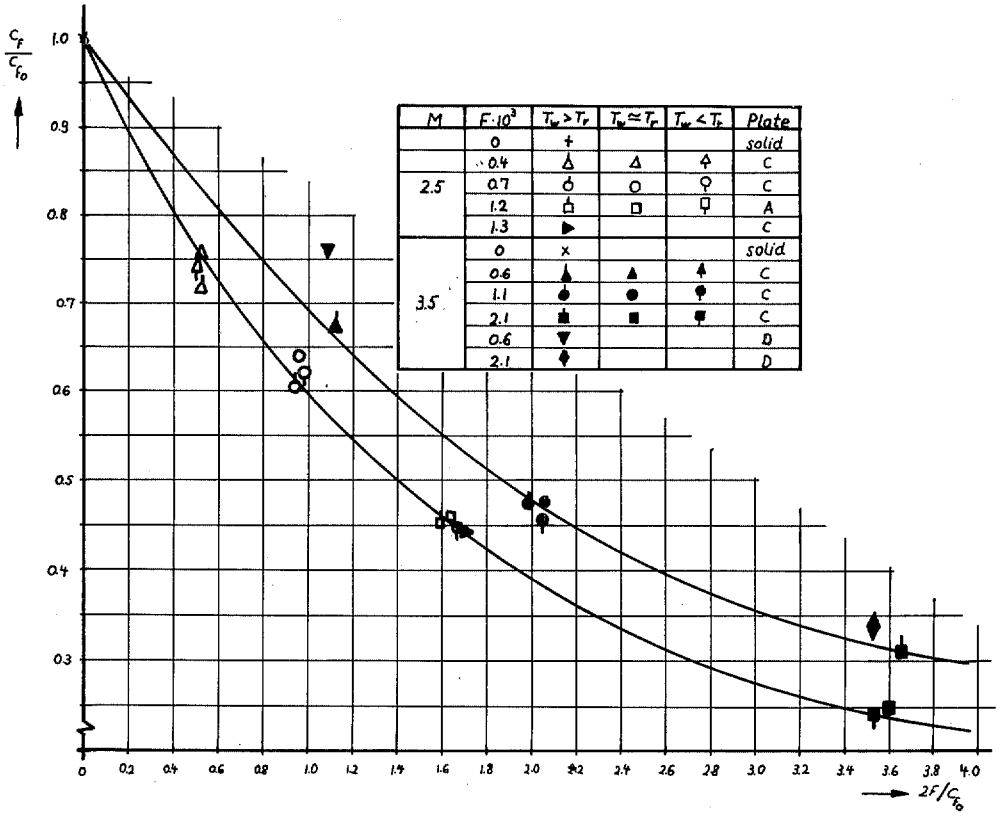

FIG. 32. The effect of heat transfer and surface roughness on the skin-friction coefficient for transpired compressible boundary layers.

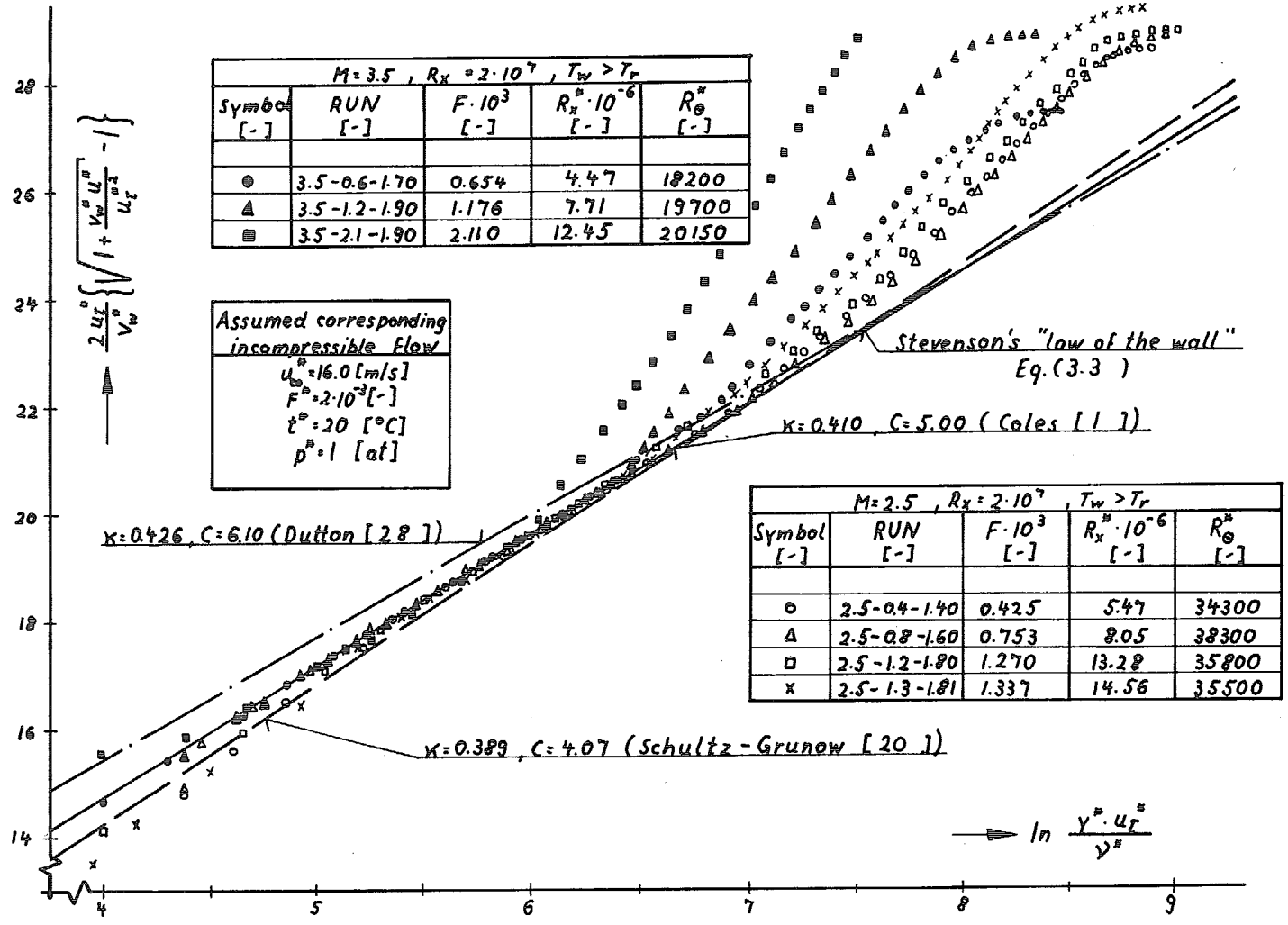

FIG. 33. Comparison between transformed compressible turbulent boundary-layer profiles with air injection and Stevenson's 'law of the wall' using the 'exact' transformation ($T_w > T_r$).

Explanation of the Symbols used on Fig. 34.

Symbol	Investigator	Mach number	Geometry
+	Mickley and Davies[29], 1957	incompressible	flat plate
×	Romanenko and Kharchenko[30], 1963	incompressible	flat plate
*	McQuaid[31], 1966	incompressible	flat plate
⌓	Rubesin[32], 1956	0; 2·0; 2·7	flat plate
□ ■	Danberg, 1960 Danberg, 1964	5·1 6·2	flat plate
● o	Present Investigation, 1966	2·5 3·5	flat plate
Δ ◁ ▽ ▷	Pappas and Okano, 1960	0·3 0·7 3·5 4·5	cone
◀	Rubesin[32], 1956	0; 2·0; 2·7	cone
▶	Tendeland and Okuno[34], 1956	2·7	cone

Theories:

————: Stevenson's law (Eq. (3.3)) + Jeromin's boundary layer transformation).

– – – – – – –: Dorrance and Dore[35], 1954.

——.——: Rubesin[36], 1954.

—— ——: Spalding *et al.*[37], 1964

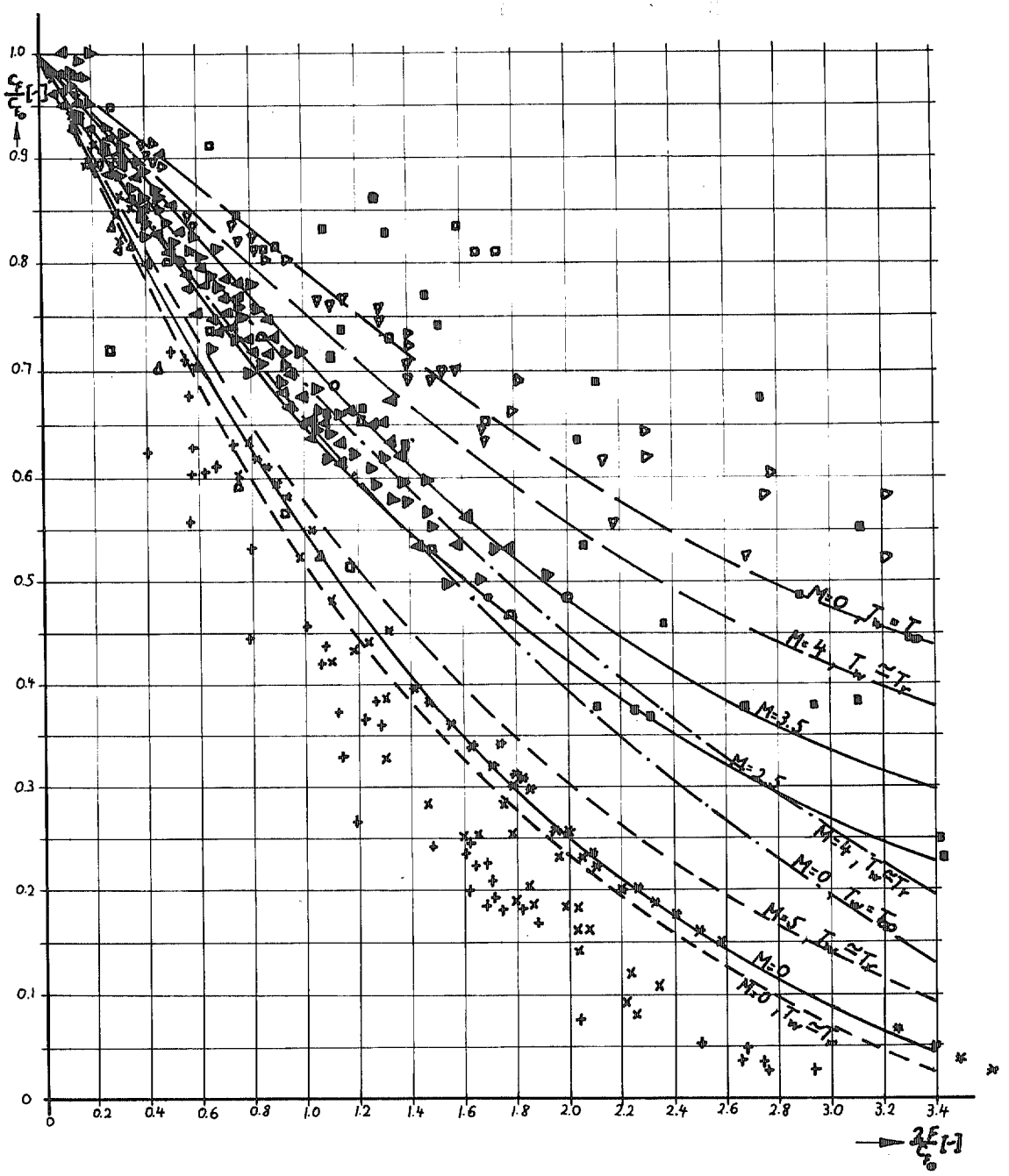

FIG. 34. Effect of air injection on the skin friction coefficient of a turbulent boundary layer.

Printed in Wales for Her Majesty's Stationery Office by Allens Printers (Wales) Limited

Dd.129527 K5

Published by
HER MAJESTY'S STATIONERY OFFICE

To be purchased from
49 High Holborn, London W.C.1
423 Oxford Street, London W.1
13A Castle Street, Edinburgh 2
109 St. Mary Street, Cardiff CF1 1JW
Brazennose Street, Manchester 2
50 Fairfax Street, Bristol 1
258-259 Broad Street, Birmingham 1
7-11 Linenhall Street, Belfast BT2 8AY
or through any bookseller

S.O. Code No. 23-35